

POLITECNICO DI TORINO

Collegio di Ingegneria Chimica e dei Materiali

**Corso di Laurea Magistrale
in Ingegneria Chimica e dei Processi Sostenibili**

Tesi di Laurea Magistrale

Development of Cu-Sn-based photo- electrocatalysts for the CO₂ valorization



Relatori

Prof.ssa Simelys Pris Hernández Ribullen
Prof. Nunzio Russo

Candidato

Antonio Bucci

Dicembre 2021

*“Tu vola alto amico caro!
Pure per chi non ce la fa.
Per chi di un sogno è prigioniero,
per chi non rinuncerà.
Pensa in grande, fallo ancora!
Tu cavalca quell’idea.
Suda, incazzati e poi prega
E quando puoi tu scappa via!
Che soffrire di coraggio è la più bella malattia!
VOLA ALTO”*

R. Zero

Riassunto in italiano

Negli ultimi anni, la Comunità Scientifica ha focalizzato la sua attenzione sui problemi legati al Global Warming. Le cause principali di questo fenomeno sono legate all'aumento delle emissioni di gas serra, legate ai processi industriali per soddisfare i sempre più esigenti bisogni umani. Uno dei gas serra più nocivi è l'anidride carbonica (CO_2). La concentrazione di CO_2 atmosferica è passata da 280 ppm in età preindustriale a un valore prossimo a 420 ppm nel 2020, a causa del crescente utilizzo di combustibili fossili, legati alle attività antropiche (es. energia termica, ecc.). Riuscire a riutilizzare questo gas di scarto per ottenere prodotti a valore aggiunto è una strategia efficace sia per mitigare il surriscaldamento globale che per far fronte alla crisi energetica. Le reazioni di riduzione dell'anidride carbonica (CO_2RR) sono processi complessi, in cui è coinvolto un gran numero di reazioni di trasferimento di elettroni e protoni. A causa dei suoi doppi legami covalenti, l'anidride carbonica presenta una cinetica lenta e un'elevata stabilità termodinamica. Per questi motivi, la maggior parte dei CO_2RR sono sfavorevoli a temperatura e pressione ambiente. Inoltre, il numero di elettroni richiesti per la riduzione è elevato tale da rendere estremamente difficile una reazione one-step, in particolare una reazione non catalizzata. Secondo precedenti considerazioni cinematiche e termodinamiche, è necessario utilizzare un catalizzatore per effettuare tali reazioni. La catalisi elettrochimica e la fotocatalisi possono essere strategie promettenti per la conversione dell'anidride carbonica in condizioni ambientali, perché la prima utilizza l'elettricità, possibilmente prodotta da fonti rinnovabili, e la seconda sfrutta la radiazione solare per guidare la reazione. Quindi, la riduzione foto-elettrochimica della CO_2 può essere vista come la "fotosintesi artificiale", in cui la foto e la catalisi elettrochimica sono combinate per formare un sistema più efficiente. Rispetto ai metodi convenzionali, i sistemi foto/elettrochimici presentano numerosi vantaggi in termini di efficienza, compatibilità ambientale, elevata selettività e facilità di lavorazione.

I composti a base rame sono catalizzatori interessanti verso l'anidride carbonica, grazie alle loro buone proprietà di trasferimento multi-elettronico dovute ai loro elettroni debolmente legati. Tra questi, i catalizzatori più promettenti sono il rame metallico (Cu), l'ossido di rame (I) (Cu_2O) e l'ossido di rame (II) (CuO). Tuttavia, solo Cu_2O mostra proprietà fotocatalitiche. Cu_2O è un semiconduttore a bandgap diretto con un valore di bandgap vicino a 2 eV, che rende l'ossido di rame(I) in grado di assorbire la luce visibile che costituisce una frazione maggiore dello spettro solare. A causa della presenza di vacanze Cu con carica negativa, presenta una condutività intrinseca di tipo p e ha una delle più basse affinità elettroniche degli elementi. Inoltre, a causa dell'abbondanza dei suoi elementi costitutivi, il Cu_2O è un materiale relativamente economico. Grazie a questi vantaggi, Cu_2O è un buon candidato per la riduzione di CO_2 . A causa della sua natura cristallina, Cu_2O ha diverse morfologie dei suoi cristalli, che determinano diverse attività fotocatalitiche. Le morfologie Cu_2O sono le seguenti: cubi; cubi a faccia in su; ottaedri troncati di spigolo e spigolo; dodecaedri rombici troncati su tutti gli angoli; {100}-dodecaedri rombici troncati; dodecaedri rombici. Nei confronti della CO_2 la struttura cristallina più foto-attiva è la rombica dodecaedrica, mentre quella meno foto-attiva è la cubica. Se Cu_2O possiede buone proprietà come catalizzatore foto-elettrochimico, presenta il problema di soffrire di foto-corrosione e cambiamenti chimici. A causa delle reazioni di auto-riduzione e auto-ossidazione termodinamicamente fattibili, la degradazione del Cu_2O a Cu e CuO sono inevitabili. Ci sono lavori in letteratura che mostrano come Cu_2O si ossidi in CuO sotto illuminazione o che si riduca a Cu in un ambiente in eccesso di elettroni sotto foto-irradiazione. Per mitigare tale instabilità, è possibile realizzare un co-catalizzatore, accoppiando un foto-catalizzatore più stabile all'ossido di rame (I). Un contendente è l'ossido di stagno (IV) (SnO_2) per le sue capacità ottiche e proprietà di raccolta di carica. SnO_2 è utilizzato nelle celle solari Perovskite per migliorare notevolmente

la loro stabilità, aumentando il tempo di lavoro e le prestazioni fotovoltaiche, riducendo la ricombinazione di carica. Per questi motivi, l'ossido di stagno (IV) è un buon co-catalizzatore per ottenere un catalizzatore finale che sfrutta la buona foto-attività del Cu₂O e la stabilità dello SnO₂.

Lo scopo di questo lavoro è studiare i metodi di sintesi dell'ossido di rame (I) e il loro utilizzo nello sviluppo di catalizzatori foto-elettrochimici a base di rame e stagno per la valorizzazione dell'anidride carbonica. Inizialmente, le attività sono focalizzate su una ricerca bibliografica sulla fase cristallina più attiva del Cu₂O per la riduzione foto-elettrochimica della CO₂ e la sua sintesi. Successivamente, l'attenzione è stata rivolta alla sintesi, alla caratterizzazione e alla test di catalizzatori Cu₂O-SnO₂ preparati con due metodi di sintesi: co-precipitazione e strategia in due fasi di precipitazione e impregnazione. Per il metodo della coprecipitazione, lo studio è partito da una sintesi già implementata dal gruppo di ricerca del Prof. Hernández del Politecnico di Torino, in cui Cu(NO₃)₂ * 3H₂O e SnCl₄ * 5H₂O sono utilizzati come precursori, Na₂CO₃ è utilizzato come agente precipitante, mentre NaBH₄ ha la funzione di agente riducente. Questa strategia di sintesi è stata modificata applicando gli ultrasuoni durante tutto il tempo di reazione. Inoltre, anche il pH della soluzione è stato modificato per favorire la formazione simultanea di Cu₂O dodecaedrico rombico e SnO₂. La sintesi iniziale per il catalizzatore core-shell è riportata da Zhang et al., che sintetizzano nanocubi core-shell di Cu₂O-SnO₂ con lo spessore controllato dell'ossido di stagno (IV). Questo metodo è suddiviso in due fasi; il primo passaggio è una sintesi per precipitazione umida per ottenere nanocubi di ossido di rame(I), utilizzando CuCl₂, NaOH e C₆H₈O₆ come reagenti; la seconda è la formazione di uno strato di SnO₂ mediante strategia di impregnazione su Cu₂O, utilizzando SnCl₄ * 5H₂O. Poiché i nanocubi sono la forma cristallina meno fotoattiva dell'ossido di rame(I), lo scopo è cercare di ottenere Cu₂O con una struttura cristallina simile al dodecaedro rombico. Inizialmente si è cercato di aumentare la quantità di Cu₂O sintetizzata variando le molarità dei precipitanti e degli agenti riducenti e realizzare il catalizzatore finale. Poiché il Cu₂O è cubico, nella sintesi è stato aggiunto un processo di attacco acido per modificare la forma cristallina e cercare di ottenere una morfologia con maggiore attività photocatalitica.

Le metodologie di sintesi effettuate prevedono: sintesi di Cu₂O-SnO₂ via coprecipitazione; sintesi di Cu₂O via coprecipitazione senza precursore dello stagno; sintesi di Cu₂O tramite precipitazione con C₆H₈O₆ come agente riducente; sintesi di Cu₂O tramite precipitazione con C₆H₈O₆ come agente riducente con uno step di etching acid; sintesi di Cu₂O tramite precipitazione co SDS e NH₂OH*HCl come agente riducente; sintesi di Cu₂O-SnO₂ tramite precipitazione e impregnazione.

Per la sintesi di Cu₂O-SnO₂ via coprecipitazione, 5.797 g di Cu(NO₃)₂ e 3.355 g di SnCl₄*5H₂O sono stati aggiunti in un volume di 40 mL di acqua MilliQ, per preparare la soluzione dei precursori. 0,908 g di NaBH₄ sono stati sciolti in 20 mL di acqua MilliQ per la soluzione dell'agente riducente, mentre 10,599 g di Na₂CO₃ sono stati utilizzati per preparare una soluzione di agente precipitante di 100 mL. 200 mL di acqua MilliQ sono stati aggiunti a un becher. Questa è stata immersa in un bagno di olio di silicone per riscaldare meglio la soluzione, posta su una piastra magnetica a 70°C e agitata da un'ancora. La soluzione del precursore e la soluzione dell'agente riducente sono state aggiunte a 200 mL di acqua MilliQ tramite pompe peristaltiche a flusso costante e sono state regolate in modo tale che in 8 minuti le soluzioni siano completamente aggiunte al volume di acqua iniziale. Laggiunta di Na₂CO₃ era invece discontinua e regolata da una pompa peristaltica per mantenere il pH della soluzione reagente ad un valore costante. Il sonicator è stato impostato su un'ampiezza del 30%. Quando è stata raggiunta la temperatura richiesta, tutte le pompe e il sonicator sono stati avviati e fermati al termine del tempo di reazione. La fase successiva è l'invecchiamento per 1 h sotto agitazione a temperatura costante. Successivamente la soluzione ottenuta è stata filtrata e lavata mediante filtrazione sotto vuoto e laggiunta periodica di acqua MilliQ per un totale di 1.250 L. Infine, il campione è stato posto in stufa ad essiccare per circa 12 h a 60°C. Tali sintesi sono state condotte a pH 7, acido e basico.

Per la sintesi di Cu₂O via coprecipitazione senza precursore dello stagno, sono stati usati gli stessi reagenti, ma le molarità sono state cambiate. Nel campione CP-Cu₂O-pH7-0.6-1-1,2 la molarità di tutti i reagenti è rimasta invariata, nel campione CP-Cu₂O-pH7-0.6-1-0.6 la molarità del NaBH₄ è stata dimezzata, mentre nel campione CP-Cu₂O-pH7-0,6-1-0,3 la molarità di NaBH₄ è stata ridotta di quattro volte.

Per la sintesi di Cu₂O tramite precipitazione con C₆H₈O₆ come agente riducente, i nanocubi di Cu₂O sono stati sintetizzati aggiungendo gradualmente una soluzione di NaOH in una soluzione di CuCl₂. Dopo 30 minuti, è stata aggiunta goccia a goccia una soluzione di acido ascorbico e successivamente invecchiata per 180 minuti. Al termine dell'invecchiamento, la soluzione è stata filtrata mediante filtrazione sottovuoto e lavata con acqua MilliQ. Infine, il campione è stato posto in un essiccatore ad essiccare per circa 12 ore a 60 °C. Le concentrazioni e i volumi dei reagenti sono stati variati per aumentare la quantità di Cu₂O ottenuto. In P1-Cu₂O-0.01-2-0.6-300 non è cambiato nulla. In P1-Cu₂O-0.01-3-0.6-300 la molarità dell'agente precipitante è stata aumentata del 50%. P1-Cu₂O-0.01-2-0.9-300 mostra un aumento del 50% della molarità dell'agente riducente. In P1-Cu₂O-0.01-3-0,9-300 invece sia gli agenti precipitanti che riducenti sono aumentati del 50%. Questi campioni sono stati sintetizzati con volumi delle soluzioni uguali a quelli della sintesi di partenza. Invece, P1-Cu₂O-0.01-3-0.9-600 e P1-Cu₂O-0.02-6-1.8-600 sono stati sintetizzati con volumi raddoppiati. Tuttavia, P1-Cu₂O-0.01-3-0.9-600 ha le stesse molarità di P1-Cu₂O-0.01-3-0.9-300, mentre P1-Cu₂O-0.02-6-1.8-600 ha doppie molarità rispetto a P1-Cu₂O-0.01-3-0.9-300. La tabella R1 mostra le molarità e i volumi delle soluzioni utilizzate per le sintesi sopra menzionate.

Tabella R1: Molarità e volumi dei campioni di Cu₂O sintetizzati. .

Campione	Molarità e Volume	CuCl ₂	NaOH	C ₆ H ₈ O ₆
P1-Cu ₂ O-0.01-2-0.6-300	M	0.01	2	0.6
	mL	250	25	25
P1-Cu ₂ O-0.01-3-0.6-300	M	0.01	3	0.6
	mL	250	25	25
P1-Cu ₂ O-0.01-2-0.9-300	M	0.01	2	0.9
	mL	250	25	25
P1-Cu ₂ O-0.01-3-0.9-300	M	0.01	3	0.9
	mL	250	25	25
P1-Cu ₂ O-0.01-3-0.9-600	M	0.01	3	0.9
	mL	500	50	50
P1-Cu ₂ O-0.02-6-1.8-600	M	0.02	6	1.8

	mL	500	50	50
--	----	-----	----	----

Per la sintesi di Cu₂O tramite precipitazione con C₆H₈O₆ come agente riducente con uno step aggiuntivo di etching acid, una soluzione di HCl (1 M, 100 mL) è stata aggiunta alla soluzione del reagente attraverso la pompa peristaltica per mantenere il pH ad un valore di 5,5. In P1-Cu₂O-0.02-6-1.8-300-Et0 l'attacco acido è stato effettuato contemporaneamente alla fase di invecchiamento, che in questo caso è durata 2 ore invece di 3 ore. Nel caso invece di P1-Cu₂O-0.02-6-1.8-300-Et3, la fase di attacco è stata eseguita dopo la fase di 3 ore di invecchiamento e la soluzione del reagente è stata mantenuta a pH 5,5 per 25 minuti. La tabella R2 mostra le molarità e i volumi delle soluzioni utilizzate per le sintesi sopra menzionate.

Tabella R2: Molarità e volumi dei campioni di Cu₂O sintetizzati con uno step aggiuntivo di etching acido.

Sample	Molarity and Volume	CuCl ₂	NaOH	C ₆ H ₈ O ₆	HCl
P1-Cu ₂ O-0.02-6-1.8-300-Et0	M	0.02	6	1.8	1
	mL	250	25	25	100
P1-Cu ₂ O-0.02-6-1.8-300-Et3	M	0.02	6	1.8	1
	mL	250	25	25	100

Per la sintesi di Cu₂O tramite precipitazione co SDS e NH₂OH*HCl come agente riducente, 0,67225 g di CuCl₂ vengono aggiunti in un volume di 25 mL di acqua MilliQ, che è la soluzione precursore. 1,66776 g di NH₂OH*HCl vengono sciolti in 120 mL di acqua MilliQ per la soluzione dell'agente riducente, mentre 0,71995 g di NaOH vengono utilizzati per preparare una soluzione dell'agente precipitante di 9 mL. 346 mL di acqua MilliQ sono stati aggiunti a un becher. Questa è stata immersa in un bagno di olio di silicone per riscaldare meglio la soluzione, posta su una piastra magnetica a 35 °C e agitata da un'ancora. La soluzione precursore e 8,7 g di SDS sono stati aggiunti ai 346 mL di acqua MilliQ. Quando l'SDS è stato completamente sciolto, alla soluzione reattiva è stata aggiunta una soluzione di NaOH e, successivamente, è stata aggiunta anche la soluzione di NH₂OH*HCl. La soluzione viene tenuta sotto agitazione per 1 h per la crescita dei cristalli. Dopo la fase di invecchiamento, la soluzione è stata centrifugata e il precipitato è stato lavato con una soluzione di 300 mL di acqua ed etanolo in rapporto 1: 1. Il lavaggio e la centrifugazione sono stati eseguiti due volte con la stessa soluzione di etanolo-acqua per rimuovere i reagenti non reagenti e l'SDS. Un ulteriore e finale lavaggio è stato effettuato con il solo etanolo. Infine, Cu₂O è stato disperso in 15 mL di etanolo per lo stoccaggio per evitare possibili reazioni con l'O₂ atmosferico. Prima di essere analizzato, il campione è stato essiccato in un essiccatore sotto vuoto a 60°C per 12 h. La tabella R3 mostra la quantità, le molarità e i volumi delle soluzioni utilizzate per le sintesi sopra menzionate.

Tabella R3: Molarità e volumi delle soluzioni utilizzate..

Reagent list	mL	M	G
H ₂ O	346		
CuCl ₂	25	0.2	0.6722
SDS			8.7
NaOH	9	2	0.7199
NH ₂ OH*HCl	120	0.2	1.6678

Per la sintesi di Cu₂O-SnO₂ tramite precipitazione e impregnazione, 150 mg di Cu₂O, precedentemente sintetizzato, sono stati sciolti nella soluzione di 150 mL di etanolo e 4,5 mL di soluzione 0,2 M NaCl. Quindi, 0,005 g di SnCl₄*5H₂O vengono dispersi in 50 mL di etanolo e aggiunti alla soluzione. La quantità di SnCl₄*5H₂O utilizzata era in rapporto 1:40 con Cu₂O. La soluzione è stata agitata per 10 minuti e posta in una centrifuga per recuperare il catalizzatore. Infine, il campione è stato posto in un essiccatore ad essiccare per circa 12 ore a 60 °C.

Tutte le caratterizzazioni dei campioni sintetizzati sono presentate in questo paragrafo. Nello specifico, le caratterizzazioni includono analisi XRD, analisi BET, spettroscopia di assorbimento UV-visibile, analisi EDX e FE-SEM.

Per quanto riguarda la strategia di sintesi per coprecipitazione, dall'analisi degli spettri XRD dei campioni sintetizzati a pH 7, i picchi relativi al Cu₂O sono ben evidenti, mentre quelli di SnO₂ hanno una forma spaciata, probabilmente a causa della sua natura amorfa. Per i campioni sintetizzati a pH diversi da quello neutro, CP-Cu₂O-SnO₂-pH8 mostra solo picchi relativi a Cu₂O e SnO₂, mentre CP-Cu₂O-SnO₂-pH5.5 ha anche picchi di CuO, CP-Cu₂O-SnO₂-pH6 ha picchi sia di Cu metallico che CuO e CP-Cu₂O-SnO₂-pH9,5 ha picchi relativi al Cu metallico oltre a quelli di Cu₂O e SnO₂. La figura R1 confronta la dimensione dei cristalli di Cu₂O, {220}/{200} PIR (rapporto di intensità di picco) e {111}/{200} PIR di campioni di CP-Cu₂O-SnO₂ sintetizzati a diversi pH della soluzione.

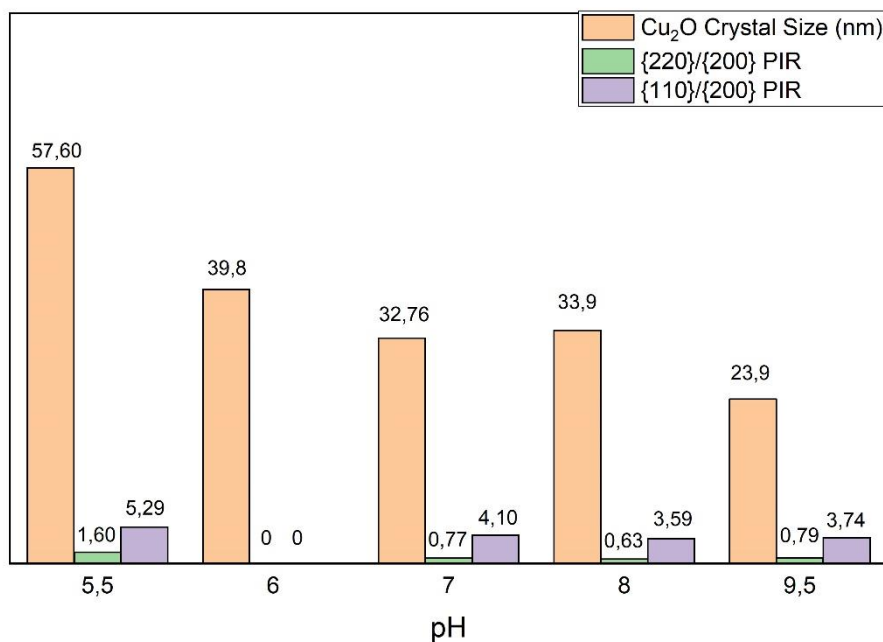


Figura R1: Cu_2O Crystal Size, $\{220\}/\{200\}$ PIR and $\{111\}/\{200\}$ PIR dei campioni CP- $\text{Cu}_2\text{O}-\text{SnO}_2$ a differenti pH.

Dalla Figura R1, si può dedurre che il campione sintetizzato a pH 8 non presenta significative differenze con quello a pH neutro. Si può notare inoltre che le dimensioni dei cristalli tendano ad aumentare spostandosi verso pH più acidi. Tuttavia, a pH acidi la reazione di sintesi è meno controllata, data la presenza di Cu e CuO e le variazioni non trascurabili dei parametri PIR $\{220\}/\{200\}$ e PIR $\{111\}/\{200\}$.

Per quanto riguarda l'area superficiale e la porosità, i campioni a pH 7 hanno un'area superficiale media di $134 \pm 7,15 \text{ m}^2/\text{g}$, volume dei pori di $0,101 \pm 0,017 \text{ cm}^3/\text{g}$ e dimensione dei pori di $54,7 \pm 3,58 \text{ \AA}$. La sua superficie è la più alta rispetto ai campioni sintetizzati a pH diverso da 7, mentre la minore dimensione dei pori è da attribuire a CP- $\text{Cu}_2\text{O}-\text{SnO}_2$ -pH5,5 con un valore di $42,9 \text{ \AA}$ e il valore più alto del poro il volume è quello di CP- $\text{Cu}_2\text{O}-\text{SnO}_2$ -pH8 pari a $0,13 \text{ cm}^3/\text{g}$. Dall'osservazione dell'isteresi delle isoterme di adsorbimento, si può presumere che i pori di tutti i campioni di CP- $\text{Cu}_2\text{O}-\text{SnO}_2$ possano essere di forma cilindrica. La figura R2 confronta l'area superficiale, la dimensione dei pori e il volume dei pori di campioni di CP- $\text{Cu}_2\text{O}-\text{SnO}_2$ sintetizzati a pH diversi.

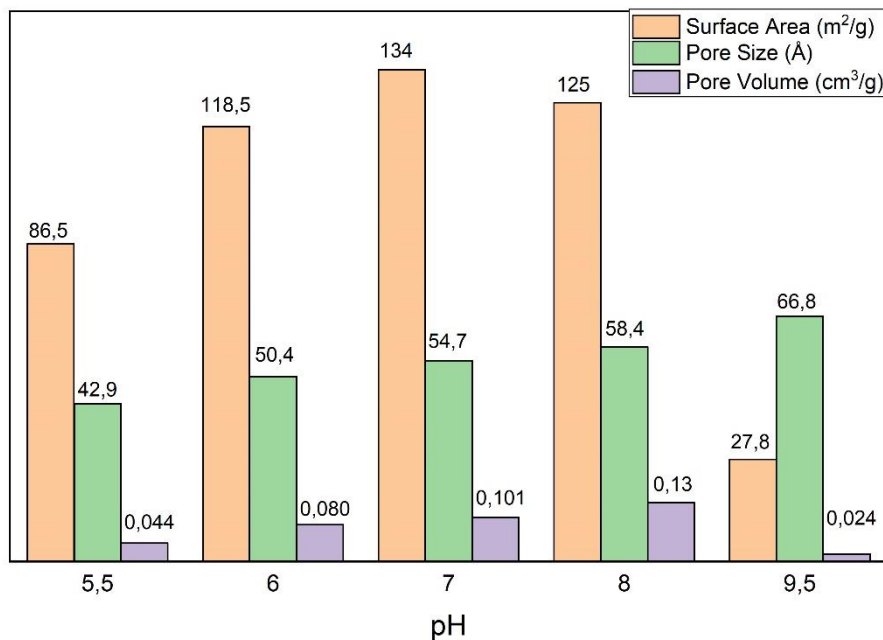


Figura R2: Area superficiale, dimensione e volume dei pori dei campioni CP-Cu₂O-SnO₂ a diversi pH.

Dallo spettro di assorbimento UV-Visibile e tramite il metodo Tauc plot sono stati ottenuti i valori di Energy Bandgap (Eg) dei campioni CP-Cu₂O-SnO₂. I campioni CP-Cu₂O-SnO₂-pH7 hanno un gap energetico di valore medio $2,51 \pm 0,02$ eV. Questo risultato è ragionevole, dato che dalla letteratura, il bandgap energetico di Cu₂O è di circa 2-2,2 eV, mentre quello di SnO₂ oscilla tra 3,58 e 3,8 eV. Gli altri campioni mostrano invece un valore di gap di energia di 4,25 eV, tranne il CP-Cu₂O-SnO₂-pH6 che ha un valore di Eg pari a 4,4 eV.

Dall'analisi complessiva dei dati raccolti, i CP-Cu₂O-SnO₂-pH7 sembrano essere i campioni in cui sono presenti esclusivamente Cu₂O e SnO₂, quelli con bandgap di energia inferiore e con area superficiale maggiore. Di conseguenza, si può affermare che il pH ottimale per la sintesi via coprecipitazione di Cu₂O e SnO₂ è 7. Per questo motivo si è deciso di non ripetere le sintesi a pH diversi. Per quanto riguarda la replicabilità dei campioni CP-Cu₂O-SnO₂-pH7, il bandgap energetico mostra un coefficiente di variazione percentuale dello 0,8%, l'area superficiale mostra un valore del 5% e una dimensione dei pori del 6,5%. Tuttavia, coefficienti di variazione percentuale più elevati sono relativi alla dimensione dei cristalli di Cu₂O e al volume dei pori con valori rispettivamente del 22,9% e del 16,8%. Pertanto la sintesi via coprecipitazione a pH 7 mostra una buona replicabilità. Nella tabella R4 sono riportati i coefficienti di variazione percentuale delle variabili precedentemente illustrate delle ripetizioni effettuate a pH 7.

Tabella R4: Coefficienti di variazione percentuale delle ripetizioni effettuate a pH7.

	Coefficienti di variazione percentuali(%)
Bandgap energetico	0,8
Area superficiale	5
Dimensione dei pori	6,5
Volume dei pori	16,8

Cu_2O crystal size	22,9
{220}/{200} PIR	9
{111}/{200} PIR	12,2

Per i campioni di Cu_2O sintetizzati via precipitazione con un vari reagenti, inizialmente si è cercato di aumentare la resa in ossido di rame(I) variando le concentrazioni ed i volumi delle soluzioni di sintesi per precipitazione con $\text{C}_6\text{H}_8\text{O}_6$. È stato possibile passare da una resa di circa l'86% per P1- Cu_2O -0,01-2-0.6-300 a circa il 99% per P1- Cu_2O -0,02-6-1.8-600, come mostrato in Figura R3.

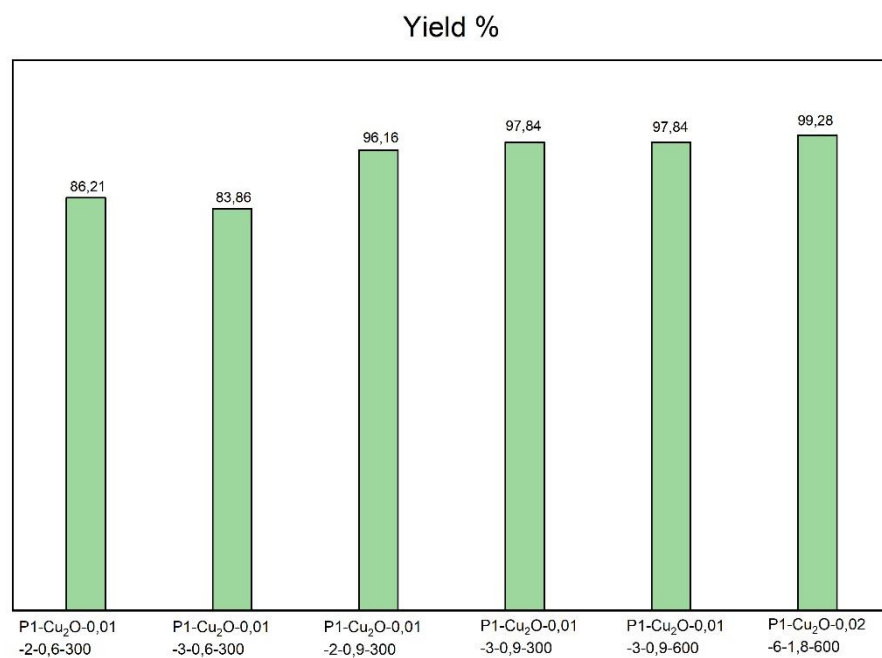


Figura R3: Resa dei campioni P1- Cu_2O .

Rese significativamente inferiori sono quelle ottenute per i campioni P1- Cu_2O -Et e per i campioni P2- Cu_2O . Le rese sono rispettivamente del 46% circa per P1- Cu_2O -0,02-6-1.8-300-Et0, del 39% circa per P1- Cu_2O -0,02-6-1.8-300-Et3, e del 44% circa e 50% per P2- Cu_2O _1 e P2- Cu_2O _2, rispettivamente. Questo perché l'HCl reagisce con il Cu_2O superficiale, modificando la forma cristallina e consumando contemporaneamente molecole di ossido di rame(I) secondo la reazione chimica (3.2.1.1) riportata nel capitolo 3.2.2.

Gli spettri XRD di tutti i campioni di Cu_2O sono chiari e i picchi ben definiti. Tutti i campioni presentano picchi relativi al solo ossido di rame(I), ad eccezione dei campioni P1- Cu_2O -Et, in cui è presente anche il Cu metallico. Il HCl ha ridotto una parte del prodotto desiderato a rame metallico. Questo non è il risultato sperato, ma può essere un interessante punto di partenza per la sintesi di catalizzatori misti Cu/ Cu_2O per la conversione elettrochimica della CO_2 in alcoli. Il rapporto di intensità tra i picchi {220} e {200} può essere un parametro per distinguere le diverse forme cristalline di Cu_2O . Secondo la metodologia sviluppata da Zhang et al., P1- Cu_2O -0,01-2-0.6-300 possiede nanocristalli di forma cubica, informazioni confermate dal figura R4.

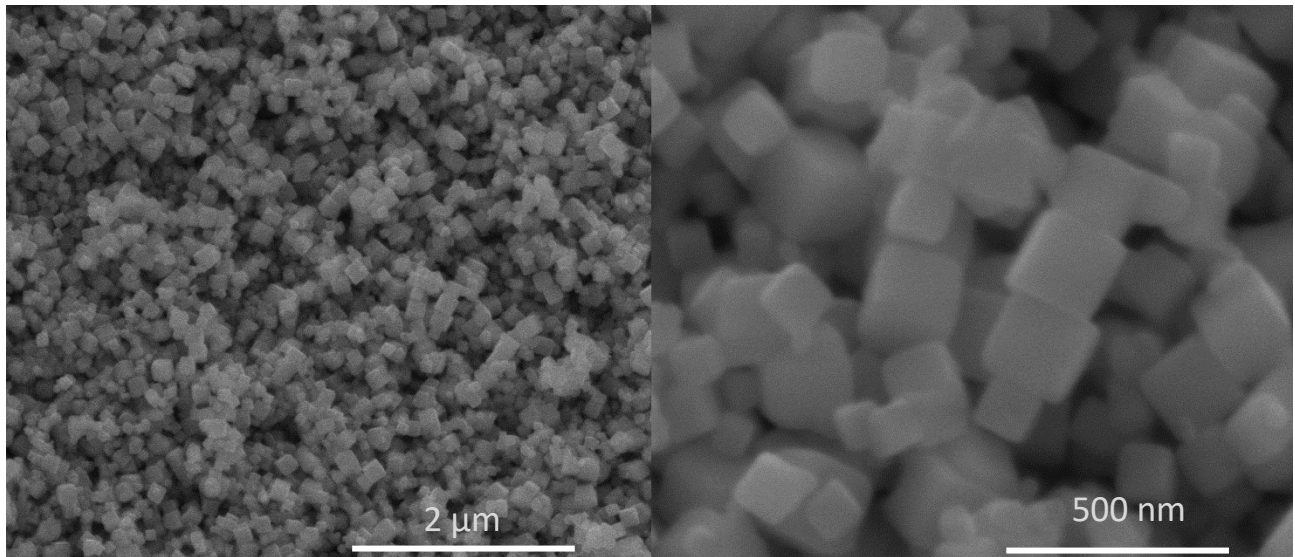


Figura R4: Immagine FESEM a diversi ingrandimenti del campone P1-Cu₂O-0.01-2-0.6-300.

Tuttavia i campioni di P1-Cu₂O sintetizzati mostrano rapporti di intensità tra i picchi {220} e {200} riconducibili ad una forma cristallina non certo cubica. Questi rapporti vanno da 0,6 a 0,7, dove 0,6 è relativo agli ottaedri troncati ai bordi e agli angoli, da 0,7 a {100} dodecaedri rombici troncati, mentre per i nanocubi questo rapporto è di circa 0,36. Un'altra informazione, che può dare validazione all'ipotesi della non cubicità della forma cristallina del Cu₂O, è la posizione del picco di maggiore intensità. Per i nanocubi, il picco di intensità del 100% è alla posizione di 42,5 gradi, rispetto al piano {200}, mentre per i campioni P1-Cu₂O questo picco è a circa 36,5 gradi, rispetto al piano {111}, una caratteristica tipica di cristalli ottaedrici. Dal FESEM nella figura R4, il campione P1-Cu₂O-0,01-2-0,6-300 sembra possedere cristalli cubici anche se gli spettri XRD possiedono le caratteristiche precedentemente menzionate. Probabilmente i cristalli hanno difetti non osservabili dal FESEM, ma rilevati dall'analisi XRD. Per i campioni P2-Cu₂O, la figura R5 al SEM mostra come i nanocristalli di Cu₂O ottenuti abbiano una forma più smussata, molto simile a quella rombica dodecaedrica, confermando la veridicità di questa metodologia di sintesi.

Dall'analisi EDX si evince che la composizione atomica del campione sintetizzato con C₆H₈O₆ è formata da 66,81% di Cu e 33,19% di O, mentre per il campione sintetizzato con Cloruro di Idrossilammonio la percentuale atomica è 52% di Cu, 46,5 % di O e 1,5% di Cl. La presenza di Cl può essere giustificata dal fatto che NH₂OH * HCl viene utilizzato come agente riducente e di conseguenza potrebbe rimanere una piccola quantità di cloro nel campione. Le analisi BET sono state effettuate su campioni P1-Cu₂O-0.02-6-1.8-600 e P1-Cu₂O-Et. Per tutti e tre i campioni la superficie è estremamente bassa, inferiore a 10 m²/g. Osservando l'isteresi delle curve isoterme, si nota che anche per P1-Cu₂O-0.02-6-1.8-600 i pori hanno probabilmente una forma cilindrica, mentre per i campioni P1-Cu₂O-Et l'isteresi è molto simile a quella isoterma curva, segno di una bassa porosità del materiale. Inoltre, P1-Cu₂O-0.02-6-1.8-600 è stato sottoposto a spettroscopia UV-Visibile. Utilizzando il metodo del diagramma Tauc, il valore di Energy bandgap ottenuto è di 2,4 eV, leggermente superiore ai valori riscontrati in letteratura.

Test RDE e PEC sono stati condotti su alcuni campioni sintetizzati. La cella elettrochimica utilizzata è suddivisa in due semicelle, comunicanti tra loro tramite una membrana bipolare. All'interno della semicella si trovano gli elettrodi, che sono conduttori del primo tipo, sui quali avvengono le semireazioni di ossidazione e di riduzione, immersi in una soluzione elettrolitica. L'elettrodo in cui avviene la semireazione di riduzione è detto catodo, mentre quello in cui

avviene la semireazione di ossidazione è detto anodo. La tipologia della cella è quella a tre elettrodi: l'elettrodo di lavoro (WE); l'elettrodo di riferimento (RE); il controelettrodo (CE). L'elettrodo di lavoro è quello in cui avviene la semireazione redox di interesse, dove si deposita l'inchiostro, che contiene il catalizzatore. L'elettrodo di riferimento ha un potenziale stabile, attraverso il quale è possibile controllare rigorosamente il potenziale applicato all'elettrodo di lavoro. Il controelettrodo è quello in cui avviene la seconda semireazione e rispetto al quale si misura la corrente di lavoro. Gli elettrodi sono collegati tramite terminali ad un potenziostato, grazie al quale è possibile ottenere informazioni sui campioni tramite tecniche, quali cronoamperometria (CA), cronopotenziometria (CP), voltammetria a scansione lineare (LSV) e voltammetria ciclica (CV). Nel CA il potenziale viene mantenuto costante e la corrente viene misurata in funzione del tempo, mentre nel CP la corrente è costante e il potenziale varia nel tempo. Nelle tecniche voltammetriche la corrente viene misurata in funzione del potenziale, che viene fatto variare linearmente nel LSV, mentre nel CV il potenziale varia con forma triangolare, crescendo linearmente fino ad un certo valore e poi decrescendo con andamento lineare tendenza. I test RDE sono test elettrochimici e l'elettrodo di lavoro è un elettrodo a disco rotante, sul quale viene depositato l'inchiostro, contenente il catalizzatore, all'interno del cerchio centrale scuro, costituito da un conduttore di prima specie, nel caso specifico carbone vetroso (*glassy carbon*), rivestito con un materiale polimerico, come il teflon. I test PEC sono invece test foto-elettrochimici, in cui è presente una lampada che emette luce visibile per simulare la luce solare. Attraverso questo tipo di test è possibile valutare il contributo della foto-attività e se tale contributo migliora significativamente le prestazioni del catalizzatore durante il test. In questo caso, l'elettrodo di lavoro è costituito da un supporto in carta di carbone, in cui l'area attiva è di 1 cm^2 , dove si deposita l'inchiostro contenente il catalizzatore. Per quanto riguarda l'elettrodo di riferimento, l'elettrodo Ag/AgCl (3,5 M KCl sat.) viene utilizzato come RE per entrambi i tipi di test. L'elettrodo Pt viene utilizzato come controelettrodo in entrambi i test e l'unica differenza è la forma del CE, a forma di retina nel test PEC e a forma di filo nel test RDE. La soluzione elettrolitica utilizzata è invece un KHCO_3 0,1 M per il test RDE. 50 mL di questa soluzione sono nella cella "catodo", in cui sono presenti WE e RE, e 29 mL sono nella cella "anodo", dove è presente CE. Per il test PEC, 28 mL di soluzione 0,1 M KOH sono nell'anodo, mentre 50 mL di soluzione 0,1 M KHCO_3 sono nel catodo. La Figura R6 e la Figura R7 mostrano i set up rispettivamente dei test RDE e PEC.

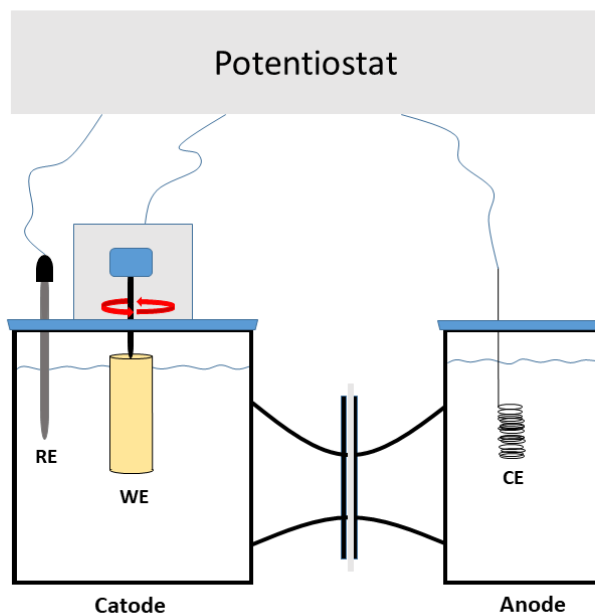


Figura R6: Set up dei test RDE.

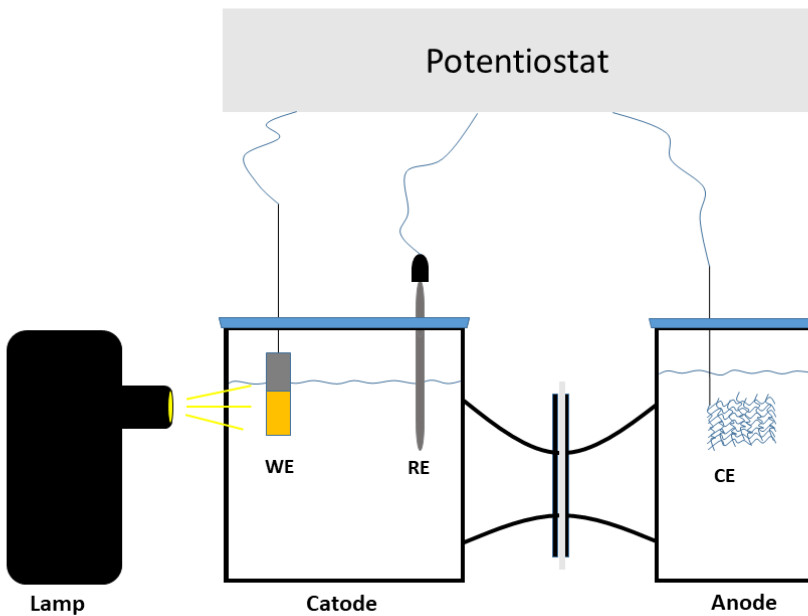


Figure R7: Set up dei test PEC

Per la preparazione degli inchiostri sono stati calcolati le percentuali dei componenti che lo costituiscono. L'inchiostro RDE è costituito dal 0,18 % di Vulcan Carbon, 1,90 % di catalizzatore 16,38 % di Nafion e 81,54 % g di iso-propanolo. Questa soluzione viene posta in ultrasuoni per circa 20 minuti in modo da avere un inchiostro il più omogeneo ed uniforme possibile. Il volume di inchiostro da depositare sull'elettrodo a disco rotante è tale da avere una carica di catalizzatore pari a 1 mg/cm^2 . Per l'inchiostro PEC, la sua composizione è costituita da 4,17 % di catalizzatore dal 12,5% di Nafion e dal 83,33% di Etanolo. Anche questa soluzione viene sonicata per 20 minuti e, tramite aerografo, viene spruzzata sulla carta carbone, posta su una lastra a 50°C per far evaporare il Nafion e l'etanolo. Infine, l'elettrodo utilizzato è quello con caricamento del catalizzatore pari a 1 mg/cm^2 .

I campioni testati nel test RDE sono P1-Cu₂O-0.02-6-1.8-300-Et0 e P1-Cu₂O-0.02-6-1.8-300-Et0, mentre quelli per il test PEC sono P1-Cu₂O-0.02-6-1.8-600, P1+I-Cu₂O-SnO₂_4 e CP-Cu₂O-SnO₂-pH7 e CP-Cu₂O-pH7-0.6-1-0.3. I risultati dei test saranno presentati confrontando i campioni per il metodo di sintesi e per le specie chimiche.

Nei campioni di test PEC è possibile calcolare il guadagno faradico della luce e osservare come varia nel tempo. La tabella 4.4.1 mostra il guadagno faradico medio della luce dei campioni testati. La figura R8 e la figura R9 presentano tendenze di guadagno faradico leggere nel tempo nella CA rispettivamente a -100 mV e -250 mV .

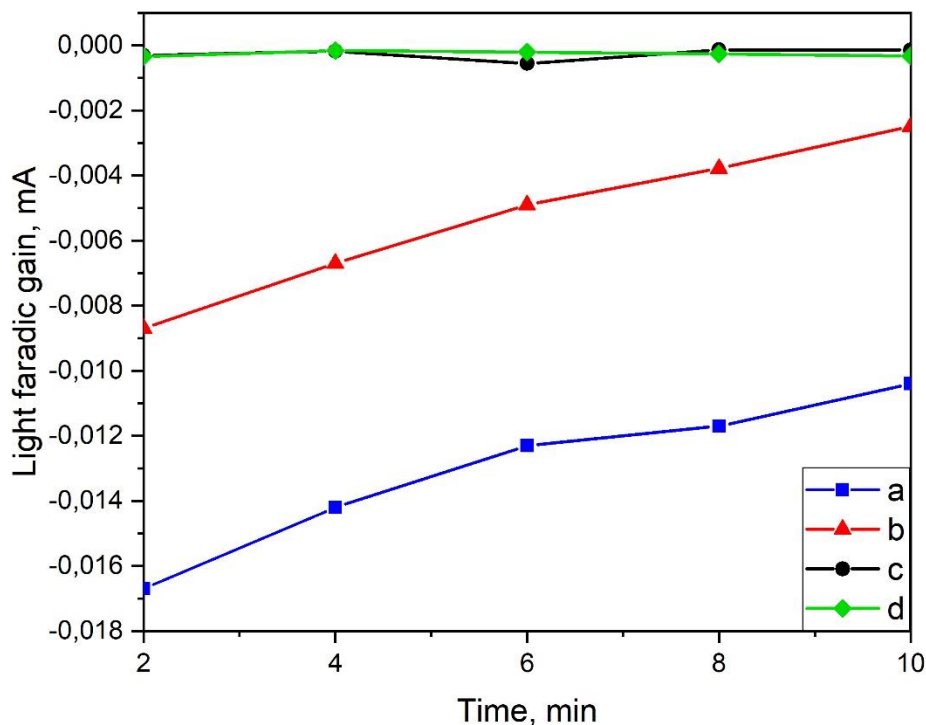


Figura R8: Andamento del guadagno faradico luminoso dei campioni a) P1-Cu₂O-0.02-6-1.8-600, b) P1+I-Cu₂O-SnO₂-4, c) CP-Cu₂O-pH7-0.6-1-0.3 and d) CP-Cu₂O-SnO₂-pH7 durante la CA a -100 mV.

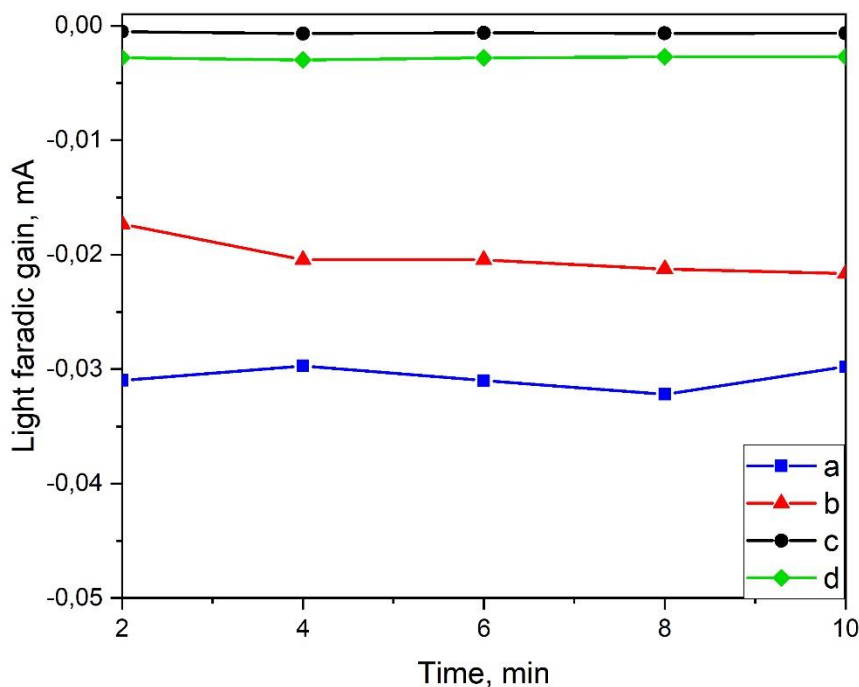


Figura R9: Andamento del guadagno faradico luminoso dei campioni a) P1-Cu₂O-0.02-6-1.8-600, b) P1+I-Cu₂O-SnO₂-4, c) CP-Cu₂O-pH7-0.6-1-0.3 and d) CP-Cu₂O-SnO₂-pH7 durante la CA a -250 mV.

Dalle figure R8 e R9 si può notare che il campione P1-Cu₂O-0.02-6-1.8-600 presenta i maggiori guadagni faradici della luce con valori pari a -0.0131 mA e -0.0307 mA, seguiti dal campione P1+I-Cu₂O-SnO₂-4 con guadagni faradici della luce pari a -0,0052 mA e -0,0203 mA. Valori molto più bassi sono quelli dei campioni sintetizzati con il metodo della coprecipitazione. In particolare il campione CP-Cu₂O-pH7-0.6-1-0.3 mostra valori pari a -0.0002662 mA e -0.00065 mA, mentre il campione CP-Cu₂O-SnO₂-pH7 mostra valori di guadagno faradico della luce pari a -0,0002587 mA e -0,00280 mA. Questi valori possono essere giustificati ragionando sulle specie chimiche presenti nei campioni testati. Il campione P1-Cu₂O-0.02-6-1.8-600 è costituito esclusivamente da Cu₂O, mentre il P1+I-Cu₂O-SnO₂-4 ha uno 0,33% di Sn che potrebbe aver influenzato negativamente il guadagno faradico della luce, riducendone il valore. Stesso ragionamento può essere applicato a CP-Cu₂O-SnO₂-pH7 in cui SnO₂ è presente in quantità maggiori rispetto a P1+I-Cu₂O-SnO₂-4, essendo osservabile dall'analisi XRD. D'altra parte, per il campione CP-Cu₂O-pH7-0.6-1-0.3 la presenza di Cu metallico potrebbe essere causa di bassi valori di guadagno faradico, poiché il Cu metallico non è foto-attivo. Osservando gli andamenti del guadagno faradico, si può osservare che le curve a -250 mV variano meno di quelle a -100 mV, in particolare per P1-Cu₂O-0,02-6-1.8-600 e P1+I-Cu₂O-SnO₂-4 campioni. Probabilmente questo è dovuto al fatto che, applicando un potenziale maggiore, il materiale è più attivo e, di conseguenza, più stabile nello sfruttamento del contributo luminoso. La figura R10 e la figura R11 mostrano le efficienze faradiche dei campioni di test PEC e dei campioni di test RDE rispettivamente.

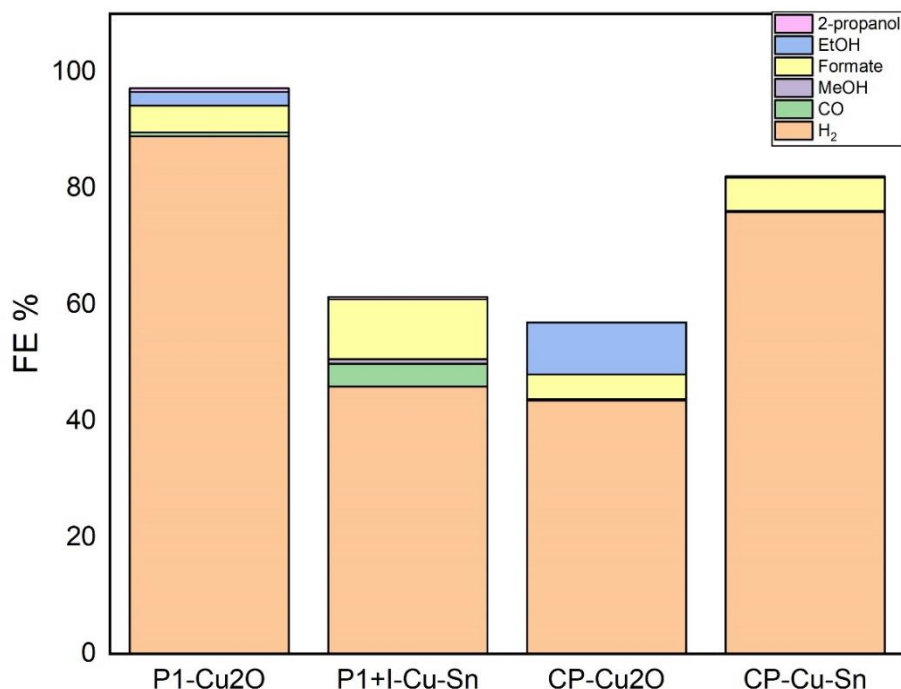


Figura R10: Efficienze faradiche dei campioni testati al tes PEC.

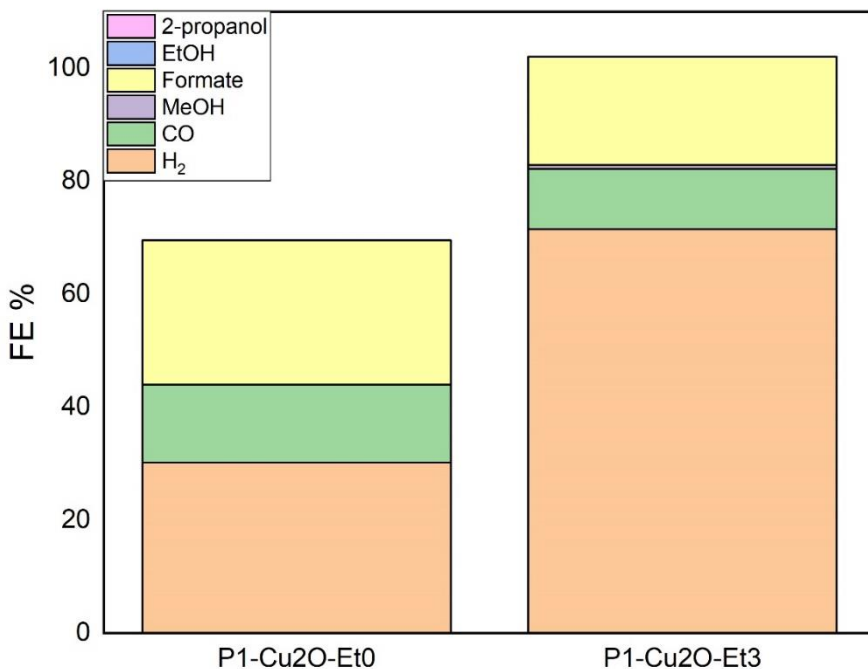


Figura R11: Efficienze faradiche dei campioni testati al test RDE.

Per quanto riguarda le efficienze faradiche dei campioni di prova PEC, i campioni con Sn hanno efficienze faradiche di HCOOH maggiore rispetto ai corrispondenti campioni privi di stagno. In particolare, P1+I-Cu₂O-SnO₂-4 ha un'efficienza faradica del 10,27%, mentre P1-Cu₂O-0,02-6-1.8-600 mostra un valore del 4,62%, circa due volte inferiore. Per il campione CP-Cu₂O-SnO₂-pH7, invece, FE di HCOOH è del 5,73%, leggermente superiore a quello del CP-Cu₂O-pH7-0,6-1-0,3 di circa il 4,28%. Questo aumento di FE del formiato è dovuto alla presenza di ossido di stagno (IV), che è un buon catalizzatore per la riduzione elettrochimica della CO₂ a formiato. Osservando l'FE di CO, solo il P1+I-Cu₂O-SnO₂-4 mostra un valore superiore all'unità e pari al 3,89%. Inoltre, è interessante osservare come il campione CP-Cu₂O-pH7-0,6-1-0,3 mostri un discreto FE verso l'etanolo di circa l'8,91 %.

Dai test RDE i campioni mostrano buone efficienze faradiche di CO e HCOOH con valori pari al 13,81% e 25,50% per il P1-Cu₂O-0,02-6-1.8-300-Et0 e 10,69% e 19,16% per il P1-Cu₂O-0,02-6-1.8-300-Et3 rispettivamente. Osservando il FE dell'idrogeno, si può notare che il campione P1-Cu₂O-0,02-6-1.8-300-Et0 ha un'efficienza faradica del 30,14%, mentre P1-Cu₂O-0,02-6-1.8-300-Et3 del 71,48%. Ciò potrebbe essere giustificato osservando gli spettri XRD dei due campioni. P1-Cu₂O-0,02-6-1.8-300-Et0 mostra un rapporto di intensità tra i picchi massimi di Cu₂O e quello di Cu metallico pari a 0,046, mentre tale rapporto è 0,618 per P1-Cu₂O-0,02-6-1,8-300- Et3. Ciò suggerisce che nel campione P1-Cu₂O-0,02-6-1.8-300-Et3 vi sia una percentuale di Cu metallico maggiore rispetto a P1-Cu₂O-0,02-6-1.8-300-Et0. Poiché il Cu metallico è molto più conduttivo del Cu₂O potrebbe aver favorito la reazione di scissione dell'acqua, determinando così una maggiore FE di H₂ nel campione P1-Cu₂O-0,02-6-1.8-300-Et3. Estremamente bassi o nulli sono gli FE di metanolo, etanolo e 2-propanolo per entrambi i campioni.

Contents

1. Introduction.....	1
1.1. Global warming and strategies to mitigate it.....	1
1.2. Photo-Electrochemical reduction of Carbon Dioxide.....	2
1.3. Cu forms for Photo-Electrochemical CO ₂ Conversion.....	5
1.4. Rhombic Dodecahedral Cu ₂ O Synthesis Methods.....	9
1.5. Cu ₂ O Instability.....	10
1.6. The aim of the thesis.....	10
2. Materials and Methods.....	11
2.1. Materials and instruments.....	11
2.1.1. Materials and instruments for Coprecipitation catalyst synthesis.....	11
2.1.2. Materials and instruments for Core-Shell catalyst synthesis.....	11
2.2. Methods of synthesis.....	13
2.2.1. Cu ₂ O-SnO ₂ Coprecipitation catalyst synthesis.....	13
2.2.1.1. Synthesis at pH 7.....	14
2.2.1.2. Synthesis at acid pH.....	16
2.2.1.3. Synthesis at basic pH.....	17
2.2.1.4. Synthesis of Cu ₂ O by the Coprecipitation method without Sn precursor.....	18
2.2.2. Cu ₂ O-SnO ₂ Core-Shell catalyst synthesis.....	20
2.2.2.1. Synthesis of Cu ₂ O with C ₆ H ₈ O ₆ as reducing agent.....	20
2.2.2.2. Synthesis of Cu ₂ O with C ₆ H ₈ O ₆ and Acid Etching Step.....	22
2.2.2.3. Synthesis of Cu ₂ O with SDS and NH ₂ OH*HCl as reducing agent.....	23
2.2.2.4. Synthesis of Cu ₂ O-SnO ₂ Core-Shell catalyst.....	25
3. Characterization.....	27
3.1. Cu ₂ O-SnO ₂ Coprecipitation Synthesis.....	29
3.1.1. Cu ₂ O-SnO ₂ Coprecipitation Catalyst.....	29
3.1.1.1. XRD.....	29
3.1.1.2. BET.....	32
3.1.1.3. UV-visible absorption spectroscopy.....	35
3.1.2. Cu ₂ O synthesized by the Coprecipitation method without Sn precursor.....	37
3.1.2.1. XRD.....	37
3.1.2.2. UV-visible absorption spectroscopy.....	38
3.1.3. Results Discussion.....	39
3.2. Cu ₂ O – SnO ₂ Core-Shell Synthesis.....	43
3.2.1. Cu ₂ O with C ₆ H ₈ O ₆ as reducing agent.....	43
3.2.1.1. Yield.....	43
3.2.1.2. XRD.....	45
3.2.1.3. FESEM and EDX.....	47
3.2.1.4. BET.....	48
3.2.1.5. UV-visible absorption spectroscopy.....	49
3.2.2. Cu ₂ O synthesized with C ₆ H ₈ O ₆ and additional Acid Etching Step.....	50

3.2.2.1. Yield.....	50
3.2.2.2. XRD.....	50
3.2.2.3. BET.....	52
3.2.3. Cu ₂ O synthesized with SDS and NH ₂ OH*HCl as reducing agent.....	53
3.2.3.1. Yield.....	53
3.2.3.2. XRD.....	53
3.2.3.3. SEM and EDX.....	55
3.2.4. Cu ₂ O-SnO ₂ Core-Shell catalyst.....	57
3.2.4.1. XRD.....	57
3.2.4.2. SEM and EDX.....	58
3.2.4.3. BET.....	59
3.2.4.4. UV-visible absorption spectroscopy.....	60
3.2.5. Results Discussion.....	61
3.2.5.1. Cu ₂ O samples.....	61
3.2.5.2. Cu ₂ O-SnO ₂ Core-Shell samples.....	62
4. Test.....	63
4.1. Comparison of test results by synthesis method.....	65
4.1.1. Comparison between P1-Cu ₂ O-0.02-0.6-1.8-600 and P1+I-Cu ₂ O-SnO ₂ -4.....	65
4.1.2. Comparison between CP-Cu ₂ O-pH7-0.6-1-0.3 and CP-Cu ₂ O-SnO ₂ -pH7.....	70
4.2. Comparison of test results by chemical species.....	75
4.2.1. Comparison between CP-Cu ₂ O-pH7-0.6-1-0.3 and P1-Cu ₂ O-0.02-6-1.8-600.....	75
4.2.2. Comparison between CP-Cu ₂ O-SnO ₂ -pH7 and P1+I-Cu ₂ O-SnO ₂ -4.....	80
4.2.3. Comparison between P1-Cu ₂ O-0.02-6-1.8-300-Et0 and P1-Cu ₂ O-0.02-6-1.8-300-Et3.....	85
4.3. Comparison of Light Faradic Gains.....	89
4.4. Comparison of Faradica Efficiencies.....	91
5. Conclusions.....	95
References.....	97
Copyright.....	101
Acknowledgements.....	103

1 Introduction

1.1 Global warming and strategies to mitigate it

In the recent years, the Scientific Society has focused its attention on problems related to Global Warming. The main causes of this phenomenon are connected to increasing emissions of greenhouse gases, linked to industrial processes to satisfy the more and more demanding human needs. Greenhouse gases are those gases present in the atmosphere that are able to retain a part of solar radiation, which hits planet Earth and is subsequently released by the earth's surface and atmosphere. One of the most harmful gases is carbon dioxide (CO_2). The natural world keeps under control the CO_2 concentration with the “Carbon Cycle”, which is a balance between the amount of carbon released and that potentially absorbed by the environment. Despite this, the concentration of atmospheric CO_2 raised from 280 ppm in the pre-industrial age to a value close to 420 ppm in 2020 [1], due to the increasing use of fossil fuel, related to anthropic activities (e.g. transportation, electrical and thermal energy, etc.). Figure 1.1 shows a trend of emitted CO_2 in the atmosphere in the last decades.

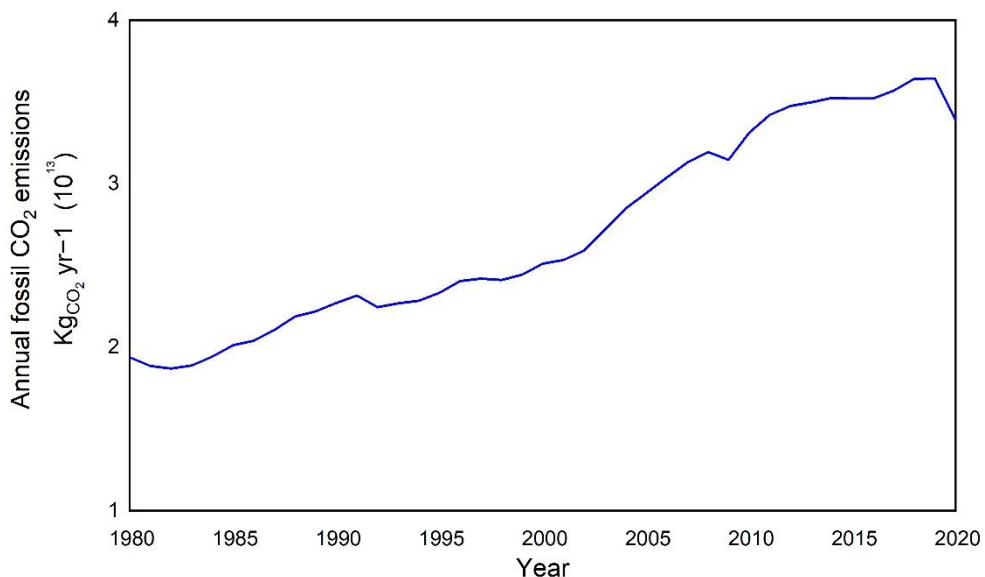


Figure 1.1: Annual fossil CO_2 emissions for 1980-2020 in Kg yr^{-1} . From ref. [2] with modifications.

Greenhouses gases limit dispersion of residual sunlight radiation out of the “Earth system”, determining an accumulation of thermal energy in the system. Visible consequences of this problem are extreme changes in the mountain glaciers, the Arctic Polar Circle, Greenland and the West Antarctic Ice Sheet. From the late 1970s to the 2000s, the Arctic summer sea ice lost more than 10% of its area per decade. If this trend persists, it has been estimated that the Arctic could become ice-free in summer for the first time within the 21st century. Approximately 600 glaciers have vanished in this timeframe and many more are likely to follow the same fate in the future. Moreover, a negative feedback comes from the West Antarctic and the Greenland Ice Sheet, which have reduced their ice mass with a growing pace during these years [3].

Ongoing researches have been directed on the finding of ways for minimizing carbon dioxide production and its recycling for synthesizing valuable chemicals. Production of energy from “green” sources can be an interesting challenge to curb CO₂ emissions and content the global primary energy supply. Presently, renewed resources provide 15% of the worldwide primary energy, in which 10% comes from bioenergy, 3% from hydropower and the rest 2% from other renewables like wind and solar energy. The World Energy Outlook and integrated assessment models (IAMs) assess that renewables may cover 20–30% of the world energy requirements by 2040 [4]. If the green strategy is aimed to avoid the problem in the first place, another approach is to see CO₂ as a source of carbon to produce fuel. The purpose is to convert carbon dioxide into value-added products by its reduction reaction. Pairing these two solutions, it is possible to satisfy the total power demand.

1.2 Photo-Electrochemical reduction of Carbon Dioxide

The reduction of carbon dioxide (CO₂RR) is a complex process, in which a large number of proton-coupled electron transfer reactions are involved. Because of its double covalent bonds, carbon dioxide presents slow kinetics and high thermodynamic stability. For these reasons, most of CO₂RRs are unfavorable at ambient temperature and pressure (as shown in Table 1.1).

Table 1.2.1. The Gibbs Free Energy for the Reduction Reactions of CO₂ at standard conditions. From [5] with modifications.

CO ₂ RRs	ΔG° (kJ/mol)
CO ₂ (g) → CO (g) + ½ O ₂ (g)	257
CO ₂ (g) + H ₂ O (l) → HCOOH (l) + ½ O ₂ (g)	275
CO ₂ (g) + H ₂ O (l) → HCHO (l) + O ₂ (g)	520
CO ₂ (g) + H ₂ O (l) → CH ₃ OH (l) + 3/2 O ₂ (g)	703
CO ₂ (g) + H ₂ O (l) → CH ₄ (g) + 2O ₂ (g)	818
CO ₂ + H ₂ → CO + H ₂ O (g)	28.6
CO ₂ + H ₂ → HCOOH (l)	33
CO ₂ + 3H ₂ → CH ₃ OH + H ₂ O (l)	-9
CO ₂ + 4H ₂ → CH ₄ + 2H ₂ O (g)	-113.5
2CO ₂ + 6H ₂ → C ₂ H ₄ + 4H ₂ O (g)	-57.32
3CO ₂ + 9H ₂ → C ₃ H ₆ + 6H ₂ O (g)	-125.69

In addition, for spontaneous reactions at ambient conditions, which have negative Gibbs Free Energy, the number of electrons required for reduction is high such as to make extremely difficult a one-step reaction, in particular a not catalyzed reaction. Table 1.2 sums up some electrochemical half-reactions for CO₂ reduction with relative standard potentials E⁰ (at 1 atm and 25 °C).

Table 1.2. Electrochemical half-reactions for CO₂ reduction with standard potentials E⁰ at pH 0 in aqueous solution versus NHE. From [5] with modifications.

Proton-coupled electron transfer reactions of CO ₂	ΔE ⁰ (V vs. NHE)
CO ₂ (g) + 2H ⁺ + 2e ⁻ → HCOOH(l)	-0.2
CO ₂ (g) + 2H ⁺ + 2e ⁻ → CO(g) + H ₂ O(l)	-0.12
CO ₂ (g) + 4H ⁺ + 4e ⁻ → HCHO(l) + H ₂ O(l)	0.07
CO ₂ (g) + 6H ⁺ + 6e ⁻ → CH ₃ OH(l) + H ₂ O(l)	0.03
CO ₂ (g) + 8H ⁺ + 8e ⁻ → CH ₄ (g) + 2H ₂ O(l)	0.17
2CO ₂ (g) + 8H ₂ O(l) + 12e ⁻ → C ₂ H ₄ (g) + 12OH ⁻	0.07
2CO ₂ (g) + 9H ₂ O(l) + 12e ⁻ → C ₂ H ₅ OH(l) + 12OH ⁻	0.08

According to previous kinetic and thermodynamic considerations, it is necessary to use a catalyst to carry out the reaction. Electrochemical catalysis and photocatalysis can be promising strategies for carbon dioxide conversion at ambient conditions, because the first use electricity, possibly produced by renewables, and the second exploits solar radiation to lead reaction.

Due to its versatility, electrochemical reduction of CO₂ could allow to synthesize a large number of valuable industrial commodities. An effective electrocatalyst must decrease the CO₂ reduction overpotentials and be highly stable and selective, controlling the reaction pathways toward a specific product. However, the majority of the high-performance electrocatalysts in the aqueous electrolyte are based on noble metals, limiting their applicability at laboratory scale for high costs and poor abundance [6]. Due to the complexity of its kinetic reactions, the main products are carbon monoxide (CO) and formic acid (HCOOH), where the involved electrons are only two. Au, Ag and Pd-based catalysts promote the conversion of CO₂ to CO in the common aqueous electrolyte solution of KHCO₃, meanwhile Sn, In, Pb and Bi are selective for the reduction to formate. Contrary to catalysts mentioned above, Cu is an interesting transition metal, particularly active to enhance the reduction reactions of CO₂ to several products, like CO, HCOOH and hydrocarbons [7].

Photo-catalysis is a process based on the absorption of photons, which activate the catalyst. This process needs the utilization of catalysts with metal or semiconductor properties. A photon with energy greater or equal to the bandgap energy ($h\nu \geq E_g$) is absorbed on semiconductor surface, where photon energy is used to favor an electron transfer from the valence band (VB) to the conduction band (CB) [8]. To photo-catalyze CO₂ reduction reactions, in addition to noble metals, a wide range of semiconductors are investigated (e.g. ZnO, α-Fe₂O₃, TiO₂, etc.) and, of these, TiO₂ has been proposed to be the most appropriate photo-catalyst for solar fuel production, due to its availability in nature and significant chemical stability. A not negligible aspect is related to the wide bandgap energy of Titania (3.0–3.2 eV), which restricts absorbed sunlight to the ultraviolet region, limiting conversion efficiency [9]. This is a disadvantage of most semiconductor-based catalysts, which are characterized by mediocre sunlight utilization and insufficient interaction with CO₂. The following Table 1.3 presents a list of typical semiconductors, used for photo-catalysis, and related energy bandgap.

Table 1.3: Comparison of the Band Gap Structures of Typical Semiconductors (pH =7, vs NHE). From [5] with modifications.

Catalyst	CB	VB	E _g (eV)
Si	-0.81	0.29	1.1
TiO ₂ (anatase)	-0.50	2.7	3.2
TiO ₂ (rutile)	-0.32	2.7	3.02
SrTiO ₃	-0.75	2.75	3.5
ZnO	-0.61	2.58	3.2
Cu ₂ O	-1.16	0.85	2.0
SnO ₂	0.04	3.54	3.5
CdS	-0.9	1.5	2.4
Ta ₃ N ₅	-0.75	1.35	2.1
TaON	-0.75	1.75	2.5
WO ₃	-0.1	2.7	2.8
α -Fe ₂ O ₃	-0.03	2.17	2.2
BiVO ₄	-0.3	2.17	2.4

Photoelectrochemical CO₂ reduction can be seen like “artificial photosynthesis”, where the photo and electrochemical catalysis are combined to form a more efficient system. In comparison to conventional methods, photo/electrochemical systems present several advantages in terms of efficiency, environmental compatibility, high selectivity and ease of work-up. For example, redox reagents in the electrochemical synthesis can be either replaced by electric current or in-situ generated at electrodes, allowing the transformation to take place with the deletion of beginning reagents. In addition, the kinetics of electrochemical reactions can be sped up by the electrode potential, which promotes the reactions with high activation energy at low temperatures. In the case of photochemical reactions, the electrode potential is replaced by photoirradiation, which enhances the conversion of reactants into active radical intermediates to work at mild conditions. From these merits, the photo-electrochemical reduction of CO₂ into valuable products seems to be more attractive and convenient compared to other catalytic strategies [10].

1.3 Cu forms for Photo-Electrochemical CO₂ conversion

Cu compounds are interesting catalysts towards carbon dioxide, thanks to their good multielectron transfer properties due to their loosely bonded electrons. Among them, the most promising catalysts are metallic copper (Cu), copper(I) oxide (Cu₂O) and copper(II) oxide (CuO). However, only Cu₂O shows photocatalytic properties. Cu₂O is a direct-bandgap semiconductor with a bandgap value close to 2 eV, which makes copper(I) oxide able to absorb visible light that constitutes a bigger fraction of the solar spectrum. Due to the presence of negatively charged Cu vacancies, it presents intrinsic p-type conductivity and has one of the lowest electron affinities of the elements. Moreover, because of the abundance of its constituent elements, Cu₂O is a relatively cheap material. Thanks to these advantages, Cu₂O is a good candidate for the reduction of CO₂ [11].

Because of its crystalline nature, Cu₂O has several morphologies of its crystals, which determine different photo activities. Cu₂O morphologies are the following ones: cubes; face-raised cubes; edge- and corner truncated octahedra; all-corner-truncated rhombic dodecahedra; {100}-truncated rhombic dodecahedra; rhombic dodecahedra. Its photocatalytic activity has been estimated by the photodegradation of methyl orange and results show that photo-activity increases passing from the cubes, which are the least photoactive, to rhombic dodecahedral structure, where degradation of methyl orange is fast and complete [12]. Therefore rhombic dodecahedral Cu₂O can be a powerful catalyst for other photo-catalytic reactions, as well as photo-electrochemical reactions. Figure 1.2 presents the just mentioned crystal shapes.

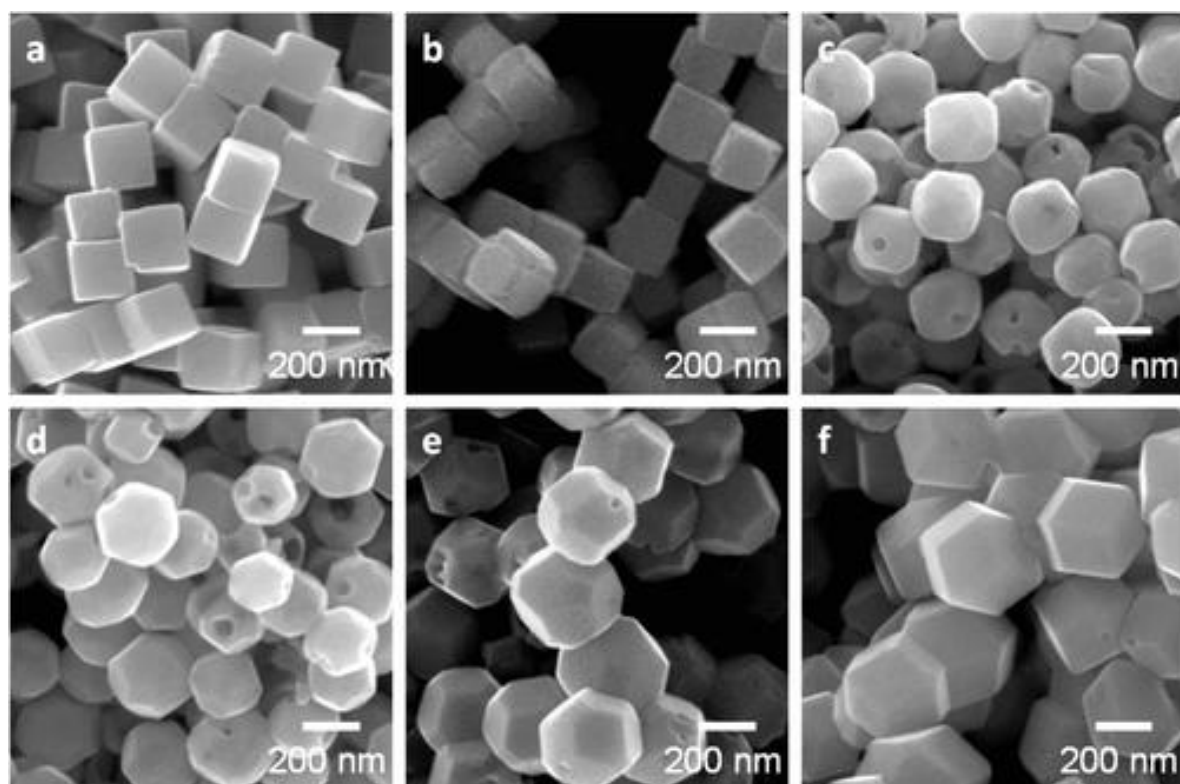


Figure 1.2: SEM images of the Cu₂O nanocrystals synthesized with various morphologies: (a) cubes, (b) face-raised cubes, (c) edge- and corner truncated octahedra, (d) all-corner-truncated rhombic dodecahedra, (e) {100}-truncated rhombic dodecahedra, and (f) rhombic dodecahedra. “Reprinted (adapted) with permission from {Wan-Chen Huang, Lian-Ming Lyu, Yu-Chen Yang and Michael H. Huang, *Synthesis of Cu₂O Nanocrystals from Cubic to Rhombic Dodecahedral Structures and Their Comparative Photocatalytic Activity*, J. Am. Chem. Soc. 2012, 134, 1261–1267}. Copyright {2021} American Chemical Society”.

A study, published by Liu et al. [13], shows a method to synthesize Cu₂O, with different crystalline forms, decorated with reduced graphene oxide (rGO) and compares them in the photoreduction of CO₂. The crystalline structures of Cu₂O considered are the cubic, octahedral and rhombic dodecahedral one. Rhombic dodecahedral Cu₂O/rGO exhibits the best CH₃OH yield after being illuminated by visible light for 20 h. This highlights the characteristic of the rhombic dodecahedral form to be more active in the photoreduction of CO₂, in particular towards the methanol formation. Probably, this is due to the less band bending of CB and VB of rhombic dodecahedral copper(I) oxide and consequently lower barrier to the transfer of photogenerated electrons to the surface. Other differences between the crystalline forms can be seen from characterization techniques such as XRD, TEM and UV-vis absorption spectrum. XRD patterns appear similar, because of random crystals orientations, but a more accurate analysis highlights that the ratio of the intensity of the {220} peak to that of the {200} peak rises from 0.36 for the cubes to 0.6, 0.7, and 0.79 for the edge- and corner-truncated octahedra, {100}-truncated rhombic dodecahedra and rhombic dodecahedra, respectively. This is probably due to the increasing fractions of {110} faces.

Figure 1.3 gives information about the TEM images, selected-area electron diffraction (SAED) patterns and high-resolution TEM images of Cu₂O edge- and corner-truncated octahedra observed along the {100}, {110}, and {111} directions. The high-resolution TEM images reveal clear lattice fringes with d spacings of 2.4 and 2.9 Å, which reflect the {111} and {110} planes of Cu₂O.

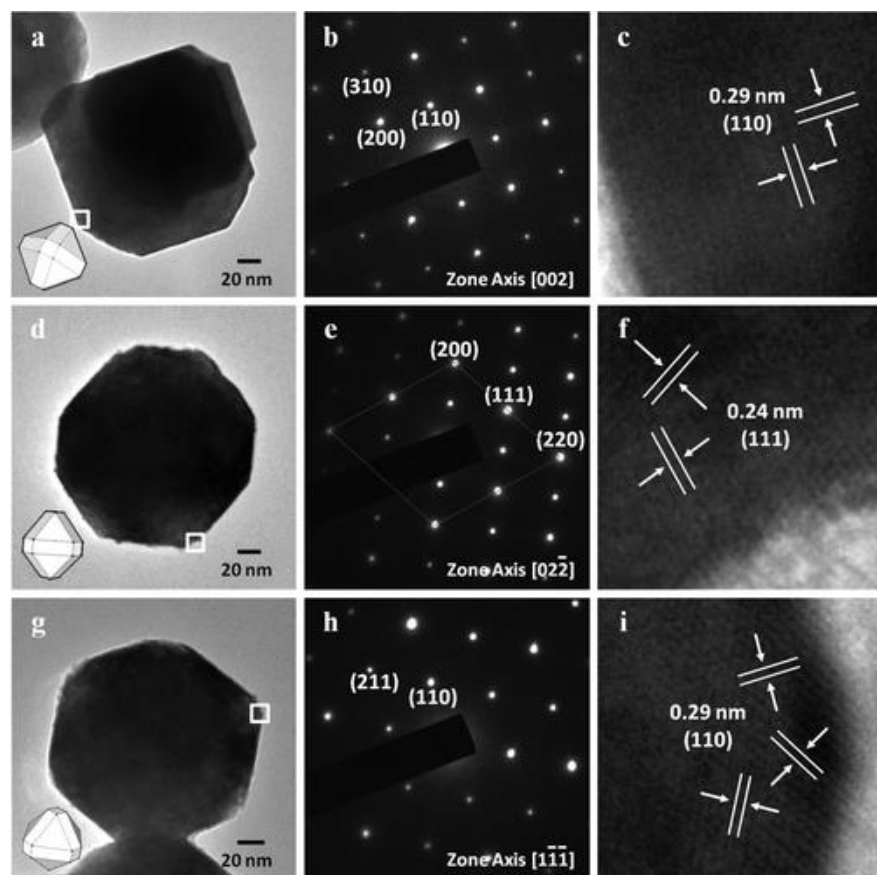


Figure 1.3: TEM images, SAED patterns and high-resolution TEM images of the square regions of Cu₂O edge- and corner-truncated octahedra viewed along the (a-c) [100], (d-f) [110], and (g-i) [111] directions. From [12] with modifications. “Reprinted (adapted) with permission from {Wan-Chen Huang, Lian-Ming Lyu, Yu-Chen Yang and Michael H. Huang, *Synthesis of Cu₂O Nanocrystals from Cubic to Rhombic Dodecahedral Structures and Their Comparative Photocatalytic Activity*, J. Am. Chem. Soc. 2012, 134, 1261–1267}. Copyright {2021} American Chemical Society”.

Figure 1.4 gives information about the TEM images, SAED patterns and high-resolution TEM images of Cu₂O all-corner-truncated rhombic dodecahedra observed along the {100}, {110}, and {111} directions. Due to the fact that the {111} surface area of these nanocrystals is small, it can be difficult to find an isolated all-corner-truncated rhombic dodecahedron positioned along the [111] zone axis.

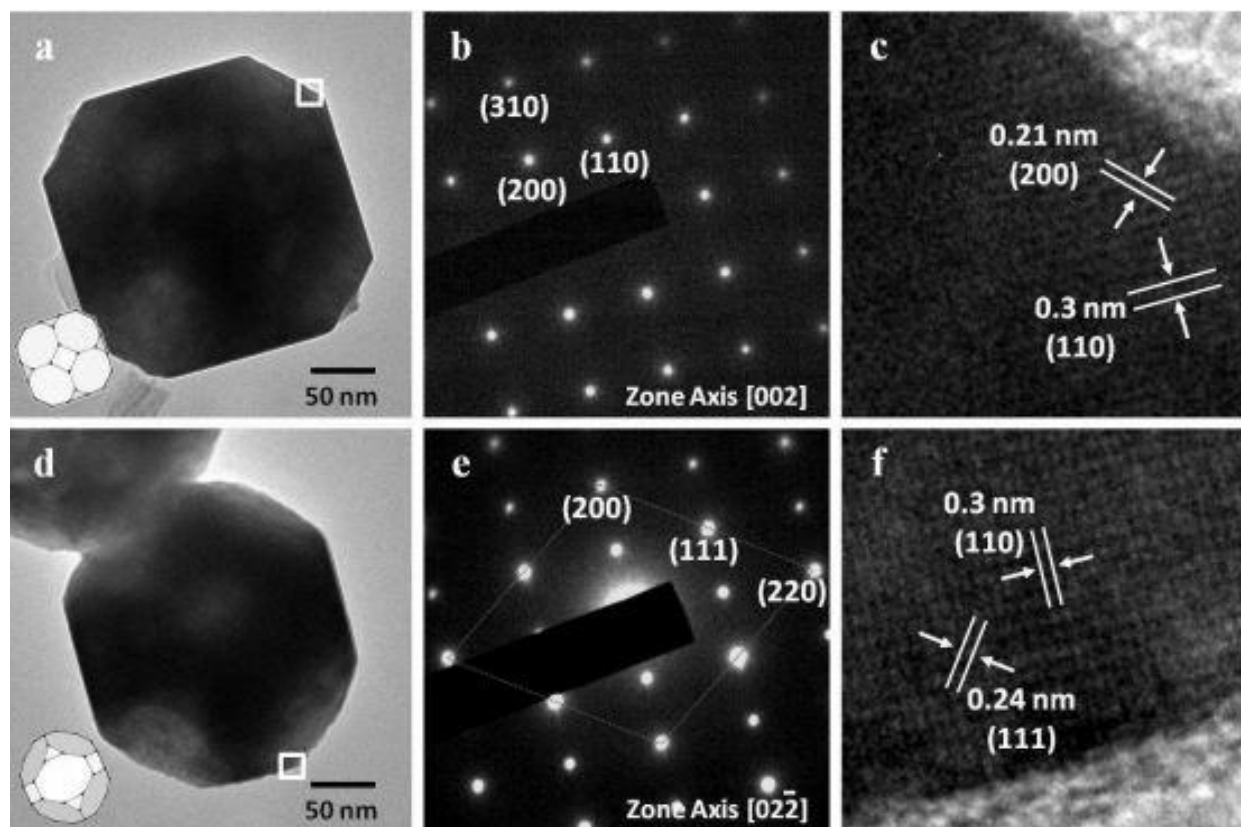


Figure 1.4: TEM images, SAED patterns, and high-resolution TEM images of the square regions of Cu₂O all-corner-truncated rhombic dodecahedra viewed along the (a–c) [100], (d–f) [110], and (g–i) [111] directions. From [12] with modifications. “Reprinted (adapted) with permission from {Wan-Chen Huang, Lian-Ming Lyu, Yu-Chen Yang and Michael H. Huang, *Synthesis of Cu₂O Nanocrystals from Cubic to Rhombic Dodecahedral Structures and Their Comparative Photocatalytic Activity*, J. Am. Chem. Soc. 2012, 134, 1261–1267}. Copyright {2021} American Chemical Society”.

Figure 1.5 presents the TEM images and the corresponding SAED patterns of rhombic dodecahedra viewed along the [100], [110], and [111] directions. These SAED patterns are coherent with those of the particle surfaces bounded by the {110} facets.

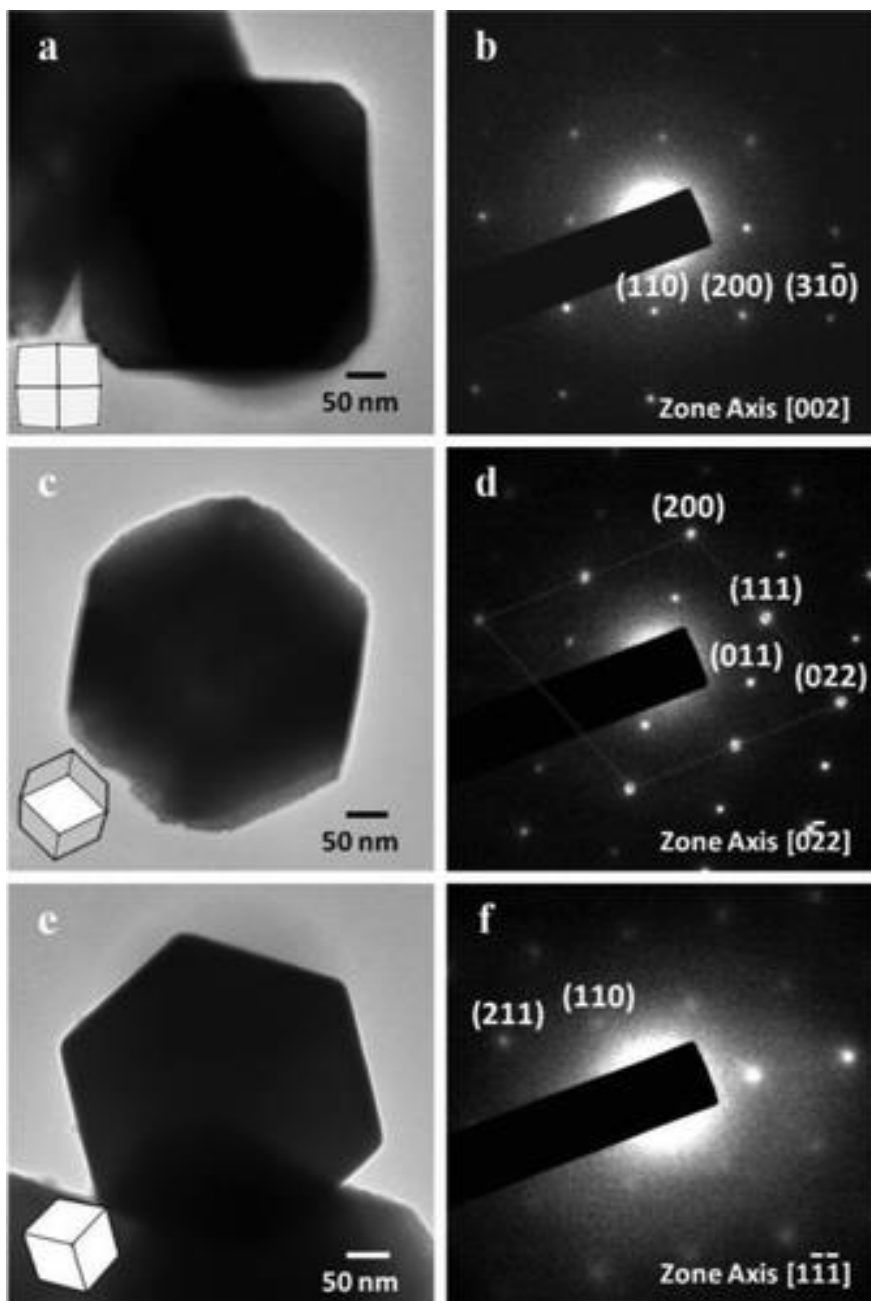


Figure 1.5: TEM images of Cu_2O rhombic dodecahedra viewed along the (a) [100], (c) [110], and (e) [111] directions and their corresponding SAED patterns. “Reprinted (adapted) with permission from {Wan-Chen Huang, Lian-Ming Lyu, Yu-Chen Yang and Michael H. Huang, *Synthesis of Cu_2O Nanocrystals from Cubic to Rhombic Dodecahedral Structures and Their Comparative Photocatalytic Activity*, J. Am. Chem. Soc. 2012, 134, 1261–1267}. Copyright {2021} American Chemical Society”.

Information of optical properties of Cu_2O nanocrystals can be obtained by UV-vis absorption spectra, as shown by Figure 1.6 .Cubes, {100}-truncated rhombic dodecahedra and rhombic dodecahedra present a small absorption band at 440-450 nm, meanwhile the edge- and corner truncated octahedral at 540 nm [12].

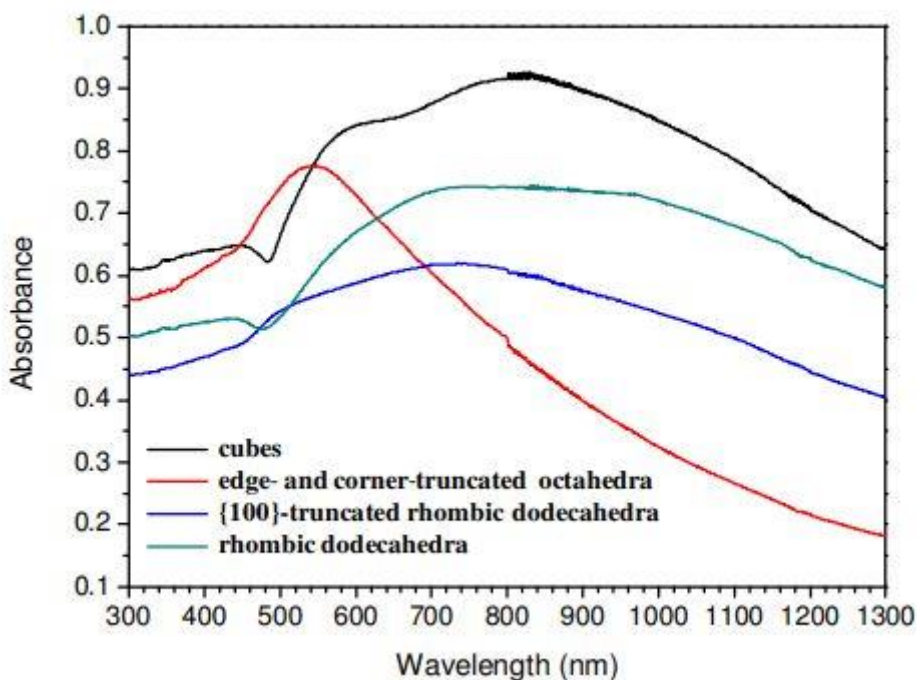


Figure 1.6: UV-vis absorption spectra of Cu_2O nanocrystals. “Reprinted (adapted) with permission from {Wan-Chen Huang, Lian-Ming Lyu, Yu-Chen Yang and Michael H. Huang, *Synthesis of Cu_2O Nanocrystals from Cubic to Rhombic Dodecahedral Structures and Their Comparative Photocatalytic Activity*, J. Am. Chem. Soc. 2012, 134, 1261–1267}. Copyright {2021} American Chemical Society”.

1.4 Rhombic Dodecahedral Cu_2O Synthesis Methods

In the following paragraph, some synthesis methodologies of the rhombic dodecahedral Cu_2O are reported. Zeng et al. [14] present a rhombic dodecahedral Cu_2O synthesis, using copper(II) acetate, hexadecylamine, and undecane under vigorous stirring for 15-90 min at 160-220 °C. An important role is that of hexadecylamine, which could play multiple functions such as a ligand, phase-transfer agent, reducing agent, and surface-regulating agent. Zhang and co-workers [15] propose a method, which involves the use of $\text{Cu}(\text{NO}_3)_2$, CH_2O_2 and NH_3 in an ethanol-water solvent at 145 °C for 90 min. Gao et al. [16] reported the synthesis of rhombic dodecahedral Cu_2O by mixing aqueous CuSO_4 , ethanol, NaOH , $\text{C}_{18}\text{H}_{34}\text{O}_2$ and D-(+)-glucose for 60 min to 100 °C. The only disadvantage of these syntheses is that high temperatures are necessary to carry out the reaction. Another type of synthesis is that of Huang and co-workers [12], which have been able to obtain different crystalline shapes of Cu_2O at room temperature. They have mixed an aqueous solution of CuCl_2 , sodium dodecyl sulfate (SDS) surfactant, NaOH and $\text{NH}_2\text{OH} \cdot \text{HCl}$ reductant. The peculiarity of this last method is that it is possible to synthesize copper (I) oxide with different crystalline morphologies, from cubic to dodecahedral rhombic ones, simply by increasing the amount of reducing agent used. This is reflected in the solution pH, which decreases from 10.70 for the nanocubes to 6.56 for the edge- and corner-truncated octahedra, 6.22 for the all-corner-truncated rhombic dodecahedra, 5.73 for the {100}-truncated rhombic dodecahedra and 5.35 for the rhombic dodecahedra [12]. This information can be an interesting hint to improve new strategies of synthesis of Cu_2O with the desired crystal structure.

1.5 Cu₂O Instability

If Cu₂O possesses good properties as a photo-electrochemical catalyst, it presents the problem to suffer from photo-corrosion and chemical changes. Due to thermodynamically feasible self-reduction and self-oxidation reactions, the shifts of Cu₂O to Cu and CuO are inescapable. These reactions are kinetically and thermodynamically possible because Cu₂O redox potentials are between its conduction and valence band energies. There are works in literature that show how Cu₂O oxidizes into CuO under illumination [17]. For instance, Kakuta and Abe [18] note a deactivation of Cu₂O from self-photooxidation in water reduction and Huang and co-workers [19] reported the transformation of Cu₂O into CuO during photodegradation of methyl orange . On the other hand some studies have presented Cu₂O reduction to Cu in an environment in excess of electrons under photo-irradiation [20][21]. To mitigate the Cu₂O instability, it is possible to realize a co-catalyst, coupling a more stable photo-catalyst to copper (I) oxide. A proper contender is tin (IV) oxide (SnO₂) because of its optical abilities and its charge-collection properties. SnO₂ is used in Perovskite solar cells to enhance considerably their stability, increasing working time, and photovoltaic performances up to 20%, reducing charge recombination [22][23]. For these reasons, tin (IV) oxide is a good co-catalyst to obtain a final catalyst exploiting the Cu₂O good photo-activity and SnO₂ stability under neutral conditions.

1.6 The aim of the thesis

The scope of this work is to investigate copper (I) oxide synthesis methods and their use in the development of Cu-Sn-based photo-electrochemical catalysts for the valorization of carbon dioxide. Initially, the activities are focused on a bibliographic research on the most active crystalline phase of Cu₂O for the photoelectrochemical CO₂ reduction and its synthesis. From literature, it appears that the rhombic dodecahedral Cu₂O is the most photoactive form, while the cubic is the least photoactive. Subsequently, the attention was turned to the synthesis, characterization and testing of Cu₂O-SnO₂ catalysts prepared by two synthesis methods: co-precipitation and precipitation-impregnation two-steps strategy.

For the co-precipitation method, the study has started from a synthesis already implemented by the research team of Prof. Hernández at Politecnico di Torino [24], in which Cu(NO₃)₂ * 3H₂O and SnCl₄ * 5H₂O are used as precursors, Na₂CO₃ is used as a precipitating agent, while NaBH₄ has the function of reducing agent. This synthesis strategy has been modified by applying ultrasounds throughout the reaction time. Moreover, The solution pH was also modified to favor the formation of rhombic dodecahedral Cu₂O and SnO₂ simultaneously.

Starting synthesis for core-shell catalyst is reported by Zhang et al. [6], which synthesize Cu₂O-SnO₂ core-shell nanocubes with the controlled thickness of tin (IV) oxide. This method is subdivided into two steps; the first step is a wet precipitation synthesis to obtain copper(I) oxide nanocubes, using CuCl₂, NaOH and C₆H₈O₆ as reagents; the second one is the formation of a SnO₂ layer by impregnation strategy on Cu₂O, utilizing SnCl₄ *5H₂O. Since nanocubes are the least photo-active crystalline form of copper(I) oxide, the aim is to obtain Cu₂O with a crystal structure similar to rhombic dodecahedral. Initially, it was tried to increase the quantity of Cu₂O synthesized by varying the molarities of precipitant and reducing agents and realize the final catalyst. Since the Cu₂O is cubic, an acid etching process was added in the synthesis to modify the crystalline form and try to obtain a morphology with greater pH

2 Materials and Methods

2.1 Materials and instruments

2.1.1 Materials and instruments for Coprecipitation catalyst synthesis

$\text{Cu}(\text{NO}_3)_2 \cdot 3\text{H}_2\text{O}$ is used as the precursor of copper oxide. $\text{SnCl}_4 \cdot 5\text{H}_2\text{O}$ was used as the precursor of tin oxide. Na_2CO_3 was used as precipitating agent. NaBH_4 was used as the reducing agent. All reagents were procured by Sigma-Aldrich, except $\text{Cu}(\text{NO}_3)_2 \cdot 3\text{H}_2\text{O}$ which was procured from Merck KGaA. A silicone oil bath was needed to maintain the constant temperature of reacting solution. Cellulose nitrate membrane filters with a pore diameter of 5.0 μm were utilized for vacuum filtration and they were purchased from WhatmanTM. MilliQ water was utilized to prepare solutions, during vacuum filtration and to clean glassware and instruments.

The instruments involved during synthesis are listed in the following paragraph. Two peristaltic pumps were used to ensure a constant flow rate of precursors and reducing agent and another one was utilized to keep constant solution pH, varying precipitant agent flow rate. A magnetic plate was utilized to mix and warm up the solution. A sonicator was used during coprecipitation reactions. A vacuum pump, procured by Steroglass, was required for the filtration step. Finally, an oven was used for drying samples.

2.1.2 Materials and instruments for Core-Shell catalyst synthesis

CuCl_2 was used as the copper oxide precursor. NaOH was used as the precipitant agent. L-Ascorbic acid (99%) and Hydroxylamine hydrochloride (98%) were reducing agents for Cu_2O synthesis. $\text{SnCl}_4 \cdot 5\text{H}_2\text{O}$ was used as the tin oxide precursor. Sodium dodecyl sulfate (SDS) was used as a surfactant in the synthesis of copper(I) oxide. Ethanol was the solvent for the deposition of a SnO_2 layer on Cu_2O and for washing Cu_2O samples. HCl was utilized for the acid etching step. NaCl was used to favor ion exchange in the final step. All reagents were purchased from Sigma-Aldrich, except NaOH and NaCl which were procured from CARLO ERBA. Cellulose nitrate membrane filters with a pore diameter of 0.2 μm were utilized for vacuum filtration and they were purchased from WhatmanTM. MilliQ water was utilized to prepare solutions and to clean glassware and instruments.

The instruments involved during synthesis are listed in the following paragraph. Pasteur pipettes used to add reagents to reacting solutions. A magnetic plate was utilized to mix the solution. A vacuum pump, procured by Steroglass, was required for the filtration step. A centrifuge was needed to separate desired compounds. A peristaltic pump was used during acid etching to keep constant solution pH. A drying oven, purchased from Büchi Labortechnik AG, was utilized to dry and obtain final samples. Figure 2.1.2 shows Büchi drying oven and vacuum pump.



Figure 2.1.2: Büchi drying oven and vacuum pump.

2.2 Methods of synthesis

This chapter has the aim to show strategies for the synthesis of Cu-Sn-based catalysts and methodologies to increase the amount of synthesized Cu₂O and try to enhance its nanocrystal shape for obtaining the rhombic dodecahedral one.

2.2.1 Cu₂O-SnO₂ Coprecipitation catalyst synthesis

5.797 g of Cu(NO₃)₂ and 3.355 g of SnCl₄*5H₂O were added in a volume of 40 mL of MilliQ water, to prepare the precursors solution. 0.908 g of NaBH₄ were dissolved in 20 mL of MilliQ water for reducing agent solution, whereas 10.599 g of Na₂CO₃ was used to prepare a precipitant agent solution of 100 mL. 200 mL of MilliQ water was added to a beaker. This was immersed in a silicone oil bath to heat better the solution, placed on a magnetic plate at 70 °C and stirred by an anchor. The precursor solution and the reducing agent solution were added to 200 mL of MilliQ water through constant flow peristaltic pumps and they were set in such a way that in 8 minutes the solutions are completely added to the initial volume of water. On the other hand, the addition of Na₂CO₃ was discontinuous and regulated by a peristaltic pump to keep the reacting solution pH at a constant value. The sonicator was set to an amplitude of 30%. When the required temperature was reached, all the pumps and the sonicator were started and stopped after the reaction time is finished. The next step is aging for 1 h under stirring and at a constant temperature. Subsequently, the solution obtained was filtered and washed through vacuum filtration and the periodic addition of MilliQ water for a total of 1,250 L. Finally, the sample was put in an oven to dry for about 12 h at 60 °C. Figure 2.2.1.1 shows the set-up of coprecipitation synthesis with all instruments. The synthesized samples were named as follows: CP-Cu₂O-SnO₂-pHX-Y, where CP means the coprecipitation method, Cu₂O and SnO₂ are the chemical species, X is the pH value at which the reagent solution is maintained during the synthesis and Y is the number of repetitions of the samples synthesized in the same way.



Figure 2.2.1.1: The set-up of coprecipitation synthesis.

2.2.1.1 Synthesis at pH 7

Initially, it was decided to set the synthesis with a pH of the solution equal to 7. Temperature and pH were monitored during the reaction time, minute by minute, and the aging time every 20 minutes. These values are reported in tables 2.2.1.1.1 and 2.2.1.1.2. Table 2.2.1.1.3 presents quantities of synthesized samples. This synthesis strategy was repeated 5 times to evaluate the replicability of this methodology.

Table 2.2.1.1.1: Temperature and pH of the solution during the reaction time.

Sample	Reaction Time (min)	1	2	3	4	5	6	7	8
CP-Cu ₂ O-SnO ₂ -pH7_1	T (°C)	68	68	68	68	68	68	68	68
	pH	7.4	7	7.1	7	7.2	7	7	7.1
CP-Cu ₂ O-SnO ₂ -pH7_2	T (°C)	69	68	68	68	67	67	67	67
	pH	7	7.2	7.3	7.1	7.4	7.7	7	7.4
CP-Cu ₂ O-SnO ₂ -pH7_3	T (°C)	69	68	68	68	68	68	68	68
	pH	7	7.2	7.4	7	7.5	6.9	7.6	7.3
CP-Cu ₂ O-SnO ₂ -pH7_4	T (°C)	67	67	67	67	68	66	68	68
	pH	7	7.5	7.2	7.2	6.9	7	7	7
CP-Cu ₂ O-SnO ₂ -pH7_5	T (°C)	69	69	70	71	72	72	73	73
	pH	6.8	7.1	7.5	7.4	7.3	7	7.7	7.9

Table 2.2.1.1.2: Temperature and pH of the solution during the aging time.

Sample	Aging Time (min)	20	40	60
CP-Cu ₂ O-SnO ₂ -pH7_1	T (°C)	68	68	68
	pH	7.7	7.9	8.1
CP-Cu ₂ O-SnO ₂ -pH7_2	T (°C)	70	69	70
	pH	7.4	7.7	7.9
CP-Cu ₂ O-SnO ₂ -pH7_3	T (°C)	70	68	70
	pH	7.7	8	8.1
CP-Cu ₂ O-SnO ₂ -pH7_4	T (°C)	63	65	65
	pH	7.7	7.9	8
CP-Cu ₂ O-SnO ₂ -pH7_5	T (°C)	70	69	70
	pH	7.4	7.7	7.9

Table 2.2.1.1.3. The amount of synthesized sample

Sample	Amount (g)
CP-Cu ₂ O-SnO ₂ -pH7_1	3.9082
CP-Cu ₂ O-SnO ₂ -pH7_2	3.8565
CP-Cu ₂ O-SnO ₂ -pH7_3	3.7887
CP-Cu ₂ O-SnO ₂ -pH7_4	3.8675
CP-Cu ₂ O-SnO ₂ -pH7_5	3.9651

2.2.1.2 Synthesis at acid pH

The subsequent step was to set the pH to acidic values, in particular CP-Cu₂O-SnO₂-pH6 to pH 6 and CP-Cu₂O-SnO₂-pH5.5 to pH 5.5. It was decided to carry out the synthesis at acidic pH as, from the literature, the rhombic dodecahedral crystal structure was obtained with a pH of about 5.35 [12]. Temperature and pH were monitored during the reaction time, minute by minute, and the aging time every 20 minutes. These values are reported in tables 2.2.1.2.1 and 2.2.1.2.2. Table 2.2.1.2.3 presents quantities of synthesized samples.

Table 2.2.1.2.1: Temperature and pH of the solution during the reaction time.

Sample	Reaction Time (min)	1	2	3	4	5	6	7	8
CP-Cu ₂ O-SnO ₂ -pH6	T (°C)	67	67	67	67	67	67	67	67
	pH	6.0	6.1	6.1	6	6	6.2	6.1	6
CP-Cu ₂ O-SnO ₂ -pH5.5	T (°C)	75	75	74	74	73	73	72	72
	pH	6.2	5.3	5.6	5.9	5.6	5.5	5.9	5.4

Table 2.2.1.2.2: Temperature and pH of the solution during the aging time.

Sample	Aging Time (min)	20	40	60
CP-Cu ₂ O-SnO ₂ -pH6	T (°C)	66	66	70
	pH	6.6	6.9	7
CP-Cu ₂ O-SnO ₂ -pH5.5	T (°C)	68	69	70
	pH	5.6	5.7	5.9

Table 2.2.1.2.3. The amount of synthesized samples

Sample	Amount (g)
CP-Cu ₂ O-SnO ₂ -pH6	3.6661
CP-Cu ₂ O-SnO ₂ -pH5.5	3.8336

2.2.1.3 Synthesis at basic pH

It was decided to synthesize the catalyst by setting the pH to a basic value to have information also in this pH range. CP-Cu₂O-SnO₂-pH8 was synthesized at pH 8, while CP-Cu₂O-SnO₂-pH9.5 was synthesized at pH 9.5. Temperature and pH were monitored during the reaction time, minute by minute, and the aging time every 20 minutes. These values are reported in tables 2.2.1.3.1 and 2.2.1.3.2. Table 2.2.1.3.3 presents quantities of synthesized samples.

Table 2.2.1.3.1: Temperature and pH of the solution during the reaction time.

Sample	Reaction Time (min)	1	2	3	4	5	6	7	8
CP-Cu ₂ O-SnO ₂ -pH8	T (°C)	69	69	69	69	69	70	70	70
	pH	8.1	7.9	8.2	8	8	8	7.8	7.9
CP-Cu ₂ O-SnO ₂ -pH9.5	T (°C)	71	70	69	69	68	68	67	67
	pH	9.1	9.6	9.5	9.5	9.3	9.5	9.5	9.5

Table 2.2.1.3.2: Temperature and pH of the solution during the aging time.

Sample	Aging Time (min)	20	40	60
CP-Cu ₂ O-SnO ₂ -pH8	T (°C)	70	70	70
	pH	8.1	8.4	8.5
CP-Cu ₂ O-SnO ₂ -pH9.5	T (°C)	68	69	70
	pH	9.4	9.4	9.6

Table 2.2.1.3.3. The amount of synthesized sample

Sample	Amount (g)
CP-Cu ₂ O-SnO ₂ -pH8	3.7061
CP-Cu ₂ O-SnO ₂ -pH9.5	3.4972

2.2.1.4 Synthesis of Cu₂O by the Coprecipitation method without Sn precursor

In this paragraph it tried to synthesize copper (I) oxide, following the methodology developed for the synthesis by co-precipitation, but removing the tin precursor. The same reagents were used, but the molarities were changed. the synthesized samples were named as follows: CP-Cu₂O-pH7-x-y-z, where CP means the synthesis methodology similar to the coprecipitation strategy without Sn precursor, Cu₂O is the chemical species, pH7 means the pH at which the reagent solution is maintained, x the molarity of Cu(NO₃)₂, y is the molarity of N₂CO₃ and z is the molarity of NaBH₄. In the sample CP-Cu₂O-pH7-0.6-1-1.2 the molarities of all the reagents remained unchanged, in the sample CP-Cu₂O-pH7-0.6-1-0.6 the molarity of the NaBH₄ was halved, while in the sample CP-Cu₂O-pH7-0.6-1-0.3 the molarity of NaBH₄ was reduced by four times. Temperature and pH were monitored during the reaction time, minute by minute, and the aging time every 20 minutes. These values are reported in tables 2.2.1.4.1 and 2.2.1.4.2. Table 2.2.1.4.3 presents quantities of synthesized samples.

Table 2.2.1.4.1: Temperature and pH of the solution during the reaction time.

Sample	Reaction Time (min)	1	2	3	4	5	6	7	8
CP-Cu ₂ O-pH7-0.6-1-1.2	T (°C)	67	66	65	65	66	67	68	68
	pH	10.8	10.7	10.6	10.4	10.3	10	9.9	9.9
CP-Cu ₂ O-pH7-0.6-1-0.6	T (°C)	68	68	68	68	68	68	68	68
	pH	9	7	7.8	7.3	7.3	7.5	7.6	7.4
CP-Cu ₂ O-pH7-0.6-1-0.3	T (°C)	69	67	66	66	65	65	65	59
	pH	7.2	6.9	6.9	6.9	76.9	7	7.3	7.4

Table 2.2.1.4.2: Temperature and pH of the solution during the aging time.

Sample	Aging Time (min)	20	40	60
CP-Cu ₂ O-pH7-0.6-1-1.2	T (°C)	70	72	75
	pH	9.7	9.7	9.6
CP-Cu ₂ O-pH7-0.6-1-0.6	T (°C)	69	66	66
	pH	7.4	7.7	8
CP-Cu ₂ O-pH7-0.6-1-0.3	T (°C)	67	69	69
	pH	7.5	7.8	8

Table 2.2.1.4.3. The amount of synthesized sample

Sample	Amount (g)
CP-Cu ₂ O-pH7-0.6-1-1.2	1.4289
CP-Cu ₂ O-pH7-0.6-1-0.6	1.7149
CP-Cu ₂ O-pH7-0.6-1-0.3	2.1064

2.2.2 Cu₂O-SnO₂ Core-Shell catalyst synthesis

The purpose is to create a Cu₂O-SnO₂ core-shell catalyst with dodecahedral rhombic copper(I) oxide. The reference synthesis method is the methodology developed by Zhang et al. [6], in which Cu₂O nanocubes covered with a layer of SnO₂ are made. It is therefore decided to start with this method and try to modify it to increase the amount of synthesized samples and try to obtain the desired crystalline form of Cu₂O.

This synthesis is divided into two steps: the first step is a wet precipitation synthesis to obtain Cu₂O cubic nanocrystals; the second one is the formation of SnO₂ by coordinating etching strategy. All passages are always executed at ambient temperature and below strong stirring.

Cu₂O nanocubes were synthesized by adding gradually a solution of NaOH (2 M, 25 mL) into a solution of CuCl₂ (0.01 M, 250 mL). After 30 minutes, a solution of Ascorbic acid (0.6 M, 25 mL) was added dropwise and subsequently aged 180 minutes. At the end of aging, the solution was filtrated by vacuum filtration and washed with MilliQ water. Finally, the sample was put in a drying oven to dry for about 12 h at 60 °C.

For the second step, 150 mg of Cu₂O, previously synthesized, were dissolved into the solution of 150 mL of ethanol and 4.5 mL of 0.2 M NaCl solution. Then, 0.005 g of SnCl₄*5H₂O are dispersed into 50 mL of ethanol and added to the solution. The quantity of SnCl₄*5H₂O used was in a 1:40 ratio with Cu₂O. The solution was stirred for 10 minutes and put in a centrifuge to recover the catalyst. Finally, the sample was put in a drying oven to dry for about 12 h at 60 °C.

2.2.2.1 Synthesis of Cu₂O with C₆H₈O₆ as reducing agent

A first attempt was made to synthesize copper oxide by varying the concentrations and volumes of the reagents to increase the mass of obtained Cu₂O. The samples obtained were named as follows: P1-Cu₂O-x-y-z-w, where P1 means the precipitation method presented by Zhang et al. [6], Cu₂O is the chemical species, x is the molarity of CuCl₂, y is the molarity of NaOH, z is the molarity of C₆H₈O₆ and w is the total volume of the reagent solution. In particular, in P1-Cu₂O-0.01-2-0.6-300 nothing has changed. In P1-Cu₂O-0.01-3-0.6-300 the molarity of the precipitating agent was increased by 50%. P1-Cu₂O-0.01-2-0.9-300 shows a 50% increase in the molarity of the reducing agent. On the other hand, in P1-Cu₂O-0.01-3-0.9-300 both the precipitating and reducing agents increased by 50%. These samples were synthesized with volumes of the solutions equal to those of the starting synthesis. Instead, P1-Cu₂O-0.01-3-0.9-600 and P1-Cu₂O-0.02-6-1.8-600 were synthesized with doubled volumes. However, P1-Cu₂O-0.01-3-0.9-600 has the same molarities as P1-Cu₂O-0.01-3-0.9-300, while P1-Cu₂O-0.02-6-1.8-600 has double molarities compared to P1-Cu₂O-0.01-3-0.9-300. Table 2.2.2.1.1 shows the molarities and volumes of the solutions used for the syntheses mentioned above. The amounts of copper precursor and that of Cu₂O, obtained from each synthesis, are reported in Table 2.2.2.1.2.

Table 2.2.2.1.1: Molarities and volumes of Cu₂O synthesis.

Sample	Molarity and Volume	CuCl ₂	NaOH	C ₆ H ₈ O ₆
P1-Cu ₂ O-0.01-2-0.6-300	M	0.01	2	0.6
	mL	250	25	25
P1-Cu ₂ O-0.01-3-0.6-300	M	0.01	3	0.6
	mL	250	25	25
P1-Cu ₂ O-0.01-2-0.9-300	M	0.01	2	0.9
	mL	250	25	25
P1-Cu ₂ O-0.01-3-0.9-300	M	0.01	3	0.9
	mL	250	25	25
P1-Cu ₂ O-0.01-3-0.9-600	M	0.01	3	0.9
	mL	500	50	50
P1-Cu ₂ O-0.02-6-1.8-600	M	0.02	6	1.8
	mL	500	50	50

Table 2.2.2.1.2: Amounts of CuCl₂ and Cu₂O

Sample	CuCl ₂ (g)	Cu ₂ O (g)
P1-Cu ₂ O-0.01-2-0.6-300	0.3361	0.1542
P1-Cu ₂ O-0.01-3-0.6-300	0.3361	0.15
P1-Cu ₂ O-0.01-2-0.9-300	0.3361	0.172
P1-Cu ₂ O-0.01-3-0.9-300	0.3361	0.175
P1-Cu ₂ O-0.01-3-0.9-600	0.6722	0.35
P1-Cu ₂ O-0.02-6-1.8-600	1.3345	0.705

2.2.2.2 Synthesis of Cu₂O with C₆H₈O₆ and Acid Etching Step

In the syntheses mentioned in the previous paragraph, the crystalline structure of copper oxide is the cubic one, the least photoactive. From the methodology presented by Huang et al. [6], the most photoactive crystalline forms are those synthesized at acid pH, specifically 6.56 for All-corner-truncated rhombic dodecahedra, 5.73 for {100}-truncated rhombic dodecahedra and 5.35 for Rhombic dodecahedra. Furthermore, a study, conducted by Kuo and Huang, shows how to obtain Cu₂O nanoframes and nanocages through acid etching with an HCl solution [25].

Acid etching is possible thanks to the interaction of the HCl molecules with the surficial ones of Cu₂O, thus modifying the crystalline structure. The mechanism, underlying this procedure, is characterized by the following chemical reaction:



Therefore, it was decided to add another step, acid etching, to the synthesis of Cu₂O, already presented in the previous chapter.

An HCl solution (1 M, 100 mL) was added to the reagent solution through the peristaltic pump for pH control. The pump has been set in such a way as to maintain the pH of the solution at a value of 5.5. Agitation of the reagent solution was also present during the etching step. The synthesized samples were named as follows: P1-Cu₂O-x-y-z-w-EtK, where P1 means the precipitation method presented by Zhang et al. [6], Cu₂O is the chemical species, x is the molarity of CuCl₂, y is the molarity of NaOH, z is the molarity of C₆H₈O₆ and w is the total volume of the reagent solution, Et means the additional acid etching step and K stands for simultaneously with the aging step when it is equal to 0 or it is equal to 3 when acid etching is carried out after aging step. In P1-Cu₂O-0.02-6-1.8-300-Et0 the acid etching was carried out simultaneously with the aging step, which in this case lasted 2 hours instead of 3 hours. On the other hand, in the case of Cu₂O-0.02-6-1.8-300-Et3, the etching step was carried out after the 3 hours of aging step and the reagent solution was kept at pH 5.5 for 25 minutes. Table 2.2.2.2.1 shows the molarities and volumes of the solutions used for the syntheses mentioned above. The amount of copper precursor and that of Cu₂O, obtained from each synthesis with acid etching, are reported in Table 2.2.2.2.2.

Table 2.2.2.2.1: Molarities and volumes of Cu₂O synthesis with acid etching.

Sample	Molarity and Volume	CuCl ₂	NaOH	C ₆ H ₈ O ₆	HCl
P1-Cu ₂ O-0.02-6-1.8-300-Et0	M	0.02	6	1.8	1
	mL	250	25	25	100
P1-Cu ₂ O-0.02-6-1.8-300-Et3	M	0.02	6	1.8	1
	mL	250	25	25	100

Table 2.2.2.2.2: Amounts of CuCl₂ and Cu₂O

Sample	CuCl ₂ (g)	Cu ₂ O (g)
P1-Cu ₂ O-0.02-6-1.8-300-Et0	0.6722	0.165
P1-Cu ₂ O-0.02-6-1.8-300-Et3	0.6722	0.138

2.2.2.3 Synthesis of Cu₂O with SDS and NH₂OH*HCl as reducing agent

The type of synthesis, which will be shown, was developed by Huang et al. [12]. In this method, sodium dodecyl sulfate (SDS) is used as a surfactant and hydroxylamine hydrochloride (NH₂OH*HCl) as a reducing agent. In addition to ensure uniformity of particle size, SDS plays an important role as it improves photocatalytic activity. Copper (I) oxide can expose O-terminated surfaces and Cu-terminated surfaces. O-terminated surfaces are energetically more favorable than Cu-terminated surfaces, as shown by the study conducted by Soon et al. [26]. However, thanks to the absorption of the SDS, Cu-terminated surfaces are energetically more favored, as the [CH₃(CH₂)₁₁SO₄]⁻ groups of the SDS can form an O-Cu bond on the surface Cu atoms and lower the surface energy of the Cu-terminated surfaces, stabilizing it. This increases the photoactivity of Cu₂O because Cu atoms have higher photocatalytic reactivity than O atoms [27]. It was decided to increase the volumes of the solutions by 50 times and to double the molarities to try to obtain a sufficiently large quantity of samples to be characterized and tested.

0.67225 g of CuCl₂ are added in a volume of 25 mL of MilliQ water, which is the precursor solution. 1.66776 g of NH₂OH*HCl are dissolved in 120 mL of MilliQ water for reducing agent solution, whereas 0.71995 g of NaOH are used to prepare a precipitant agent solution of 9 mL. 346 mL of MilliQ water was added to a beaker. This was immersed in a silicone oil bath to heat better the solution, placed on a magnetic plate at 35 °C and stirred by an anchor. The precursor solution and 8,7 g of SDS was added to the 346 mL of MilliQ water. When SDS was completely dissolved, NaOH solution was added to the reactive solution and, subsequently, also NH₂OH*HCl solution was added. The solution is kept under stirring for 1 h for the growth of the crystals. After the aging step, the solution was centrifuged and the precipitate was washed with a 300 mL solution of water and ethanol in a 1: 1 ratio. Washing and centrifugation were performed two times with the same ethanol-water solution to remove unreacted reagents and SDS. A further and final washing was done with only ethanol. Finally, Cu₂O was dispersed in 15 mL of ethanol for storage to avoid possible reactions with atmospheric O₂. Before being analyzed, the sample was dried in a vacuum drying oven at 60° C for 12 h. Table 2.2.2.3.1 shows the amount, molarities and volumes of the solutions used for the syntheses mentioned above. The amount of copper precursor and that of Cu₂O, obtained from each synthesis, are reported in Table 2.2.2.3.2.

Table 2.2.2.3.1: Amounts, molarities and volumes of the solutions.

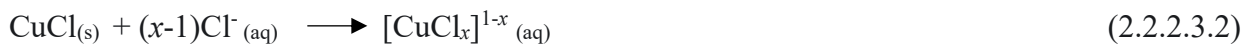
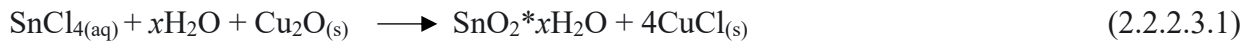
Reagent list	mL	M	g
H ₂ O	346		
CuCl ₂	25	0.2	0.6722
SDS			8.7
NaOH	9	2	0.7199
NH ₂ OH*HCl	120	0.2	1.6678

Table 2.2.2.2.2: Amounts of CuCl₂ and Cu₂O

Sample	CuCl ₂ (g)	Cu ₂ O (g)
P2-Cu ₂ O_1	0.6722	0.157
P2-Cu ₂ O_2	0.6722	0.179

2.2.2.4 Synthesis of Cu₂O-SnO₂ Core-Shell catalyst

After having synthesized the copper (I) oxide, it was decided to proceed with the second step of the core-shell synthesis, the fabrication of the SnO₂ layer through a coordination etching strategy [28]. The possible mechanism, underlying coordination etching for the formation of tin (IV) oxide, can be described by the following chemical reactions:



Copper (I) oxide acts as a template to create hollow SnO₂ structures. Exploiting this, it is possible to obtain this core-shell structure by using a quantity of tin precursor in such a way as not to completely consume the copper oxide core.

The synthesized samples were named as follows: P1+I-Cu₂O-SnO₂-X, where P1+I means the steps presented by zhang et al. [6] to synthesize the final catalyst, Cu₂O and SnO₂ are the chemical species and X are the repeats made of that sample.

P1+I- Cu₂O-SnO₂_1 was synthesized using P1-Cu₂O-0.01-3-0.9-300, samples P1+I- Cu₂O-SnO₂_2 using P1-Cu₂O-0.01-3-0.9-600, while P1+I- Cu₂O-SnO₂_3 and P1+I- Cu₂O-SnO₂_4 using P1- Cu₂O-0.02-6-1.8-600 respectively. The difference between these syntheses is the fact that in sample P1+I- Cu₂O-SnO₂_1 the Cu₂O was dissolved in a solution formed by 150 mL of ethanol and 4.5 mL of 0.2 M NaCl solution, as per the article, while for samples P1+I- Cu₂O-SnO₂_2, P1+I- Cu₂O-SnO₂_3 and P1+I- Cu₂O-SnO₂_4 it was decided to maintain the same volumes of NaCl- ethanol solution to avoid excessive consumption of ethanol. Table 2.2.2.4.1 shows the amounts of all reagents, used in the second step of the core-shell synthesis. Amounts of Cu₂O-SnO₂ core-shell catalyst, obtained from each synthesis, are reported in Table 2.2.2.4.2.

Table 2.2.2.4.1: Reagents for the last step of the core-shell synthesis.

Sample	P1+I- Cu ₂ O-SnO ₂ _1	P1+I- Cu ₂ O-SnO ₂ _2	P1+I- Cu ₂ O-SnO ₂ _3	P1+I- Cu ₂ O-SnO ₂ _4
Cu ₂ O	0.15 g	0.35 g	0.35 g	0.35 g
EtOH	150 mL	150 mL	150 mL	150 mL
NaCl	4.5 mL (0.2 M)			
SnCl ₄ *5H ₂ O	0.005 g	0.012 g	0.012 g	0.012 g
EtOH	50 mL	50 mL	50 mL	50 mL

Table 2.2.2.4.2: Amounts of Cu₂O-SnO₂ core-shell catalysts

Sample	Amount (g)
P1+I-Cu ₂ O-SnO ₂ _1	0.116
P1+I-Cu ₂ O-SnO ₂ _2	0.28
P1+I-Cu ₂ O-SnO ₂ _3	0.305
P1+I-Cu ₂ O-SnO ₂ _4	0.28

3 Characterization

In the following chapter all the characterizations of the synthesized samples will be presented. Specifically, the characterizations include XRD, BET, UV-visible absorption spectroscopy, EDX and FE-SEM.

X-ray diffraction (XRD) [27] is a technique that aims to identify the crystalline phase and estimate the size of the particles. The principle behind this analysis is the scattering of x-ray photons from atoms in a crystal lattice. During the analysis, an x-ray beam, with a wavelength varying between 0.5 and 2 Å, is sent on the sample and, subsequently, is diffracted by a certain θ angle. This phenomenon is described by Bragg's law (Eq. 3.1), where $n = 1.2 \dots d$ is the space between the atomic planes in a crystal structure and θ is the diffraction angle. The intensity of the diffracted x-rays is plotted as a function of double the θ angle. Therefore, the position of the peaks and their intensity, expressed in percentages respect to the highest peak, represents the identification pattern of the analyzed sample. later this pattern is compared with known patterns of metals and oxides of the international center for diffraction data (ICDD). The advantages related to this technique are: sensitivity to the crystalline structure and to the size of the crystals; ease to carry out; possibility to work in situ. Instead, the disadvantages are: not sensitive to amorphous phases; the need for a minimum concentration of 1% w / w; it is not surface sensitive . Figure 3.1 shows the diffraction of x-rays on a crystalline lattice.

$$n \lambda = 2 d \sin \theta \quad (3.1)$$

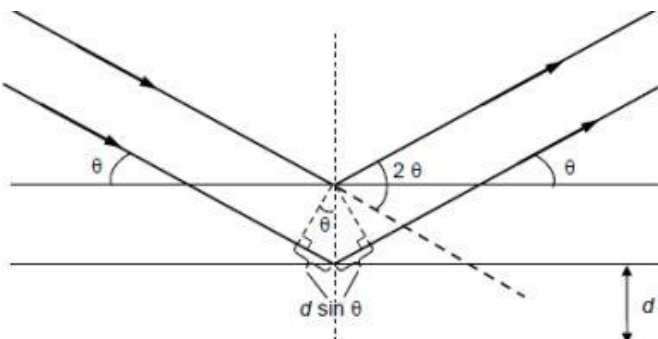


Figure 3.1: The diffraction of x-rays

BET [28]analysis is an analytical method to obtain information related to the surface area of porous materials, the size and volume of their pores. The phenomenon that characterizes this methodology is the adsorption of liquid N₂ at 77 K. The results obtained are isotherms in which the volume of the adsorbed nitrogen molecules is plotted as a function of the normalized pressure. Hysteresis indicates the presence of mesopores and gives information on the shape of the pores. Knowing the area occupied by a nitrogen molecule (16.2Å²) and the number of N₂ molecules adsorbed in the monolayer coverage, it is possible to calculate the specific surface area following Eq. 3.2, where S is the specific surface area (m² / g), n_m is the capacity of the monolayer (mole / g), A_m is the specific area occupied by a molecule (m² / g) and N is the Avogadro number (molecules/mole).

$$S = n_m * A_m * N \quad (3.2)$$

The pore size is estimated based on the quantity of gas condensed in the pores. Several mathematical derivations describe the adsorption isotherms and the formation of the monolayer

on the surface. Among these, the simplest is that of Langmuir, while a more complex model is that of Brunauer – Emmett – Teller (BET), whose acronym is commonly used to indicate this type of analysis.

UV-visible absorption spectroscopy [28] allows to carry out analyzes by studying the electromagnetic radiation absorbed and the intensity of the radiation. The absorbance $F(R)$ is plotted as a function of the wavelength λ (nm). Through the Tau plot method, it is possible to obtain the energy bandgap of the analyzed sample. In this method, on the abscissa axis there is the energy in eV ($E = h\nu$) while on the ordinates there is the absorbance coefficient α ($\alpha = [F(R) * h\nu]^2$). Eq.3.3 shows how to switch from wavelength λ (nm) to energy E (eV), where h is the Planck constant and c is the speed of light.

$$h = 4.1356678 * 10^{-15} \text{ eV} * \text{s}$$

$$c = 299792458 \quad \text{m/s}$$

$$E = h * \nu = h * \frac{c}{\lambda} = \frac{1240}{\lambda} \quad (4.3)$$

Once this is done, a straight line is drawn tangent to the points where the graph assumes a linear trend. Finally, the intersection between this line and the abscissa axis represents the value of the sample energy bandgap.

Scanning electron microscope (SEM) [29] is an analytical technique for studying the surface of materials. Through a highly focused electron beam (primary), it is possible to obtain images of the surface topography of the samples in high resolution. Primary electrons collide with the surface of the material, giving rise to low-energy secondary electrons. The topography is linked to the intensity of these secondary electrons, by relating the intensity with the position of the primary beam in its scanning movement, the image of the surface is generated. Together with the secondary electrons, backscattered electrons and also X-rays are emitted from the interaction between the sample and the primary electron beam. the backscattered electrons are important because their intensity can be correlated with the atomic number of the elements present in the sample, thus giving qualitative information on the elemental composition. This technique is called Energy Dispersive X-ray Analysis (EDX).

3.1 Cu₂O-SnO₂ Coprecipitation Synthesis

In this chapter the characterizations carried out on the sample synthesized by coprecipitation set-up will be shown.

3.1.1 Cu₂O-SnO₂-Coprecipitation Catalyst

In following paragraph the characterizations carried out on the coprecipitation synthesis samples prepared with neutral, acid and basic pH will be shown.

3.1.1.1 XRD

Figure 3.1.1.1.1 presents the XRD spectrum of samples synthesized at pH 7, while Figure 3.1.1.1.2 and Figure 3.1.1.1.3 show XRD spectrum of samples synthesized at acid pH and at basic pH respectively. Table 3.1.1.1.1 shows the reference card to analyze XRD results

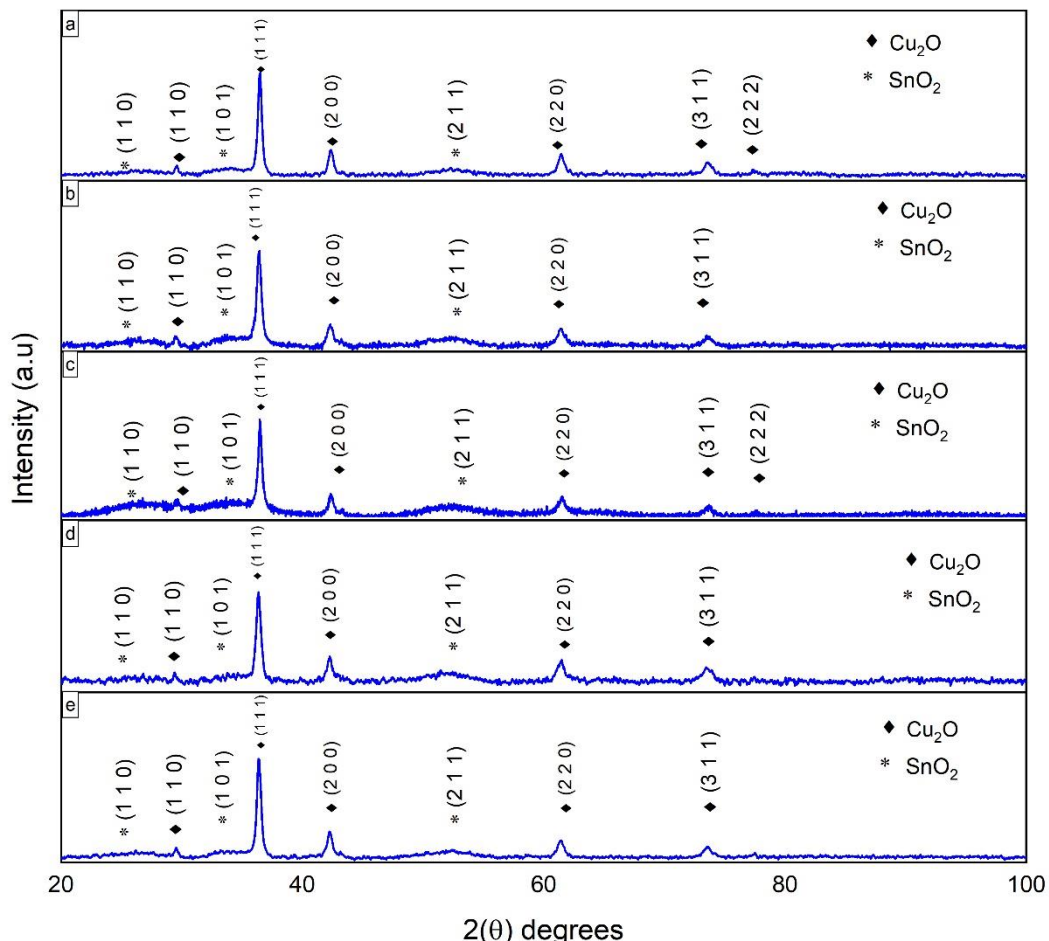


Figure 3.1.1.1.1: XRD spectrum of samples a) CP-Cu₂O-SnO₂-pH7_1, b) CP-Cu₂O-SnO₂-pH7_2, c) CP-Cu₂O-SnO₂-pH7_3, d) CP-Cu₂O-SnO₂-pH7_4 and e) CP-Cu₂O-SnO₂-pH7_5.

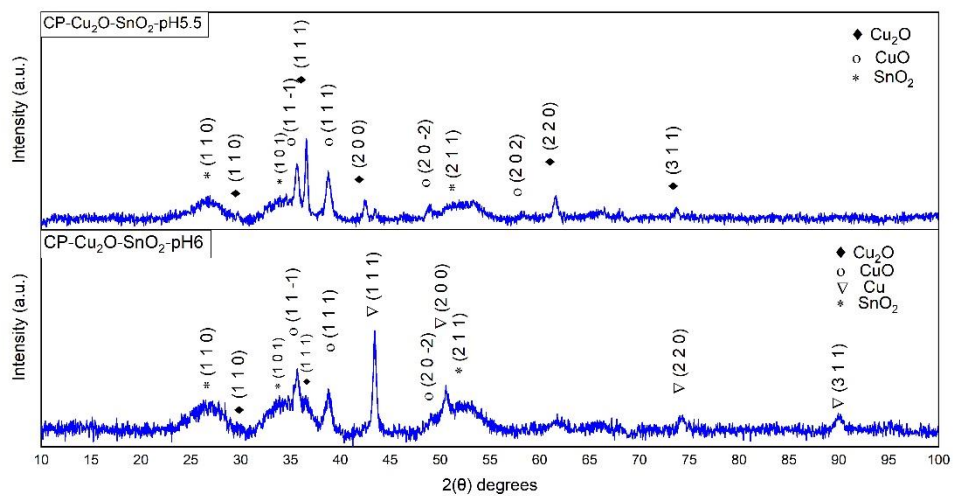


Figure 3.1.1.1.2: XRD spectrum of CP-Cu₂O-SnO₂ samples synthesized at acid pH.

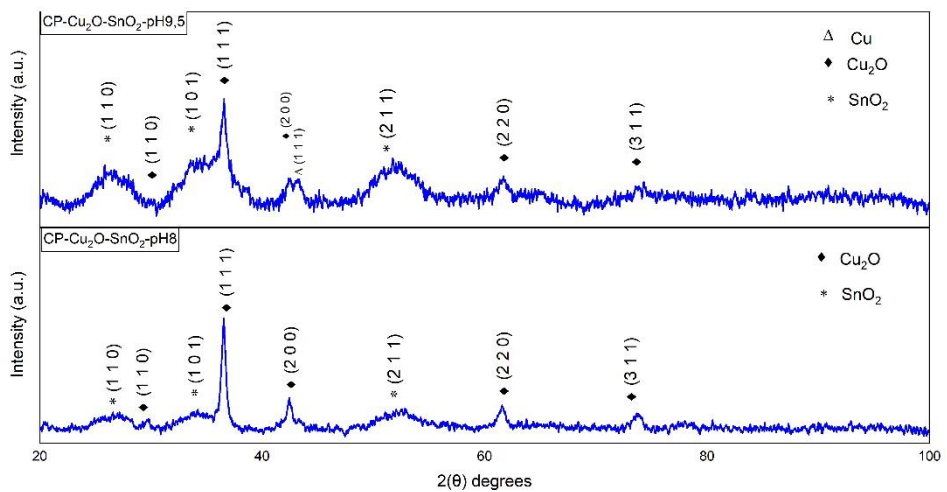


Figure 3.1.1.1.3: XRD spectrum of CP-Cu₂O-SnO₂ samples synthesized at basic pH

Table 3.1.1.1.1 : Reference Cards

	Reference Card
Cu	00 004 0836
CuO	00 048 1548
Cu ₂ O	01 077 0199
SnO ₂	00 041 1445

Crystal sizes are calculated using Debye - Scherrer's law:

$$D = \frac{0.9 * \lambda}{(FWHM) * \cos\theta} \quad (3.1.1.1.1)$$

where D is the size of the crystals, λ (1.540 Å) is the wavelength of the x-ray beam incident on the sample, FWHM is the width of the peak of greatest intensity calculated at half height and θ is half the angle in which this is positioned peak [27]. Crystal size, {220}/{200} peak intensity ratio and {111}/{200} peak intensity ratio of CP-Cu₂O-SnO₂-pH7 samples are reported in Table 3.1.1.1.2, while Table 3.1.1.1.3 shows values of crystal size, {220}/{200} peak intensity ratio and {111}/{200} peak intensity ratio for samples synthesized at acid and basic pH.

Tables 3.1.1.1.2: Crystal size, {220}/{200} peak intensity ratio and {111}/{200} peak intensity ratio of CP-Cu₂O-SnO₂-pH7 samples.

Samples	Cu ₂ O Crystal Size (nm)	{220}/{200} Peak Intensity Ratio	{111}/{200} Peak Intensity Ratio
CP-Cu ₂ O-SnO ₂ -pH7-1	27.5	0.83	4.22
CP-Cu ₂ O-SnO ₂ -pH7-2	37.7	0.81	4.59
CP-Cu ₂ O-SnO ₂ -pH7-3	32.3	0.70	5.16
CP-Cu ₂ O-SnO ₂ -pH7-4	23.9	0.83	3.89
CP-Cu ₂ O-SnO ₂ -pH7-5	42.5	0.68	4.12
Average value	32.76 ± 7.51	0.77 ± 0.07	4.10 ± 0.50

Tables 3.1.1.1.3: Crystal size, {220}/{200} peak intensity ratio and {111}/{200} peak intensity ratio of CP-Cu₂O-SnO₂ samples synthesized at acid and basic pH

Samples	Cu ₂ O Crystal Size (nm)	{220}/{200} Peak Intensity Ratio	{111}/{200} Peak Intensity Ratio
CP-Cu ₂ O-SnO ₂ -pH5.5	57.3	1.60	5.29
CP-Cu ₂ O-SnO ₂ -pH6	39.8		
CP-Cu ₂ O-SnO ₂ -pH8	33.9	0.63	3.59
CP-Cu ₂ O-SnO ₂ -pH9.5	23.9	0.79	3.74

3.1.1.2 BET

Table 3.1.1.2.1 shows the surface area, pore volume and pore size of the synthesized samples at pH 7, while Table 3.1.1.2.2 presents the surface area, pore volume and pore size of the synthesized samples at acid and basic pH.

Table 3.1.1.2.1: BET results of coprecipitation catalysts synthesized at pH 7.

Sample	Surface Area (m ² /g)	Pore Volume (cm ³ /g)	Pore size (Å)
CP-Cu ₂ O-SnO ₂ -pH7_1	125,9	0,084	50,4
CP-Cu ₂ O-SnO ₂ -pH7_2	130,7	0,109	56,6
CP-Cu ₂ O-SnO ₂ -pH7_3	142	0,121	58,5
CP-Cu ₂ O-SnO ₂ -pH7_4	137,6	0,091	53,3
Average value	134 ± 7,15	0,101 ± 0,017	54,7 ± 3,58

Table 3.1.1.2.2: BET results of coprecipitation catalysts synthesized at acid and basic pH.

Sample	Surface Area (m ² /g)	Pore Volume (cm ³ /g)	Pore size (Å)
CP-Cu ₂ O-SnO ₂ -pH5.5	86,5	0,044	42,9
CP-Cu ₂ O-SnO ₂ -pH6	118,5	0,08	50,4
CP-Cu ₂ O-SnO ₂ -pH8	125	0,13	58,4
CP-Cu ₂ O-SnO ₂ -pH9,5	27,8	0,024	66,8

Figure 3.1.1.2.1, Figure 3.1.1.2.2 and Figure 3.1.1.2.3 presents the BET isotherm curves of synthesized samples at pH7, acid pH and basic pH respectively

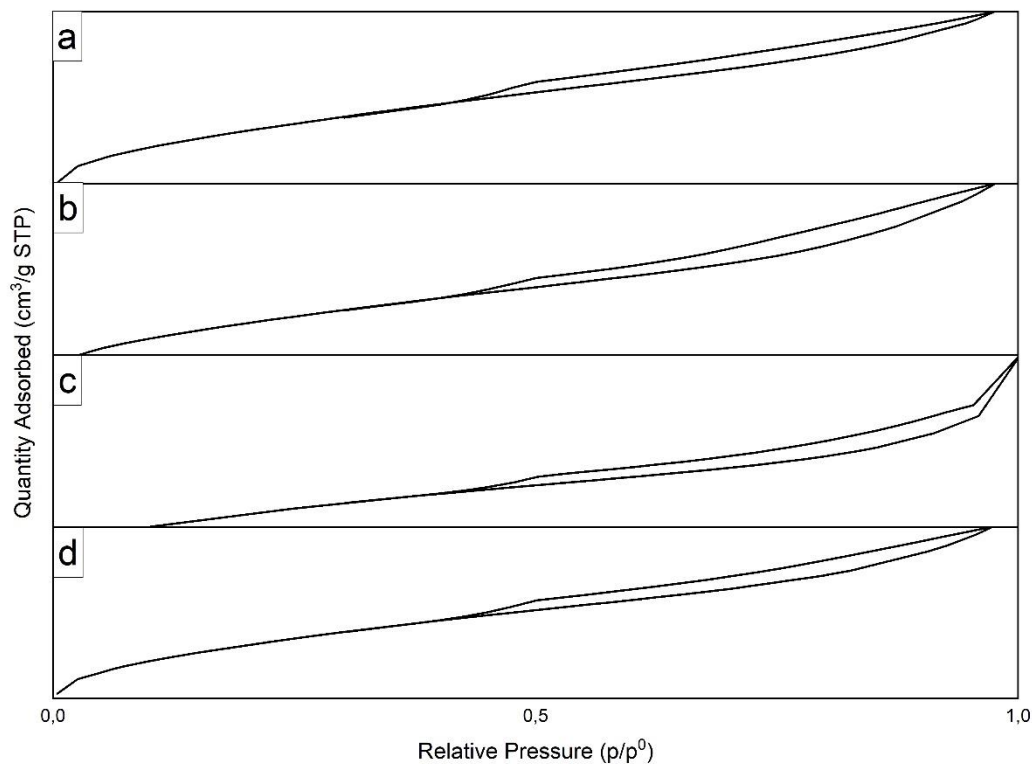


Figure 3.1.1.2.1: BET isotherm curves of samples a) CP-Cu₂O-SnO₂-pH7_1, b) CP-Cu₂O-SnO₂-pH7_2, c) CP-Cu₂O-SnO₂-pH7_3 and d) CP-Cu₂O-SnO₂-pH7_4.

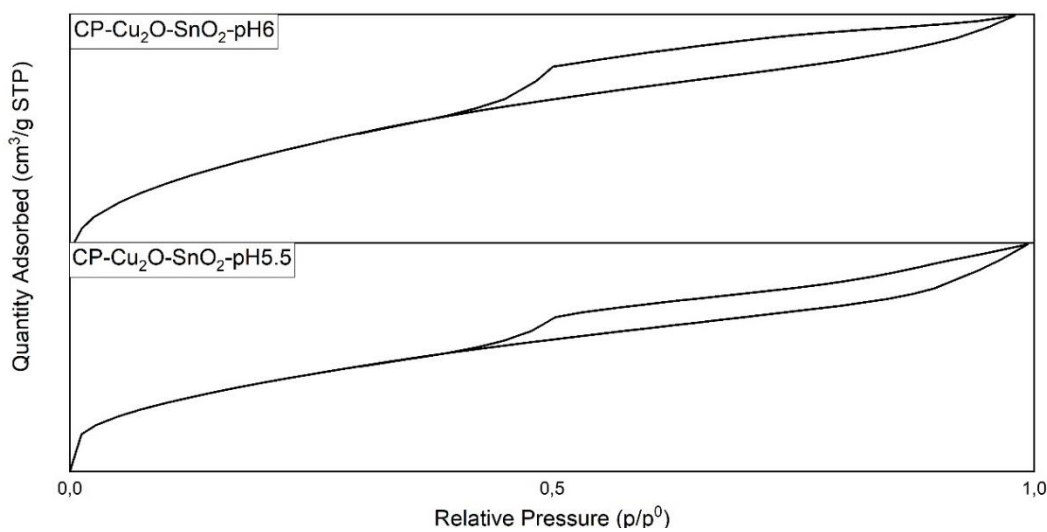


Figure 3.1.1.2.2: BET isotherm curves of CP-Cu₂O-SnO₂ samples synthesized at acid pH.

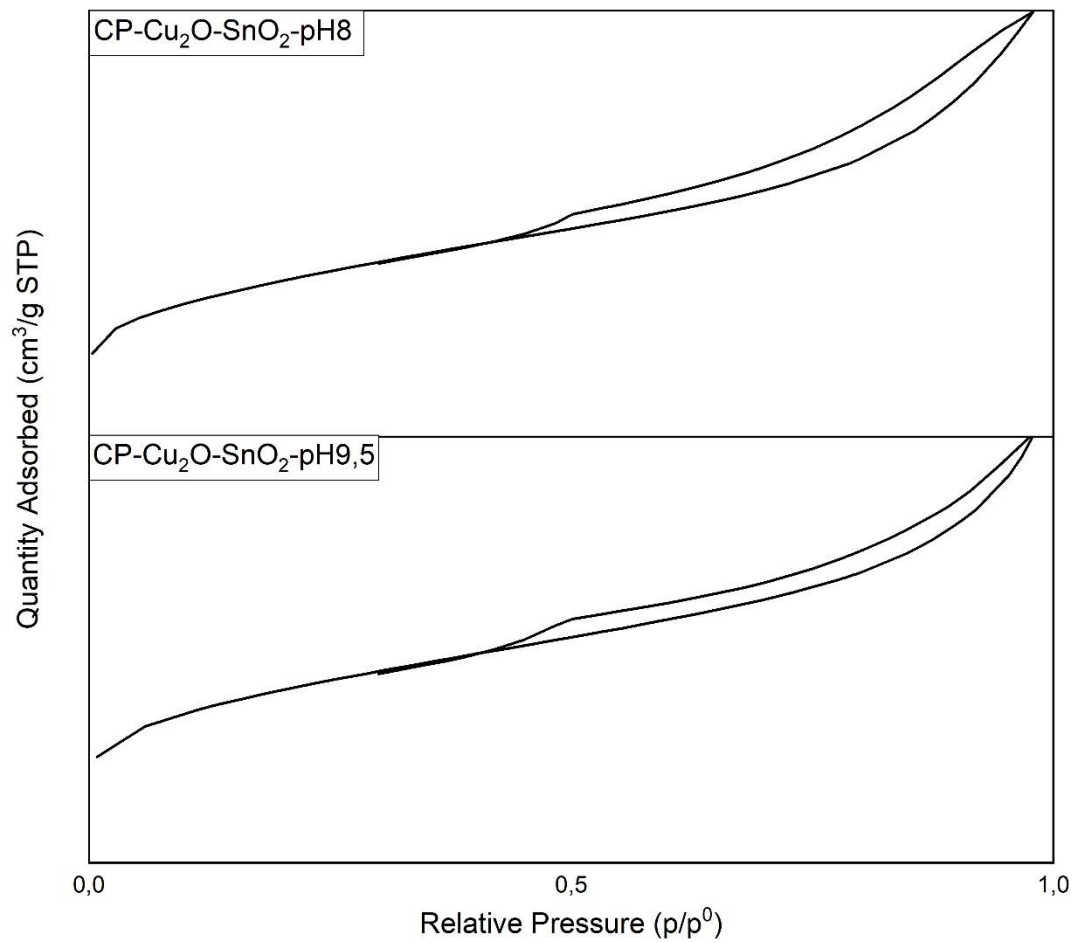


Figure 3.1.1.2.3: BET isotherm curves of CP-Cu₂O-SnO₂ samples synthesized at basic pH

3.1.1.3 UV-visible absorption spectroscopy

Through the Tau plot method, it is possible to evaluate the energy bandgap of samples. Figure 3.1.1.3.1 and Figure 3.1.1.3.2 show the graphs for the Tau plot method, while Table 3.1.1.3.1 and Table 3.1.1.3.2 give the values of the Energy Bandgap (E_g) of samples.

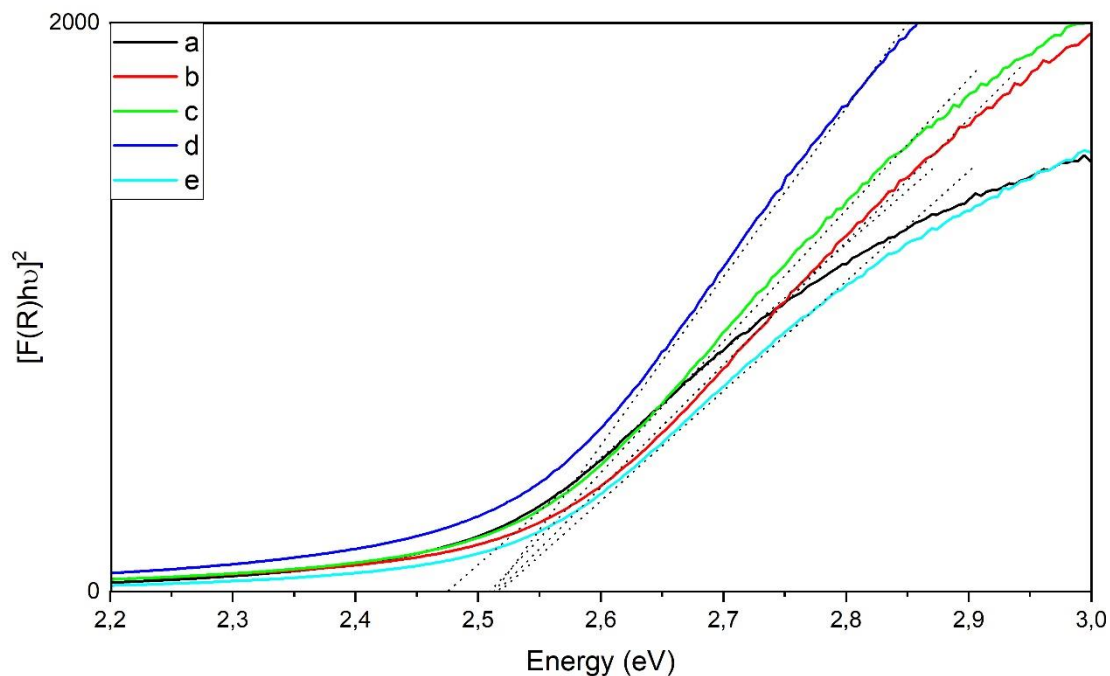


Figure 3.1.1.3.1: UV-visible absorption curves of samples a) CP-Cu₂O-SnO₂-pH7_1, b) CP-Cu₂O-SnO₂-pH7_2, c) CP-Cu₂O-SnO₂-pH7_3, d) CP-Cu₂O-SnO₂-pH7_4 and e) CP-Cu₂O-SnO₂-pH7_5.

Table 3.1.1.3.1: Energy Bandgaps of CP-Cu₂O-SnO₂-pH7 samples.

Sample	E_g (eV)
CP-Cu ₂ O-SnO ₂ -pH7_1	2.48
CP-Cu ₂ O-SnO ₂ -pH7_2	2.52
CP-Cu ₂ O-SnO ₂ -pH7_3	2.52
CP-Cu ₂ O-SnO ₂ -pH7_4	2.52
CP-Cu ₂ O-SnO ₂ -pH7_5	2.52
Average value	2.51 ± 0.02

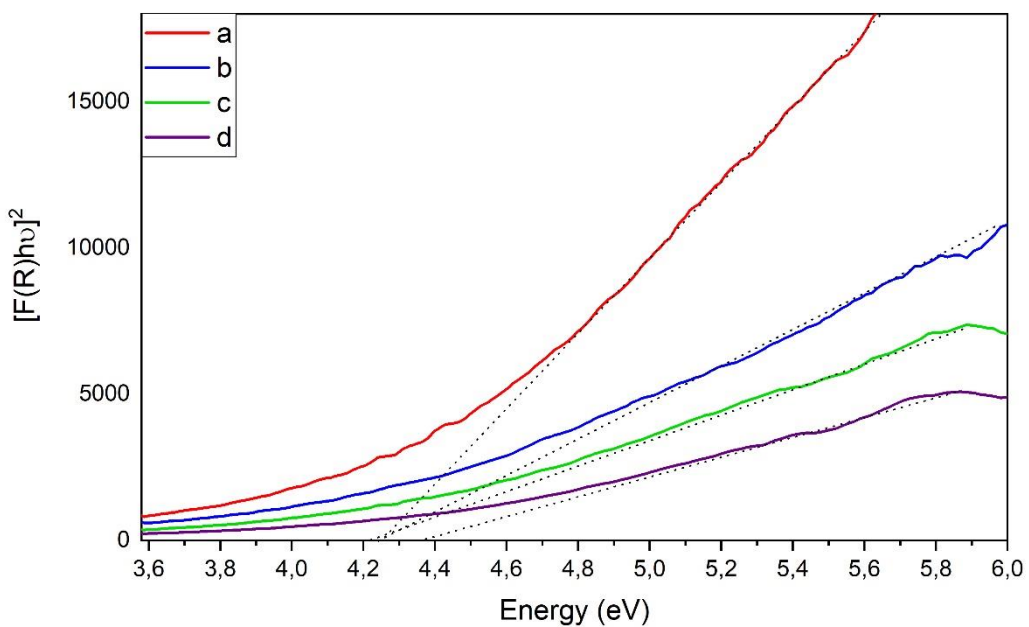


Figure 3.1.1.3.2: UV-visible absorption curves of samples a) CP-Cu₂O-SnO₂-pH8, b) CP-Cu₂O-SnO₂-pH9.5, c) CP-Cu₂O-SnO₂-pH5.5, and d) CP-Cu₂O-SnO₂-pH6.

Table 3.1.1.3.1: Energy Bandgaps of CP-Cu₂O-SnO₂-pH7 samples.

Sample	E _g (eV)
CP-Cu ₂ O-SnO ₂ -pH5.5	4.25
CP-Cu ₂ O-SnO ₂ -pH6	4.4
CP-Cu ₂ O-SnO ₂ -pH8	4.25
CP-Cu ₂ O-SnO ₂ -pH9.5	4.25

3.1.2 Cu₂O synthesized by the Coprecipitation method without Sn . precursor

In following paragraph the characterizations carried out on the synthesis of Cu₂O by the precipitation method without Sn precursor will be shown.

3.1.2.1 XRD

Figure 3.1.2.1.1 presents the XRD spectrum of CP-Cu₂O-pH7 samples and the reference cards, to analyze XRD results, are reported in Table 3.1.1.1.1.

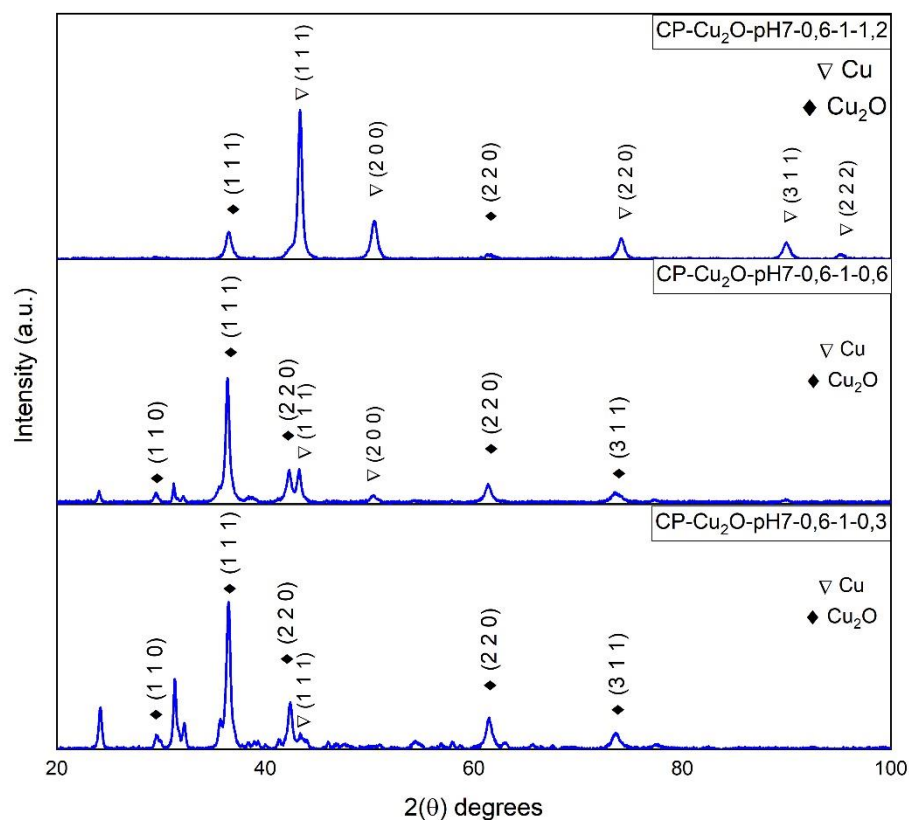


Figure 3.1.2.1.1: XRD spectrum of CP-Cu₂O-pH7 samples.

3.1.2.2 UV-visible absorption spectroscopy

Through the Tau plot method, it is possible to evaluate the energy bandgap of samples. Figure 3.1.2.2.1 shows the graphs for the Tau plot method, while Table 3.1.2.2.1 gives the values of the Energy Bandgap (E_g) of samples.

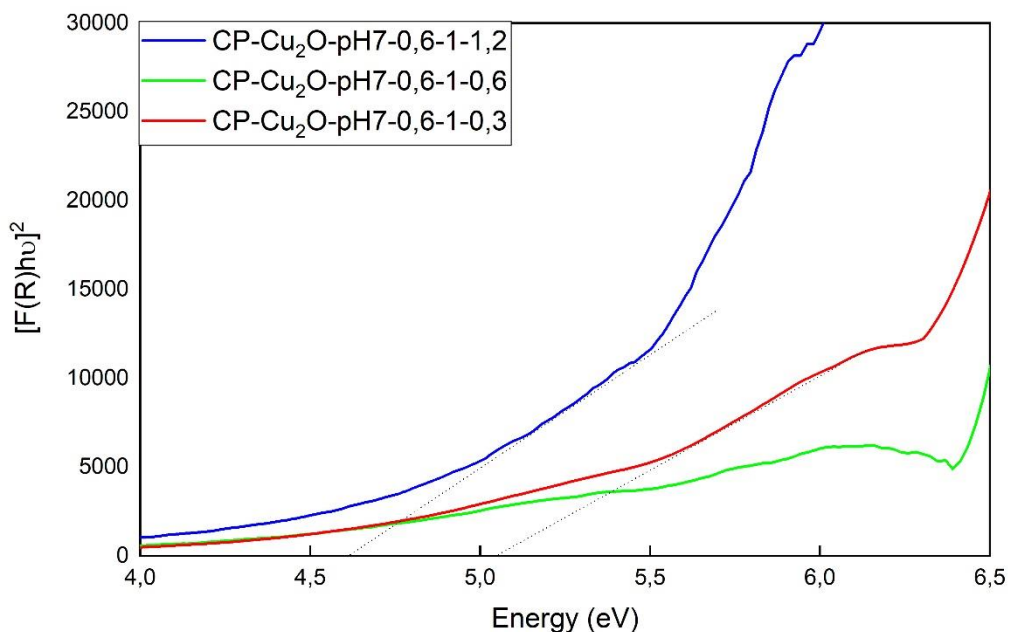


Figure 3.1.2.2.1: UV-visible absorption curves of CP-Cu₂O-pH7 samples

Table 3.1.2.2.1: Energy Bandgaps of CP-Cu₂O-pH7 samples.

Sample	E_g (eV)
CP-Cu ₂ O-pH7-0.6-1-1.2	4.6
CP-Cu ₂ O-pH7-0.6-1-0.3	5.1

3.1.3 Results Discussion

From the analysis of the XRD spectra of the samples synthesized at pH 7, it can be seen that the peaks related to Cu₂O are evident, while those of SnO₂ have a bulging shape, probably due to its amorphous nature. For samples synthesized at pHs different than neutral, CP-Cu₂O-SnO₂-pH8 shows only peaks relative to Cu₂O and SnO₂, while CP-Cu₂O-SnO₂-pH5.5 also has peaks in CuO, CP-Cu₂O-SnO₂-pH6 has peaks of metallic Cu and CuO and CP-Cu₂O-SnO₂-pH9.5 has peaks relative to metallic Cu in addition to those of Cu₂O and SnO₂. Figure 3.1.3.1 compares the Cu₂O Crystal Size, {220}/{200} PIR (Peak Intensity Ratio) and {111}/{200} PIR of CP-Cu₂O-SnO₂ samples synthesized at different solution pH.

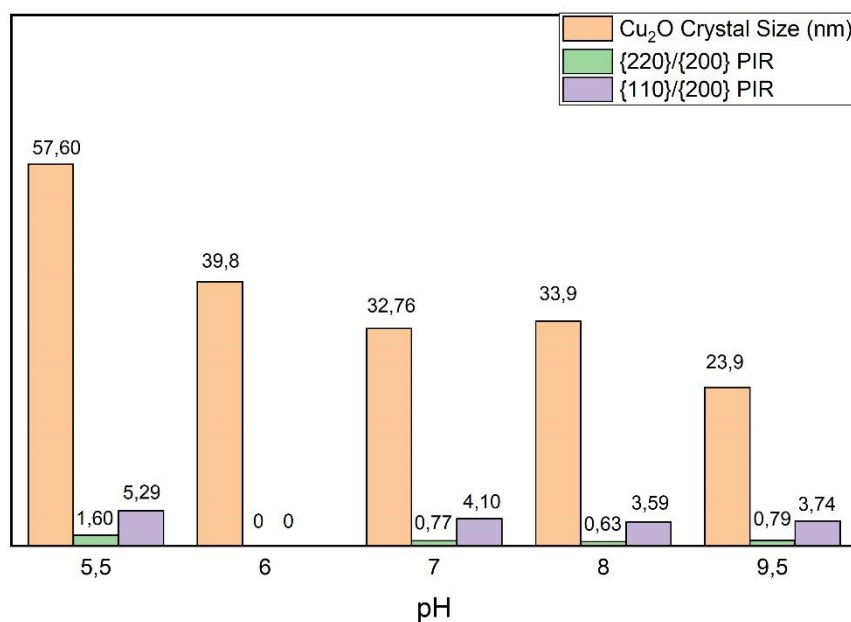


Figure 3.1.3.1: Cu₂O Crystal Size, {220}/{200} PIR (Peak Intensity Ratio) and {111}/{200} PIR of CP-Cu₂O-SnO₂ samples synthesized at different solution pH.

From Figure 3.1.3.1, it can be deduced that the sample synthesized at pH 8 does not present significant differences with that at neutral pH. It can also be noted that the size of the crystals tends to increase moving towards a more acidic pH. However, at acid pH the synthesis reaction is less controlled, given the presence of Cu and CuO and the not negligible variations of the parameters PIR {220} / {200} and PIR {111} / {200}.

As regards the surface area and porosity, the samples at pH 7 have an average surface area of $134 \pm 7,15 \text{ m}^2/\text{g}$, pore volume of $0,101 \pm 0,017 \text{ cm}^3/\text{g}$ and pore size of $54,7 \pm 3,58 \text{ \AA}$. Its surface area is the highest compared to the samples synthesized at pH different from 7, while the lowest of pore size is to be attributed to CP-Cu₂O-SnO₂-pH5.5 with a value of $42,9 \text{ \AA}$ and the highest value of the pore volume is that of CP-Cu₂O-SnO₂-pH8 equal to $0,13 \text{ cm}^3/\text{g}$. From the observation of the hysteresis of the adsorption isotherms, it can be assumed that the pores of all CP-Cu₂O-SnO₂ samples may be cylindrical in shape. Figure 3.1.3.2 compares surface area, pore size and pore volume of CP-Cu₂O-SnO₂ samples synthesized at different pH.

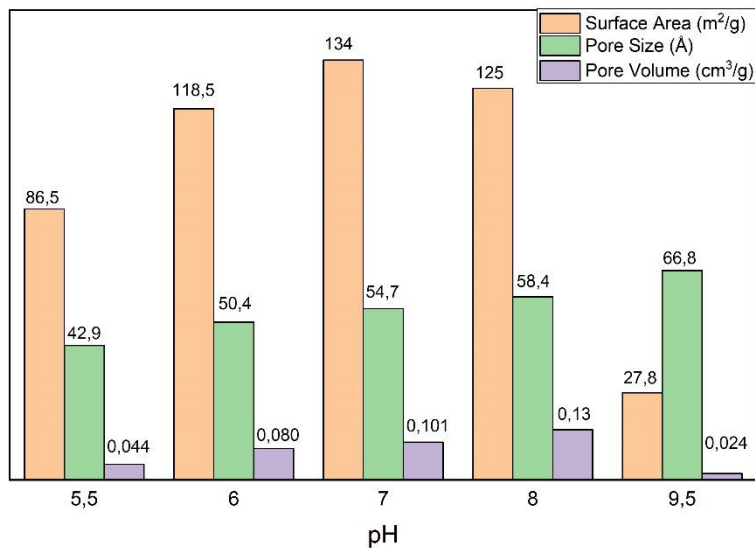


Figure 3.1.3.2: Surface area, pore size and pore volume of CP-Cu₂O-SnO₂ samples synthesized at different solution pH.

From the UV-Visible absorption spectrum and through the Tau plot method, the Energy Bandgap values of the CP-Cu₂O-SnO₂ samples were obtained. CP-Cu₂O-SnO₂-pH7 samples have an energy bandgap of average value $2.51 \text{ eV} \pm 0.02$. This result is reasonable, given that from the literature, the energy bandgap of Cu₂O is approximately 2-2.2 eV [25, 30, 32, 33], while that of SnO₂ oscillates between 3,58 and 3,8 eV [34, 35, 38]. On the other hand, the other samples show an energy band gap value of 4.25 eV, except the CP-Cu₂O-SnO₂-pH6 which has an E_g value equal to 4.4 eV.

In conclusion, from the overall analysis of the collected data, the CP-Cu₂O-SnO₂-pH7s appear to be the samples in which there is exclusively Cu₂O and SnO₂, those with lower energy bandgap and with higher surface area. Consequently, it can be affirm that the optimal pH for the synthesis by co-precipitation of Cu₂O and SnO₂ is 7. For this reason, it was decided not to repeat the syntheses at different pH. As regards the replicability of the CP-Cu₂O-SnO₂-pH7 samples, the energy bandgap shows a percentage variation coefficient of 0.8%, the surface area shows a value of 5% and a pore size of 6.5%. However, higher percentage variation coefficients are relative to Cu₂O crystal size and pore volume with values of 22.9% and 16.8% respectively. therefore the synthesis by coprecipitation at pH 7 shows a good replicability. Table 3.1.3.1 shows the percentage variation coefficients of the repetitions made at pH 7.

Table 3.1.3.1: Percentage variation coefficients of the repetitions made at pH 7.

	Percentage variation coefficients (%)
Energy Bandgap	0,8
Surface area	5
Pore size	6,5
Pore volume	16,8
Cu ₂ O crystal size	22,9
{220}/{200} PIR	9
{111}/{200} PIR	12,2

3.2 Cu₂O-SnO₂ Core-Shell Catalysts

In the following chapter the characterizations related to the copper (I) oxide and the Cu₂O-SnO₂ core-shell samples will be presented.

3.2.1 Cu₂O with C₆H₈O₆ as reducing agent

The analyzed samples refer to the Cu₂O obtained by the wet precipitation method [6], where ascorbic acid acts as a reducing agent.

3.2.1.1 Yield

The paragraph shows the yields of the syntheses in terms of the ratio between amount of copper in the precursor and amount of copper in the Cu₂O obtained. The following formulas are used to calculate the yield:

$$N_{CuCl_2} = \frac{m_{CuCl_2}}{PM_{CuCl_2}} \quad (3.2.1.1.1)$$

$$1 : N_{Cu^{2+}} = 1 : N_{CuCl_2} \quad (3.2.1.1.2)$$

$$N_{Cu^{2+}} = N_{CuCl_2} \quad (3.2.1.1.3)$$

$$m_{Cu^{2+}} = N_{Cu} * PM_{Cu} = N_{CuCl_2} * PM_{Cu} = m_{CuCl_2} * \frac{PM_{Cu}}{PM_{CuCl_2}} \quad (3.2.1.1.4)$$

$$N_{Cu_2O} = \frac{m_{Cu_2O}}{PM_{Cu_2O}} \quad (3.2.1.1.5)$$

$$1:N_{Cu^{+}}=2:N_{Cu_2O} \quad (3.2.1.1.6)$$

$$N_{Cu^{+}} = 2 * N_{Cu_2O} \quad (3.2.1.1.7)$$

$$m_{Cu^{+}} = N_{Cu^{+}} * PM_{Cu} = 2 * N_{Cu_2O} * PM_{Cu} = 2 * m_{Cu_2O} * \frac{PM_{Cu}}{PM_{Cu_2O}} \quad (3.2.1.1.8)$$

$$\eta = \frac{m_{Cu^{+}}}{m_{Cu^{2+}}} * 100 \% \quad (3.2.1.1.9)$$

where N is moles (mol), PM is molecular weight (mol/g), m is the mass (g) and η is the yield percent. Table 3.2.1.1.1 shows the amount of CuCl₂ and Cu₂O obtained and respective yields.

Table 3.2.1.1.1: Yields of P1-Cu₂O samples

Sample	CuCl ₂ (g)	Cu ₂ O (g)	Yield (%)
P1-Cu ₂ O-0.01-2-0.6-300	0.336125	0.1542	86.21
P1-Cu ₂ O-0.01-3-0.6-300	0.336125	0.15	83.86
P1-Cu ₂ O-0.01-2-0.9-300	0.336125	0.172	96.16
P1-Cu ₂ O-0.01-3-0.9-300	0.336125	0.175	97.84
P1-Cu ₂ O-0.01-3-0.9-600	0.67225	0.35	97.84
P1-Cu ₂ O-0.02-6-1.8-600	1.3345	0.705	99.28

3.2.1.2 XRD

Figure 3.2.1.2.1 presents the XRD spectrum of samples and the reference card for analyzing XRD results is 01 077 0199 corresponding to Cu₂O. Table 3.2.1.2.1 shows values of crystl size, {220}/{200} peak intensity ratio and {111}/{200} peak intensity ratio of P1-Cu₂O samples.

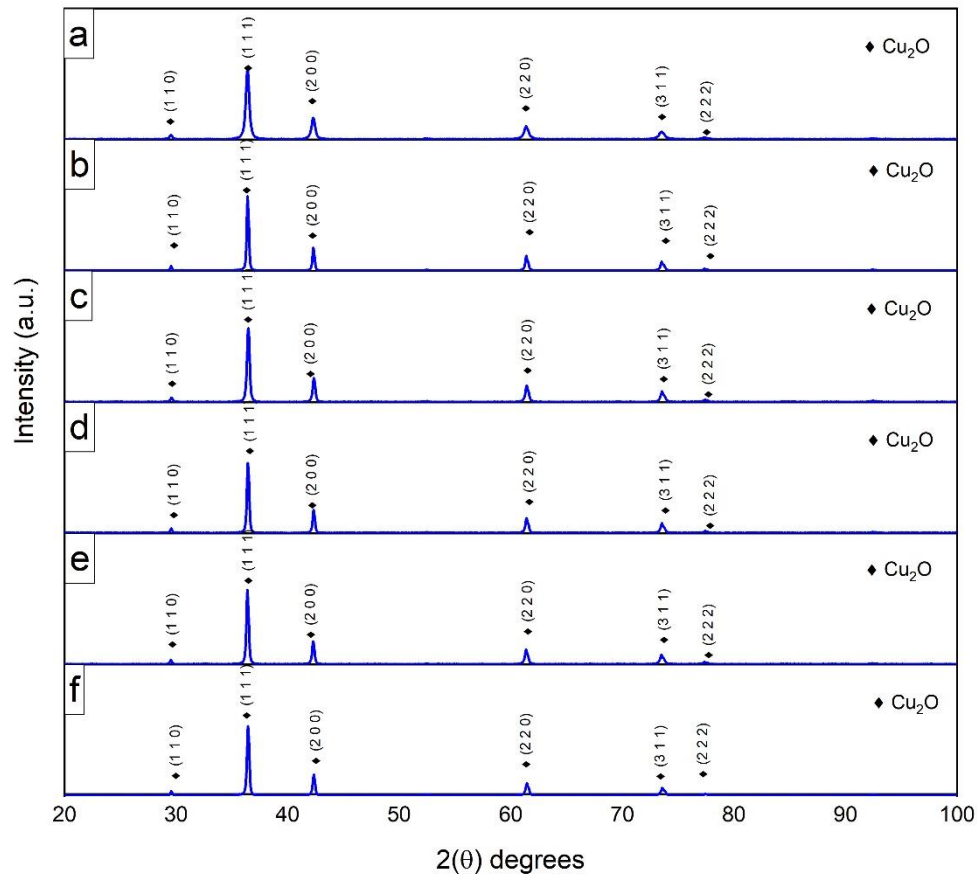


Figure 3.2.1.2.1: XRD spectrum of P1-Cu₂O samples a) P1-Cu₂O-0.01-2-0.6-300, b) P1-Cu₂O-0.01-3-0.6-300, c) P1-Cu₂O-0.01-2-0.9-300, d) P1-Cu₂O-0.01-3-0.9-300, e) P1-Cu₂O-0.01-3-0.9-600 and f) P1-Cu₂O-0.02-6-1.8-600.

Tables 3.2.1.2.1: Crystal size, {220}/{200} peak intensity ratio and {111}/{200} peak intensity ratio of P1-Cu₂O samples.

Samples	Cu ₂ O Crystal Size (nm)	{220}/{200} Peak Intensity Ratio	{110}/{200} Peak Intensity Ratio
P1-Cu ₂ O-0,01-2-0,6-300	28	0,58	3,28
P1-Cu ₂ O-0,01-3-0,6-300	42,5	0,63	3,30
P1-Cu ₂ O-0,01-2-0,9-300	42,5	0,68	3,10
P1-Cu ₂ O-0,01-3-0,9-300	42,5	0,65	3,13
P1-Cu ₂ O-0,01-3-0,9-600	42,5	0,64	3,27
P1-Cu ₂ O-0,02-6-1,8-600	42,5	0,60	3,35

3.2.1.3 FESEM and EDX

Figure 3.2.1.3.1 shows SEM images of P1-Cu₂O-0.01-2-0.6-300 and table 3.2.1.3.1 is the EDX results of the same P1-Cu₂O sample.

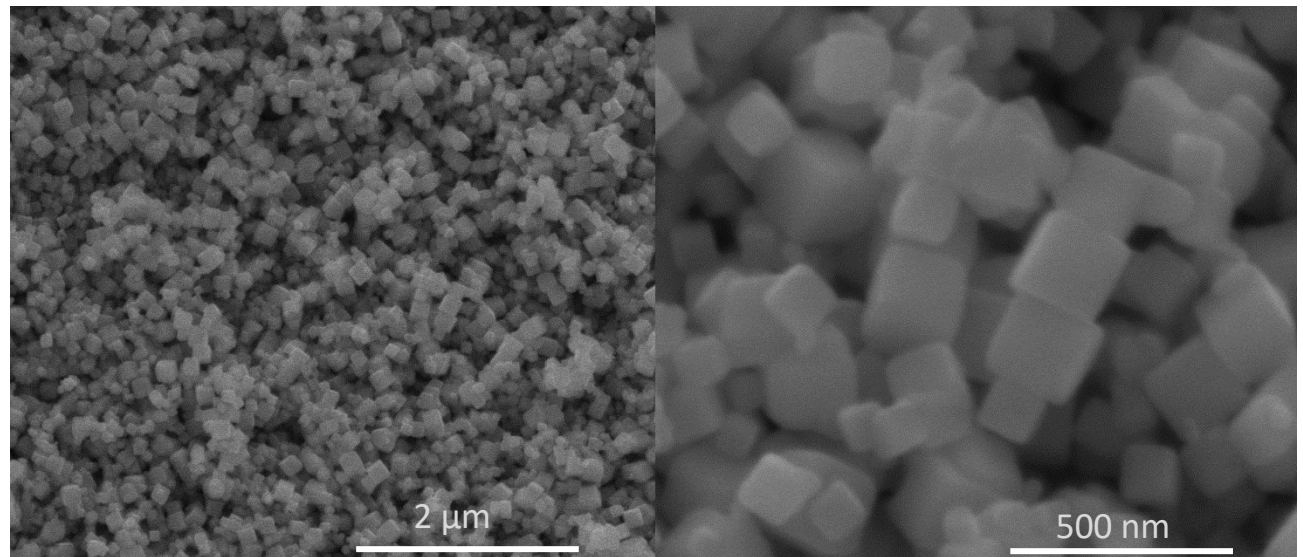


Figure 3.2.1.3.1: FESEM images of cubic nanocrystal Cu₂O at different magnifications.

Table 3.2.3.1: EDX results of P1-Cu₂O-0.01-2-0.6-300 .

Element	Atomic %
Cu	66,81 ± 2,28
O	33,19 ± 2,28

3.2.1.4 BET

Table 3.2.1.4.1 shows the surface area, pore volume and pore size of P1-Cu₂O-0.02-6-1.8-600 and Figure 3.2.1.4.1 presents the BET isotherm curve related to the same sample.

Table 3.2.1.4.1: BET results of P1-Cu₂O-0.02-6-1.8-600.

Sample	Surface Area (m ² /g)	Pore Volume (cm ³ /g)	Pore size (Å)
P1-Cu ₂ O-0.02-6-1.8-600	4.3	0,009	94.4

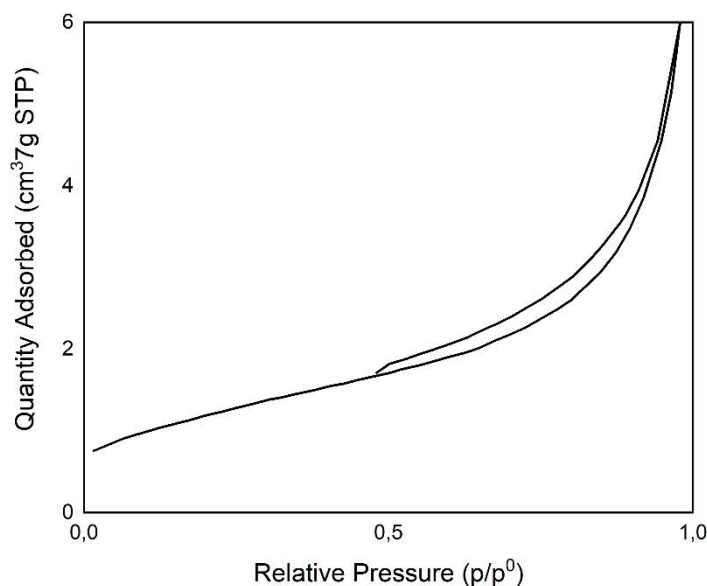


Figure 3.2.1.4.1: BET isotherm curve of P1-Cu₂O-0.02-6-1.8-600.

3.2.1.5 UV-visible absorption spectroscopy

Through the Tau plot method, it is possible to evaluate the energy bandgap of P1-Cu₂O-0.02-6-1.8-600. Figure 3.2.1.5.1 shows the graphs for Tau plot method. The value of the Energy Bandgap (E_g) of P1-Cu₂O-0.02-6-1.8-600 is 2.4 eV.

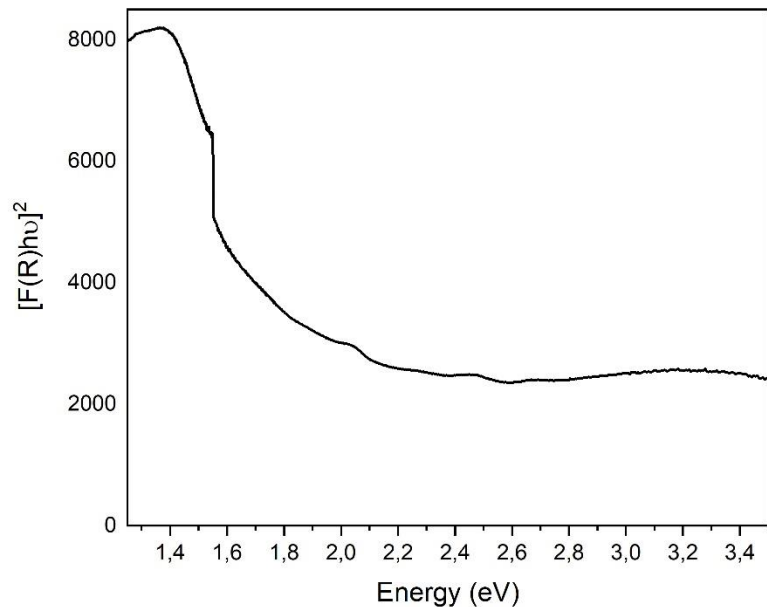


Figure 3.2.1.5.1: UV-visible absorption curve of P1-Cu₂O-0.02-6-1.8-600.

3.2.2 Cu₂O synthesized with C₆H₈O₆ and additional Acid Etching Step

The characterizations, that will be presented, relate to Cu₂O samples synthesized starting from the wet precipitation method [6] with the addition of an acid etching step at pH 5.5.

3.2.2.1 Yield

The paragraph shows the yields of the syntheses in terms of the ratio between grams of copper in the precursor and grams of copper in the Cu₂O obtained. The formulas, used to calculate the yield, are presented in paragraph 3.2.1.1. Table 3.2.2.1.1 shows the grams of CuCl₂ and Cu₂O obtained and respective yields.

Table 3.2.2.1.1: Yields of synthesized samples.

Sample	CuCl ₂ (g)	Cu ₂ O (g)	Yield (%)
P1-Cu ₂ O-0.02-6-1.8-300-Et0	0.67225	0.165	46.13
P1-Cu ₂ O-0.02-6-1.8-300-Et3	0.67225	0.138	38.58

3.2.2.2 XRD

Figure 3.2.2.2.1 presents the XRD spectrum of samples and the reference cards, to analyze XRD results, are reported in Table 3.1.1.1.1. Table 3.2.2.2.1 shows values of crystal size, {220}/{200} peak intensity ratio and {111}/{200} peak intensity ratio of P1-Cu₂O-0,02-6-1,8-300-Et samples.

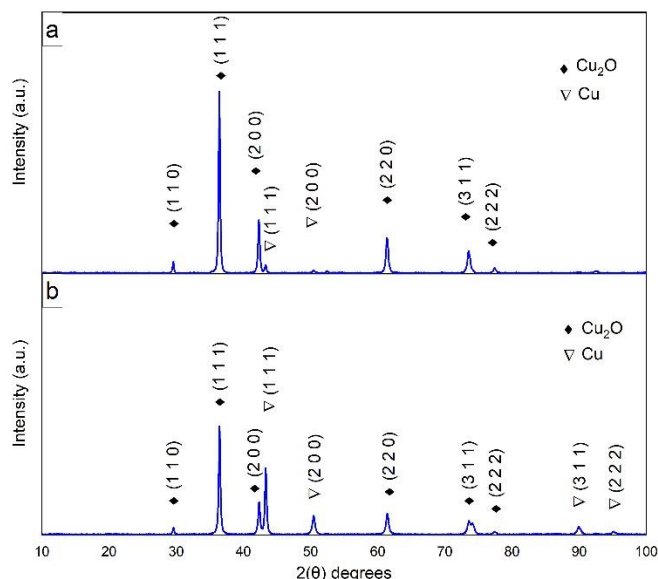


Figure 3.2.2.2.1: XRD spectrum of sample a) P1-Cu₂O-0.02-6-1.8-300-Et0 and b) P1-Cu₂O-0.02-6-1.8-300-Et3.

Tables 3.2.2.2.1: Crystal size, {220}/{200} peak intensity ratio and {111}/{200} peak intensity ratio of P1-Cu₂O-0,02-6-1,8-300-Et samples.

Samples	Cu ₂ O Crystal Size (nm)	{220}/{200} Peak Intensity Ratio	{110}/{200} Peak Intensity Ratio
P1-Cu ₂ O-0.02-6-1.8-300-Et0	37,6	0,63	3,41
P1-Cu ₂ O-0.02-6-1.8-300-Et3	37,7	0,64	3,38

3.2.2.3 BET

Table 3.2.2.3.1 shows the surface area, pore volume and pore size of samples 7 and 8. Figure 3.2.2.3.1 presents the BET isotherm curves related to samples.

Table 3.2.2.3.1: BET results of samples 7 and 8.

Sample	Surface Area (m ² /g)	Pore Volume (cm ³ /g)	Pore size (Å)
P1-Cu ₂ O-0.02-6-1.8-300-Et0	5.5	0.015	109
P1-Cu ₂ O-0.02-6-1.8-300-Et3	7	0.021	122

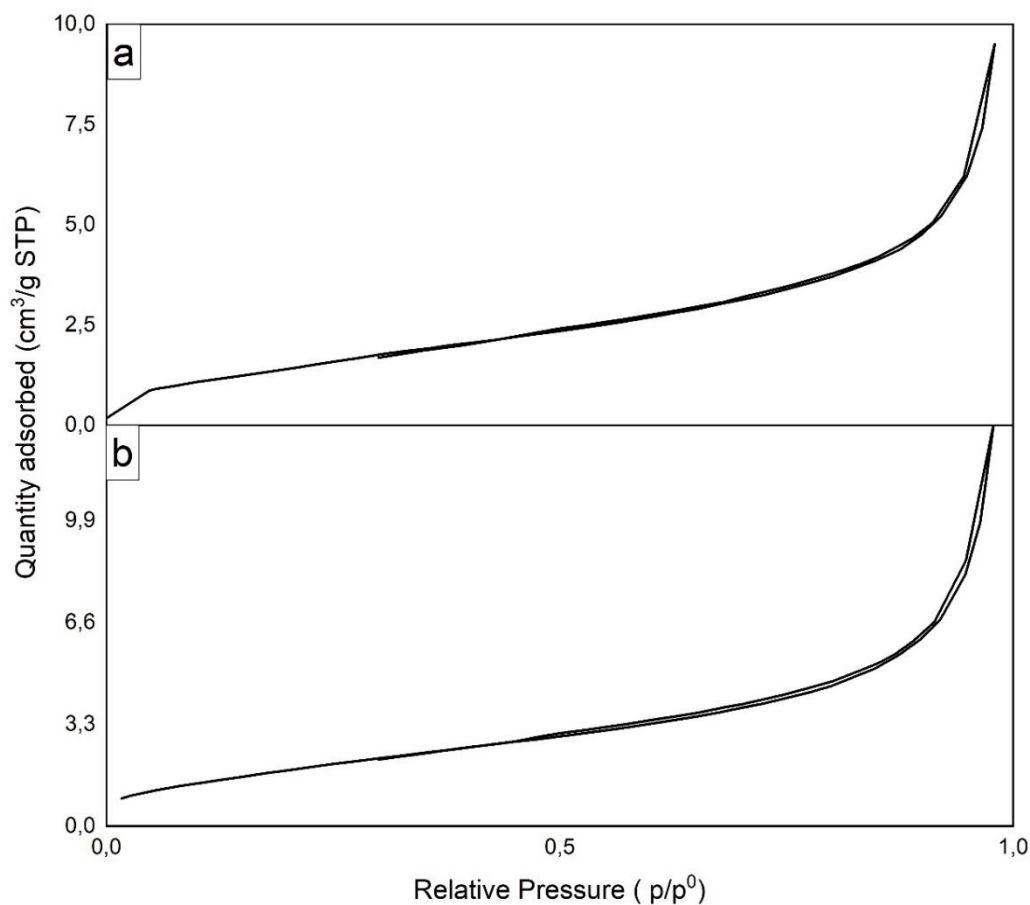


Figure 3.2.2.3.1: BET isotherm curves of sample a) P1-Cu₂O-0.02-6-1.8-300-Et0 and b) P1-Cu₂O-0.02-6-1.8-300-Et3.

3.2.3 Cu₂O synthesized with SDS and NH₂OH*HCl as reducing agent

The samples were synthesized using the method developed by Huang et al. [12], using the quantities of the reagents related to the synthesis of rhombic dodecahedral Cu₂O.

3.2.3.1 Yield

The paragraph shows the yields of the syntheses in terms of the ratio between grams of copper in the precursor and amount of copper in the Cu₂O obtained. The formulas, used to calculate the yield, are presented in paragraph 3.2.1.1. Table 3.2.3.1.1 shows the grams of CuCl₂ and Cu₂O obtained and respective yields.

Table 3.2.3.1.1: Yields of synthesized samples.

Sample	CuCl ₂ (g)	Cu ₂ O (g)	Yield (%)
P2-Cu ₂ O_1	0.67225	0.157	43,89
P2-Cu ₂ O_2	0.67225	0.179	50

3.2.3.2 XRD

Figure 3.2.3.2.1 presents the XRD spectrum of samples and the reference card for analyzing XRD results is 01 077 0199 corresponding to Cu₂O. Table 3.2.3.2.1 shows values of crystl size, {220}/{200} peak intensity ratio and {111}/{200} peak intensity ratio of P2-Cu₂O samples.

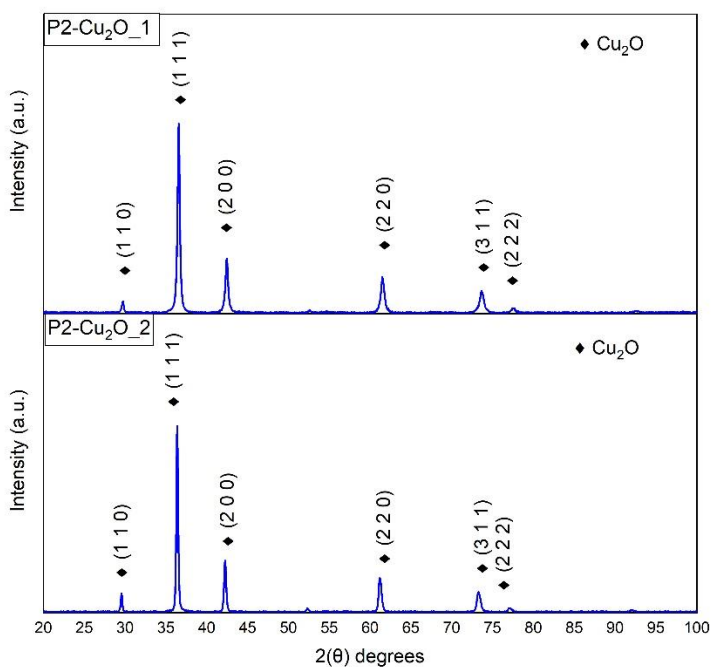


Figure 3.2.3.2.1: XRD spectrum of P2-Cu₂O samples.

Tables 3.2.3.2.1: Crystal size, {220}/{200} peak intensity ratio and {111}/{200} peak intensity ratio of P2-Cu₂O samples.

Samples	Cu ₂ O Crystal Size (nm)	{220}/{200} Peak Intensity Ratio	{110}/{200} Peak Intensity Ratio
P2-Cu ₂ O_1	42,4	0,62	3,70
P2-Cu ₂ O_2	37,7	0,70	3,74

3.2.3.3 SEM and EDX

Figure 3.2.3.3.1 shows SEM images of P2-Cu₂O_2 and table 3.2.3.3.1 is the EDX results of the same P2-Cu₂O sample.

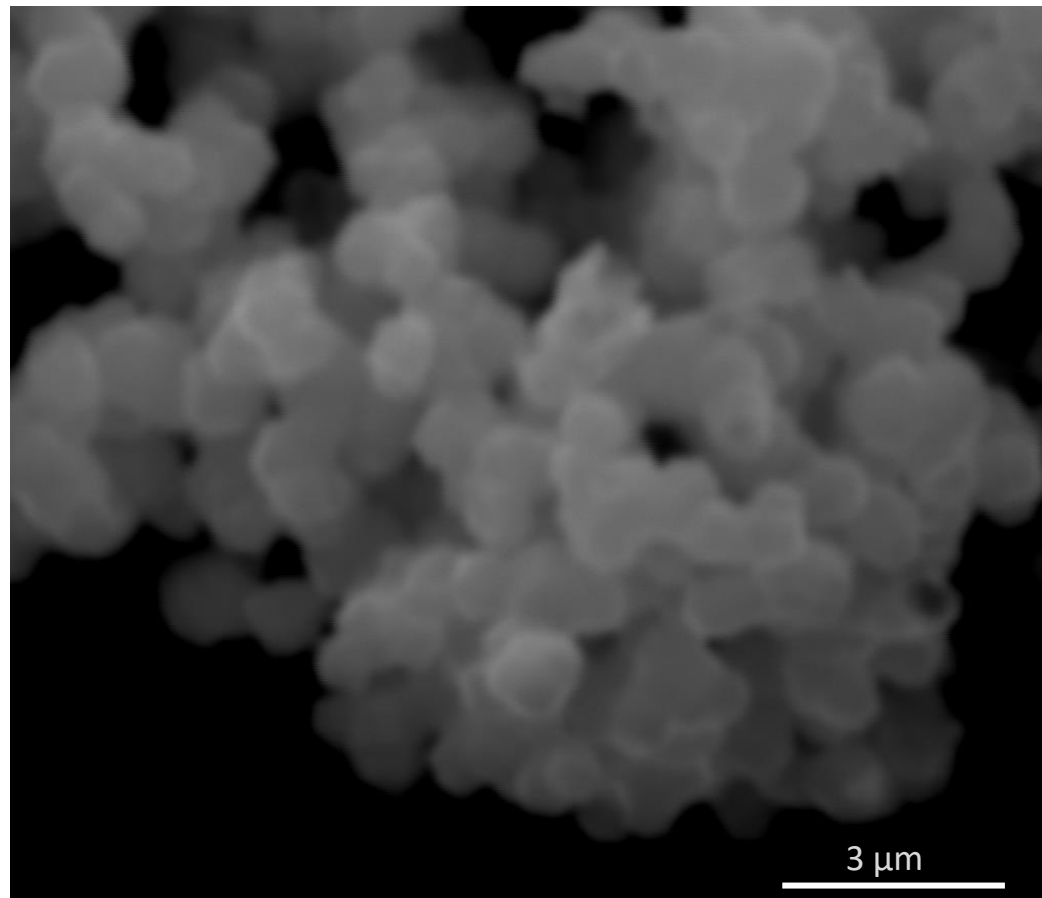


Figure 3.2.3.3.1: SEM images of nanocrystal of P2-Cu₂O₂.

Table 3.2.3.1: EDX results of P2-Cu₂O₂.

Element	Atomic %
O	46,5 ± 4,10
Cu	52 ± 2,99
Cl	1,5 ± 0,62

3.2.4 Cu₂O-SnO₂ Core-Shell catalyst

This chapter shows the characterizations related to the Cu₂O-SnO₂ core-shell samples.

3.2.4.1 XRD

Figure 3.2.4.1.1 presents the XRD spectrum of P1+I-Cu₂O-SnO₂ samples and the reference cards, used to analyze XRD results, are reported in Table 3.1.1.1.1.

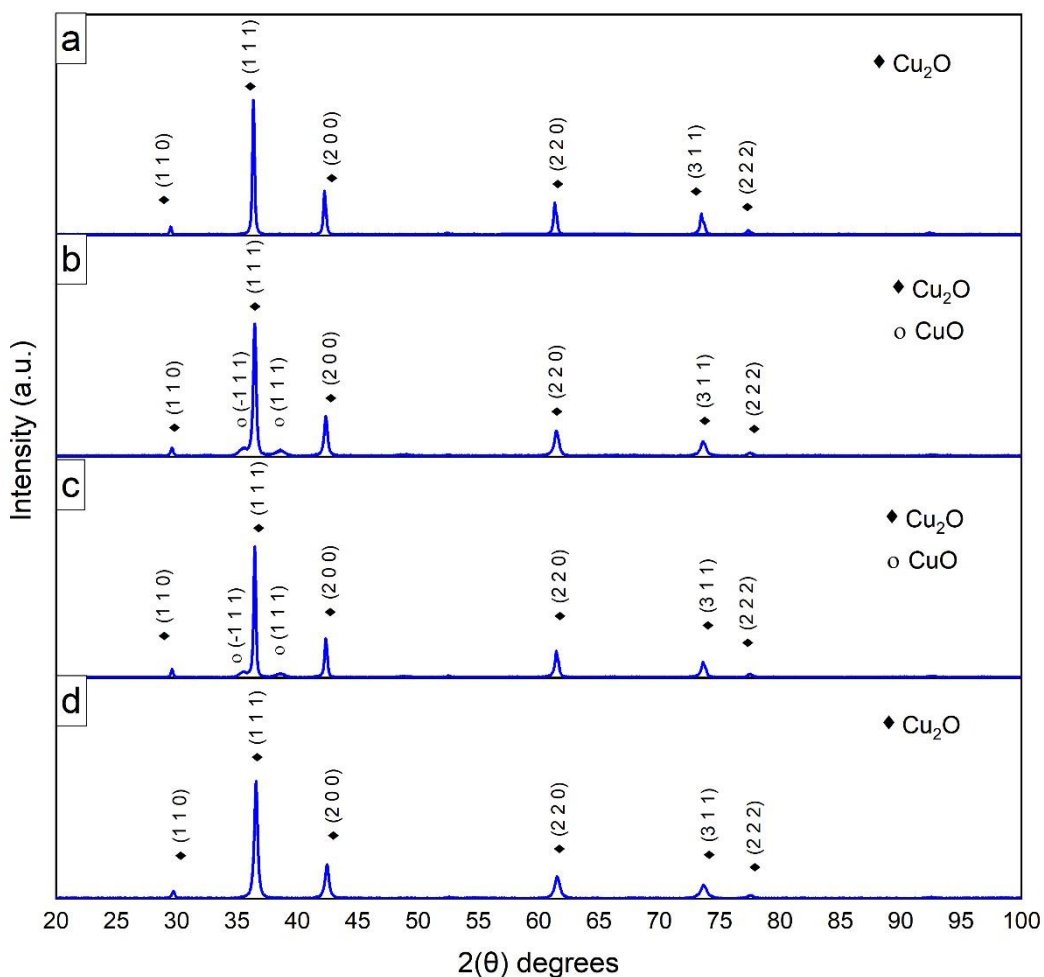


Figure 3.2.4.1.1: XRD spectrum of samples a) P1+I-Cu₂O-SnO₂_1, b) P1+I-Cu₂O-SnO₂_2, c) P1+I-Cu₂O-SnO₂_3, d) P1+I-Cu₂O-SnO₂_4.

3.2.4.2 SEM and EDX

Figure 3.2.4.2.1 shows SEM images of sample P1+I-Cu₂O-SnO₂_4 and Table 3.2.4.2.1 is the EDX results of the same P1+I-Cu₂O-SnO₂ sample.

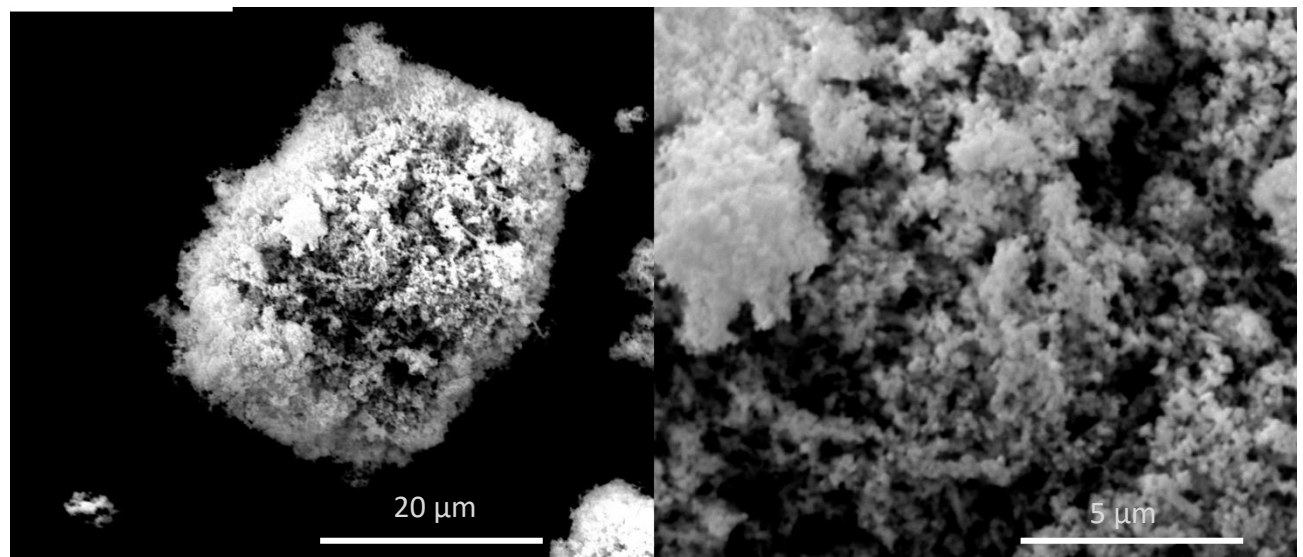


Figure 3.2.4.2.1: SEM images of P1+I-Cu₂O-SnO₂_4

Table 3.2.4.2.1: EDX results of P1+I-Cu₂O-SnO₂_4.

Element	Atomic %
O	50,5 ± 6,87
Cu	48,17 ± 2,60
Sn	0,33 ± 0,007

3.2.4.3 BET

Table 3.2.4.3.1 shows the surface area, pore volume and pore size of the P1+I-Cu₂O-SnO₂ samples. Figure 3.2.4.3.1 presents the BET isotherm curves related to P1+I-Cu₂O-SnO₂ samples.

Table 3.2.4.3.1: BET results of core-shell samples.

Sample	Surface Area (m ² /g)	Pore Volume (cm ³ /g)	Pore size (Å)
P1+I-Cu ₂ O-SnO ₂ -1	20,3	0,032	71,2
P1+I-Cu ₂ O-SnO ₂ -2	11,5	0,029	94,2
P1+I-Cu ₂ O-SnO ₂ -3	8,128	0,016	75,4

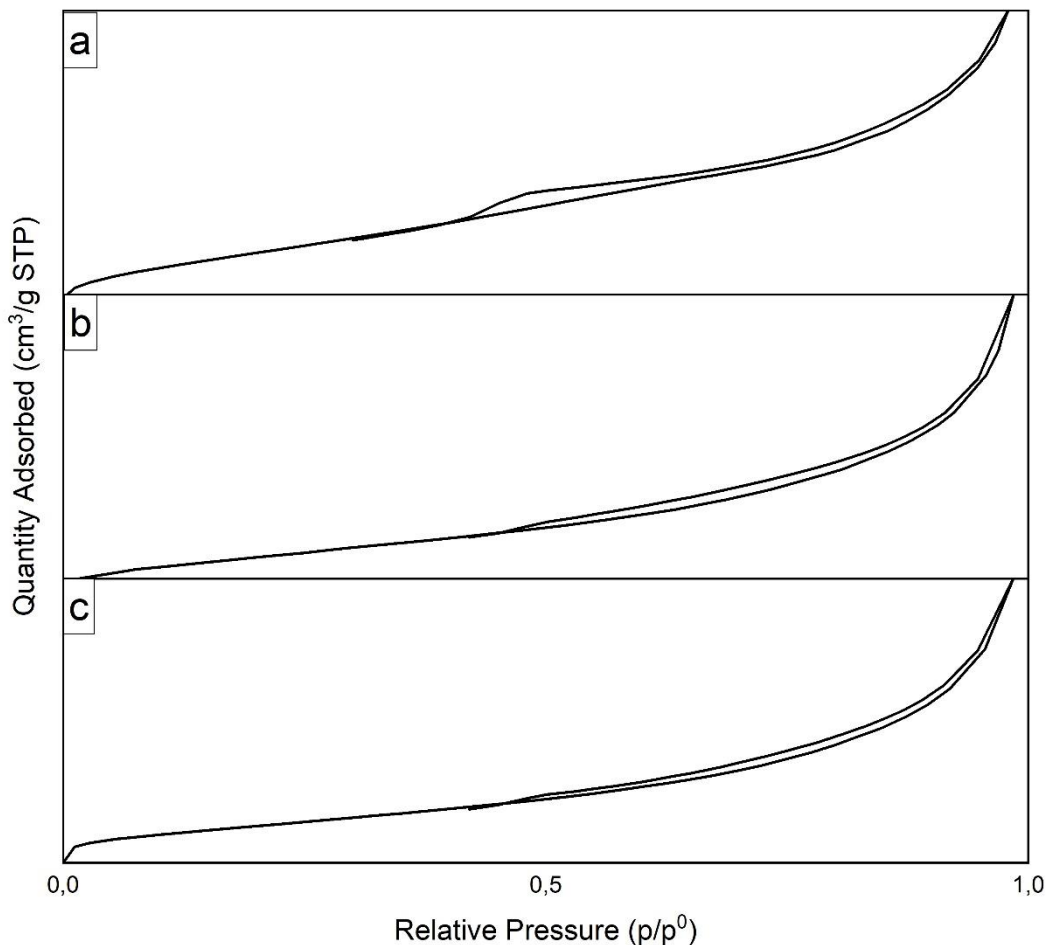


Figure 3.2.4.3.1: BET isotherm curve of samples a) P1+I-Cu₂O-SnO₂_1, b) P1+I-Cu₂O-SnO₂_2 and c) P1+I-Cu₂O-SnO₂_3.

3.2.4.4 UV-visible absorption spectroscopy

Through the Tau plot method, it is possible to evaluate the energy bandgap of sample P1+I-Cu₂O-SnO₂_3. Figure 3.2.4.3.1 shows the graphs for the Tau plot method. The value of Energy Bandgap (E_g) of sample P1+I-Cu₂O-SnO₂_3 is 2.42 eV.

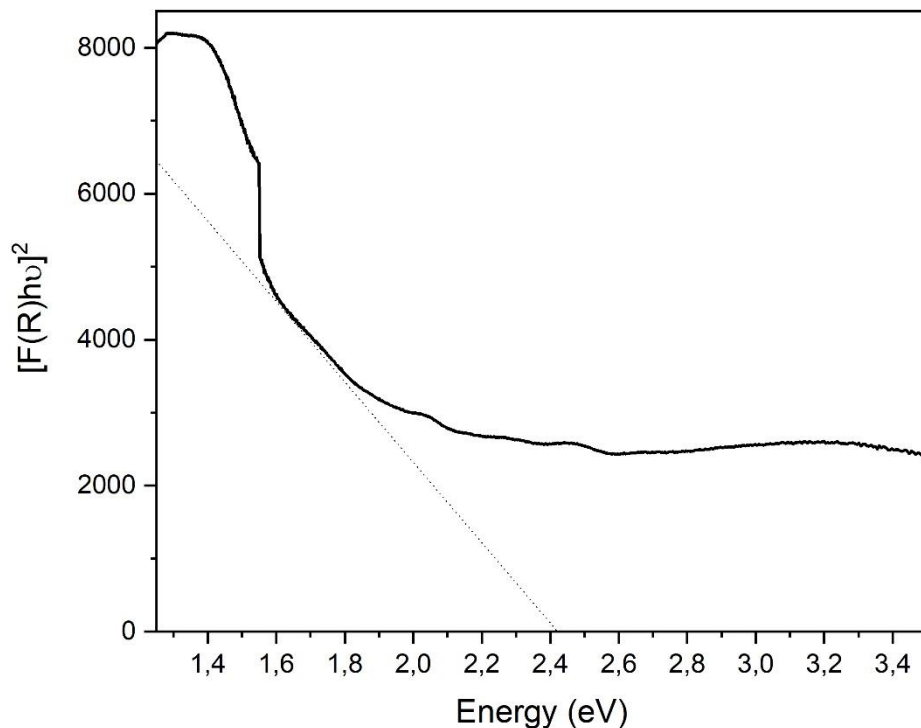


Figure 3.2.4.4.1: UV-visible absorption curve of P1+I-Cu₂O-SnO₂_3.

3.2.5 Result Discussion

3.2.5.1 Cu₂O Samples

Initially, it was tried to increase the yield of copper(I) oxide by varying the concentrations and volumes of the solutions for synthesis by wet precipitation. It was possible to pass from a yield of about 86% for P1-Cu₂O-0.01-2-0.6-300 to about 99% for P1-Cu₂O-0.02-6-1.8-600, as shown in Figure 3.2.5.1.1.

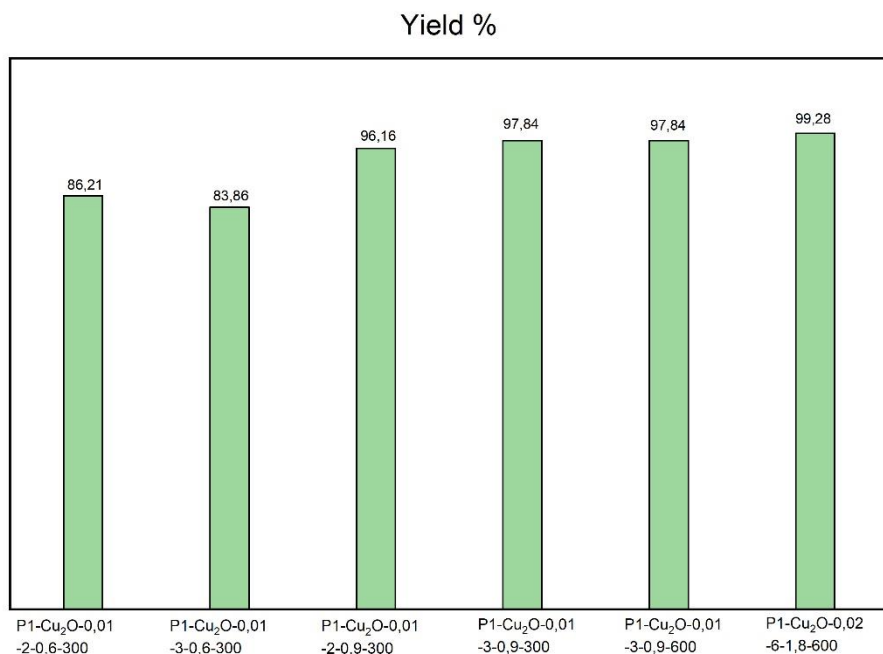


Figure 3.2.5.1.1: Yield of P1-Cu₂O samples.

Significantly lower yields are those obtained for P1-Cu₂O-Et samples and P2-Cu₂O samples. The yields are respectively about 46% for P1-Cu₂O-0.02-6-1.8-300-Et0, about 39% for P1-Cu₂O-0.02-6-1.8-300-Et3, and about 44% for P2-Cu₂O_1 and 50% for P2-Cu₂O_2. This is because the HCl reacts with superficial Cu₂O, modifying the crystalline form and simultaneously consuming copper(I) oxide molecules according to the chemical reaction (3.2.1.1) reported in chapter 3.2.2.

XRD spectra of all Cu₂O samples are clear and the peaks well defined. All the samples show peaks relative only to copper(I) oxide, except for the P1-Cu₂O-Et samples, in which there is also the presence of metallic Cu. The HCl reduced a part of the desired product to metallic copper. This is not the desired result, but it can be an interesting starting point for the synthesis of mixed Cu/Cu₂O catalysts for the electrochemical CO₂ conversion to alcohols. The intensity ratio between the peaks {220} and {200} can be a parameter to distinguish the different crystalline forms of Cu₂O [12]. According to the methodology developed by Zhang et al. [6], P1-Cu₂O-0.01-2-0.6-300 possesses cubic-shaped nanocrystals, information confirmed by the FESEM Figure 4.2.1.3.1. However the synthesized P1-Cu₂O samples show intensity ratios between the peaks {220} and {200} attributable to a crystalline form that is certainly not cubic. These ratios range from 0.6 to 0.7, where 0.6 is relative to Edge- and corner-truncated octahedra, 0.7 to {100} - truncated rhombic dodecahedra, while for nanocubes this ratio is about 0.36 [12]. Another information, that can give validation to the hypothesis of the non-cubicity of the crystalline form of Cu₂O, is the position of the peak of greater intensity. For nanocubes, the 100% intensity peak

is at the 42.5 degrees position, relative to the {200} plane, while for the P1-Cu₂O samples this peak is at about 36.5 degrees, relative to the {111} plane, a typical characteristic of octahedral crystals [6, 37, 38]. From FESEM figure 3.2.1.3.1, the sample P1-Cu₂O-0,01-2-0,6-300 seems to possess cubic crystals even if the XRD spectra possess the previously mentioned characteristics. Probably the crystals have defects not observable by FESEM, but detected by XRD analysis. For the P2-Cu₂O samples, SEM Figure 3.2.3.3.1 shows how obtained Cu₂O nanocrystals are more beveled shape, very similar to the rhombic dodecahedral one, confirming the truthfulness of this synthesis methodology.

From the EDX analysis, it can be seen that from the sample synthesized with C₆H₈O₆ the atomic composition is formed by 66.81% of Cu and 33.19% of O, while for the sample synthesized with Hydroxylammonium Chloride the atomic percentage is 52% of Cu, 46.5% of O and 1.5% of Cl. The presence of Cl can be justified by the fact that NH₂OH * HCl is used as a reducing agent and consequently a small amount of chlorine could remain in the sample.

BET analyzes were carried out on the P1-Cu₂O-0.02-6-1.8-600 and P1-Cu₂O-Et samples. For all two samples, the surface area is extremely low, less than 10 m²/g. Observing the hysteresis of the isothermal curves, it can be seen that also for P1-Cu₂O-0.02-6-1.8-600 the pores probably have a cylindrical shape, while for P1-Cu₂O-Et samples the hysteresis is very similar to the isothermal curve, a sign of a low porosity of the material.

Furthermore, P1-Cu₂O-0.02-6-1.8-600 was subjected to UV-Visible spectroscopy. Using the Tau plot method, the Energy bandgap value obtained is 2.4 eV, which is slightly higher than the values found in the literature [25, 33, 35, 36].

3.2.5.2 Cu₂O-SnO₂ Core-Shell Samples

From XRD analysis, SnO₂ peaks are not present. This is due to the amorphous form of tin (IV) oxide, but above all by the very small quantity used. In fact, from the EDX analysis, the atomic percentage of P1+I-Cu₂O-SnO₂_4 is formed by 50.5% of O, 48.17% of Cu and only 0.33% of Sn. In samples P1+I-Cu₂O-SnO₂_1 and P1+I-Cu₂O-SnO₂_1 there are only Cu₂O peaks, while in P1+I-Cu₂O-SnO₂_2 and P1+I-Cu₂O-SnO₂_3 some CuO peaks are mentioned. This is probably due to exposure to atmospheric O₂, which has oxidized a part of Cu₂O.

Having used the P1-Cu₂O samples to realize core-shell samples, the surface area of the P1+I-Cu₂O-SnO₂ samples is low. Instead as regards the Energy bandgap, its value, relative to the P1+I-Cu₂O-SnO₂_3, is 2.42 eV, very similar to the Cu₂O sample used to synthesize it. The value does not differ to that of P1-Cu₂O-0.02-6-1.8-600, as the quantity of Sn is extremely low.

4-Test

In the following Chapter the RDE and PEC tests carried out on the synthesized samples will be shown.

The electrochemical cell used is subdivided into two half-cells, communicated with each other through a bipolar membrane. Inside the half-cell there are the electrodes, which are conductors of the first kind, on which the oxidation and reduction half-reactions occur, immersed in an electrolytic solution. The electrode, in which the reduction half-reaction takes place, is called the cathode, while the one, in which the oxidation half-reaction happens, is called the anode. The cell typology is the one with three electrodes: the working electrode (WE); the reference electrode (RE); the counter electrode (CE). The working electrode is the one in which the redox half reaction of interest takes place, where the ink, which contains the catalyst, is deposited. The reference electrode has a stable potential, through which it is possible to strictly control the potential applied to the working electrode. The counter electrode is the one in which the second half reaction takes place and respect to that it is measured the total current flowing in the system. The electrodes are connected through terminals to a potentiostat, thanks to which it is possible to obtain information on the samples through techniques, such as chronoamperometry (CA), chronopotentiometry (CP), linear sweep voltammetry (LSV) and cyclic voltammetry (CV). In the CA, the potential is kept constant and the current is measured as a function of time, while in the CP the current is constant and the potential varies over time. In voltammetric techniques, the current is measured as a function of the potential, which is made to vary linearly in the LSV, while in the CV the potential varies with a triangular shape, increasing linearly up to a certain value and then decreasing with a linear trend [39].

RDE tests are electrochemical test and the working electrode is a rotating disk electrode, on which the ink, containing the catalyst, is deposited inside the dark central circle, made by a conductor of the first species, a glassy carbon in the present case, coated with a polymeric material, like Teflon [39]. On the other hand, PEC tests are photo-electrochemical tests, in which there is a lamp that emits visible light in order to simulate sunlight. Through this type of test, it is possible to evaluate the contribution of the photo-activity and whether this contribution significantly improves the performances of the catalyst during test. In this case, the working electrode is made by a support in carbon paper, in which the active area is 1 cm^2 , where the ink containing the catalyst is deposited. As regards the reference electrode, the Ag/AgCl (3,5 M KCl Sat.) electrode is used as a RE for both types of tests. The Pt electrode is used as a counter electrode in both tests and only difference is the shape of CE, mesh in PEC test and wire in RDE test. Instead, the electrolytic solution used is a 0.1 M KHCO₃ for RDE test. 50 mL of this solution is in the "cathode" cell, in which there is WE and RE, and 29 mL is in the "anode" cell, where there is CE. For PEC test, 28 mL of 0,1 M KOH solution is in the anode, while 50 mL of 0,1 M KHCO₃ solution is in the cathode. Figure 4.1 and Figure 4.2 show set-ups of RDE tests and PEC test, respectively.

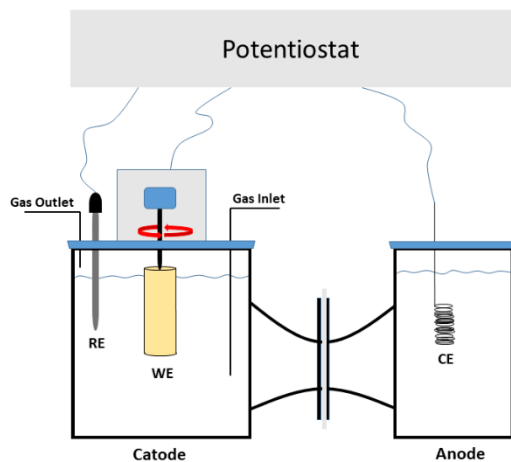


Figure 4.1: RDE test set-up.

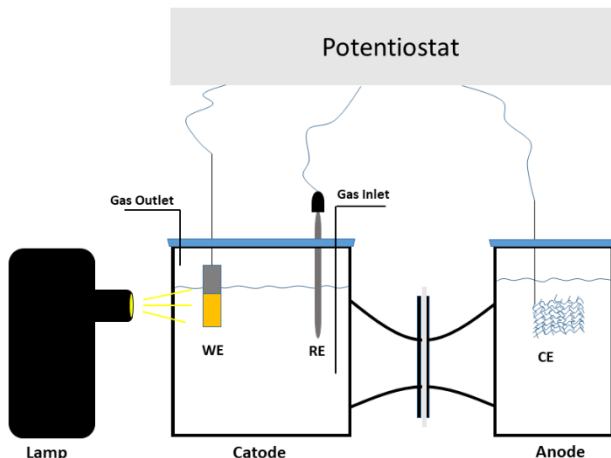


Figure 4.2: PEC test set-up.

For the preparation of the inks, the percentage ratios have been calculated with respect to the quantity of catalyst, i.e. the quantity of the component divided by that of the catalyst multiplied by 100. The RDE ink consists of 0,18 % of Vulcan Carbon, 1,90 % of catalyst, 16,38 % of Nafion and 81,54 % of isopropanol. This solution is placed in ultrasound for about 20 minutes in order to have an ink as homogeneous and uniform as possible. The volume of ink to be deposited on the rotating disk electrode is such as to have a catalyst loading equal to 1 mg/cm^2 . For PEC ink, its composition consists of 4,17% of catalyst, 12,5 % of Nafion and 83,33 % of Ethanol. Also this solution was sonicated for 20 minutes and, through an airbrush, is sprayed on the carbon paper, placed on a plate at 50°C in order to evaporate the Nafion and the ethanol. Finally, the electrode used is the one with catalyst loading equal to 1 mg/cm^2 .

Tested samples in the RDE test are P1-Cu₂O-0.02-6-1.8-300-Et0 and P1-Cu₂O-0.02-6-1.8-300-Et0 , while those for the PEC test are P1-Cu₂O-0.02-6-1.8-600, P1+I-Cu₂O-SnO₂_4 and CP-Cu₂O-SnO₂-pH7 and CP-Cu₂O-pH7-0.6-1-0.3. Test results will be presented by comparing the samples for synthesis method and for chemical species.

4.1 Comparison of test results by synthesis method

In this paragraph, the test results will be shown, comparing the samples according to the synthesis methodology. In particular, the results of the sample P1-Cu₂O-0.02-6-1.8-600 will be compared with those of P1+I-Cu₂O-SnO₂-4 and the results of the sample CP-Cu₂O-pH7-0.6-1.0.3 with those of the CP-Cu₂O-SnO₂-pH7.

4.1.1 Comparison between P1-Cu₂O-0.02-6-1.8-600 and P1+I-Cu₂O-SnO₂-4

Figure 4.1.1.1 shows cyclic voltammetries in N₂ and CO₂, while Figure 4.1.1.2 presents liner sweep voltammetries in N₂ and CO₂.

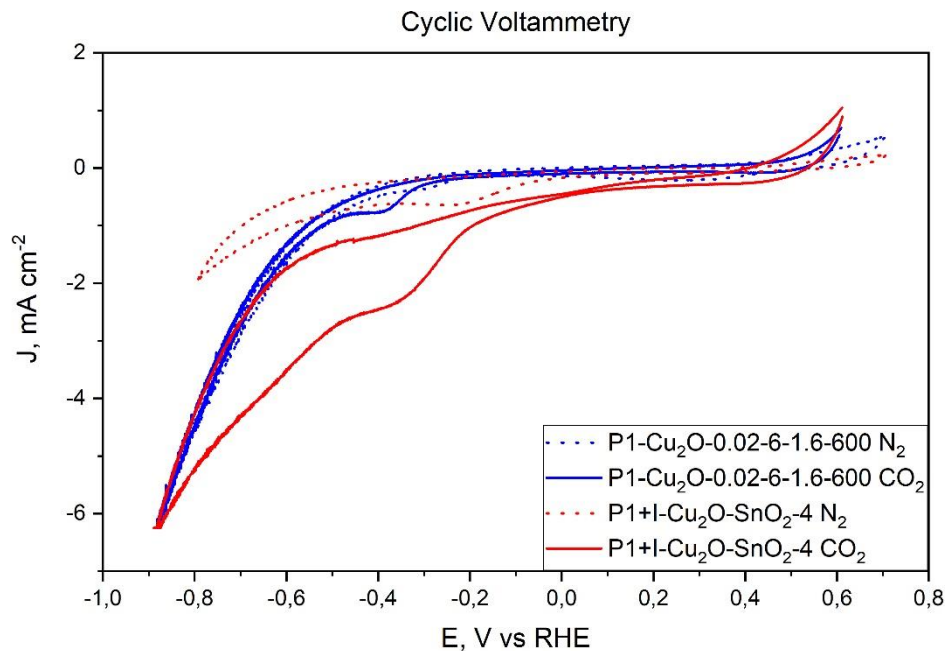


Figure 4.1.1.1 Cyclic voltammetries in N₂ and CO₂ of samples P1-Cu₂O-0.02-6-1.8-600 and P1+I-Cu₂O-SnO₂-4.

From literature, the standard reduction potential of Cu²⁺ to Cu is 0.340 V vs RHE, while the potential to reduce Cu⁺ to Cu is 0.522 V vs RHE [40]. Observing the CVs it can be seen that the sample P1-Cu₂O-0.02-6-1.8-600 presents a reduction peak in N₂ around 0.260 V vs RHE, not present in the sample P1+I-Cu₂O-SnO₂-4. This means that a part of the sample without SnO₂ has probably reduced, while SnO₂ containing sample does not present changes at that potential. This may be the confirmation of the protective role of SnO₂ towards Cu₂O, increasing its stability. On the other hand, the CVs in CO₂ did not show clear reduction peaks for both samples. Paying attention to the shape of the CV curves and the closed area inside them, it can be seen that the CVs of the sample P1+I-Cu₂O-SnO₂-4 have a larger internal area than those of the sample P1-Cu₂O-0.02-6-1.8-600, especially in CO₂. This highlights how Sn can increase the capacitive effect compared to the tin-free sample [43].

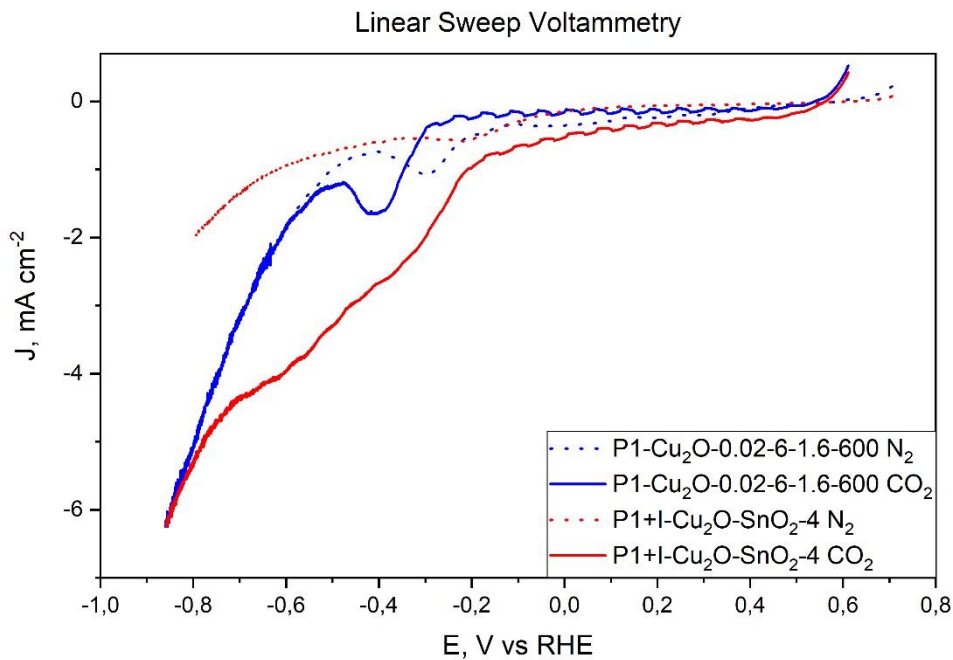


Figure 4.1.1.2: Linear sweep voltammetries in N₂ and CO₂ of samples P1-Cu₂O-0.02-6-1.8-600 and P1+I-Cu₂O-SnO₂-4.

As regards the LSVs, the sample P1-Cu₂O-0.02-6-1.8-600 shows evident reduction peaks in N₂ and CO₂ respectively at -0.3 V and -0.4 V, while the sample P1+I-Cu₂O-SnO₂-4 shows a reduction peak only in N₂ at -0.21 V. LSV curves in CO₂ show an oscillating trend in the potential range from -0.3 V to about 0.45 V. This is due to the fact that, during the linear sweep voltammetry test, samples were alternated by periods of dark and periods of light. A faradic gain due to light radiation can be noted, which is irrelevant more or less for potentials lower than -0.3 V vs. RHE, looking at the graph. Table 4.1.1.1 shows the on-set potential values of both samples in N₂ and CO₂.

Table 4.1.1.1: on-set potential values of P1-Cu₂O-0.02-6-1.8-600 and P1+I-Cu₂O-SnO₂-4 in N₂ and CO₂.

Sample	On-set potential (V)	
	N ₂	CO ₂
P1-Cu ₂ O-0.02-6-1.8-600	-0.533	-0.530
P1+I-Cu ₂ O-SnO ₂ -4	-0.532	-0.458

Comparing the on-set potentials, it can be seen that in the sample P1-Cu₂O-0.02-6-1.8-6 the values in N₂ and CO₂ are very close and equal to -0.533 V and -0.530 V respectively. The fact that this parameter in CO₂ is smaller in modulus is positive, because it indicates that the carbon dioxide reduction reaction occurs at lower potentials. As regards the sample P1+I-Cu₂O-SnO₂-4 the on-set potentials values are around -0.532 V in N₂, as for the sample P1-Cu₂O-0.02-6-1.8-600, and -0.458 V in CO₂. This last value is interesting since, being smaller in modulus than the value of the other sample, the Sn, in the small quantities used, could have improved the activity towards CO₂.

Figures 4.1.1.3 and 4.1.1.4 show the chronoamperometries in CO₂ at -100 mV and -250 mV respectively. Table 4.1.1.2 shows light faradic gain for both samples in CA at -100 mV and at -250 mV.

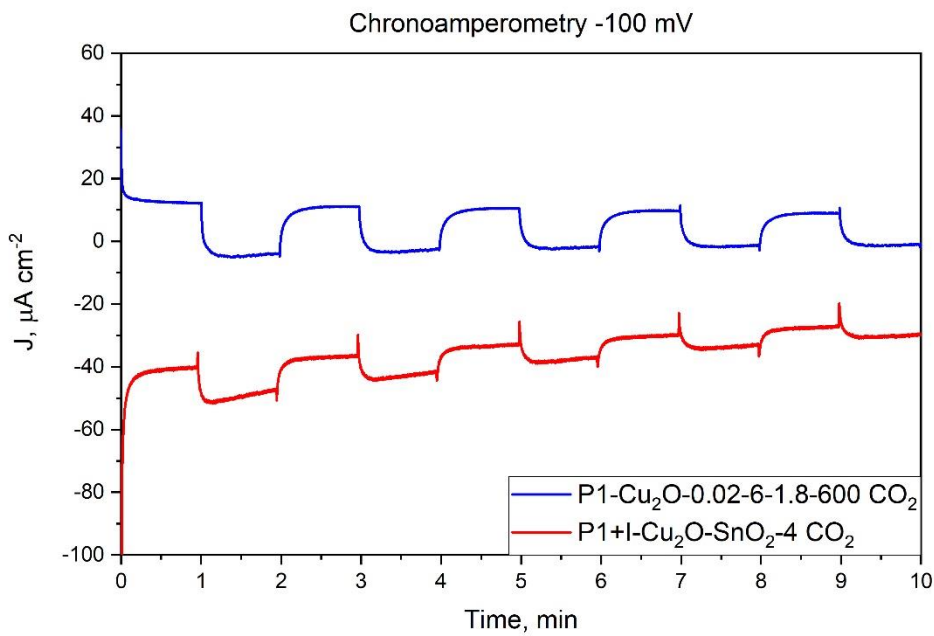


Figure 4.1.1.3: Chronoamperomtries in CO₂ of samples P1-Cu₂O-0.02-6-1.8-600 and P1+I-Cu₂O-SnO₂-4 at -100 mV.

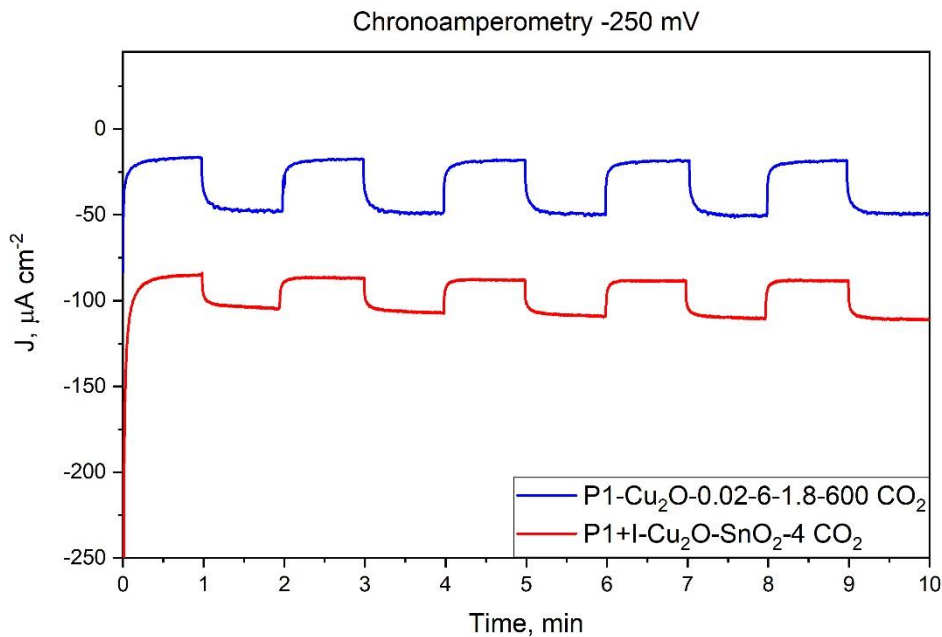


Figure 4.1.1.4: Chronoamperometries in CO₂ of samples P1-Cu₂O-0.02-6-1.8-600 and P1+I-Cu₂O-SnO₂-4 at -250 mV.

Table 4.1.1.2: Light faradic gain on average for samples P1-Cu₂O-0.02-6-1.8-600 and P1+I-Cu₂O-SnO₂-4 in CA at -100mV and at -250 mV.

Sample	Light Faradic Gain ($\mu\text{A cm}^{-2}$)	
	CA -100 mV	CA -250 mV
P1-Cu ₂ O-0.02-6-1.8-600	-13.1	-30.7
P1+I-Cu ₂ O-SnO ₂ -4	-5.2	-20.3

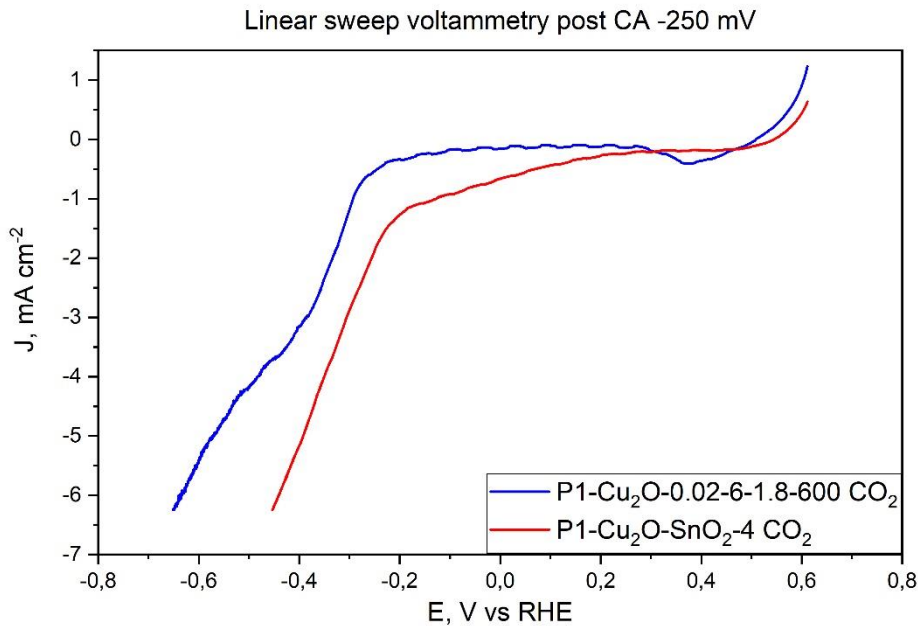


Figure 4.1.1.5: post CA at -250 mV Linear sweep voltammetries of samples P1-Cu₂O-0.02-6-1.8-600 and P1+I-Cu₂O-SnO₂-4.

Post CA -250 mV LSVs in CO₂ still show a slight fluctuating trend, especially sample P1-Cu₂O-0.02-6-1.8-600. This means that the tested samples maintain a certain photo-activity and an interesting aspect is the fact that the current density J increases in modulus for both samples. However, P1-Cu₂O-0.02-6-1.8-600 has a reduction peak in 0.37 V vs. RHE, a value very close to the reduction potential of Cu²⁺ at Cu (0.340 V). This could be due to the fact that Cu₂O could be self-oxidized during water reduction, given that H₂ FE is about 88%, as reported by Kakuta and Abe [18]. Moreover, works in the literature show how Cu₂O can oxidize to CuO under illumination [17]. Therefore, also the illumination could be the cause of this hypothetical oxidation. Instead the sample P1+I-Cu₂O-SnO₂-4 does not show reduction peaks, highlighting again the protective function of SnO₂ against possible reduction of Cu₂O.

Finally, Figure 4.1.1.5 shows a linear sweep voltammetry post CA in CO₂ at -250 mV, while figure 4.1.1.6 shows a chronopotentiometry in CO₂ at -1 mA

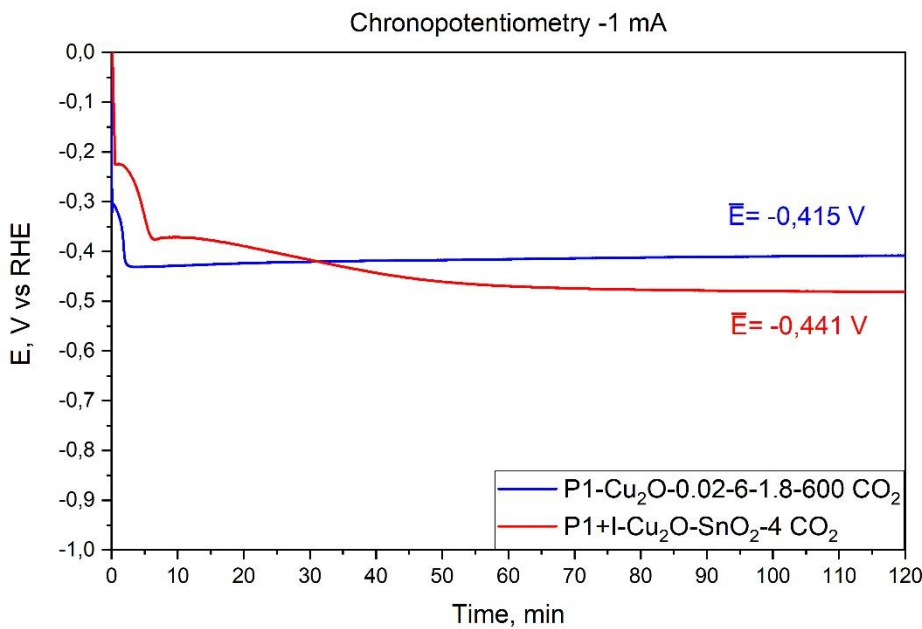


Figure 4.1.1.6: Chronopotentiometries in CO₂ at -1 mA of samples P1-Cu₂O-0.02-6-1.8-600 and P1+I-Cu₂O-SnO₂-4.

Observing the CP curves, the average values of potentials are around -0.415 V for P1-Cu₂O-0.02-6-1.8-600 and -0.441 V for P1+I-Cu₂O-SnO₂-4. This indicates that the sample with tin, subjected to a current of -1 mA, generates a greater potential in modulus. Moreover, the peculiarity is in the fact that the CP of the sample P1+I-Cu₂O-SnO₂-4 decreases until it reaches a quasi-stationary value equal to -0.480 V vs. RHE, while the CP of the sample without the tin shows an increasing trend with an almost steady -0.408 V vs. RHE. This decreasing trend may be due to the fact that SnO₂ has a lower conductivity than Cu₂O [44,45], and therefore the potential stabilizes at a larger value in modulus.

4.1.2 Comparison between CP-Cu₂O-pH7-0.6-1-0.3 and CP-Cu₂O-SnO₂-pH7

Figure 4.1.2.1 shows cyclic voltammetries in N₂ and CO₂, while Figure 4.1.2.2 presents liner sweep voltammetries in N₂ and CO₂.

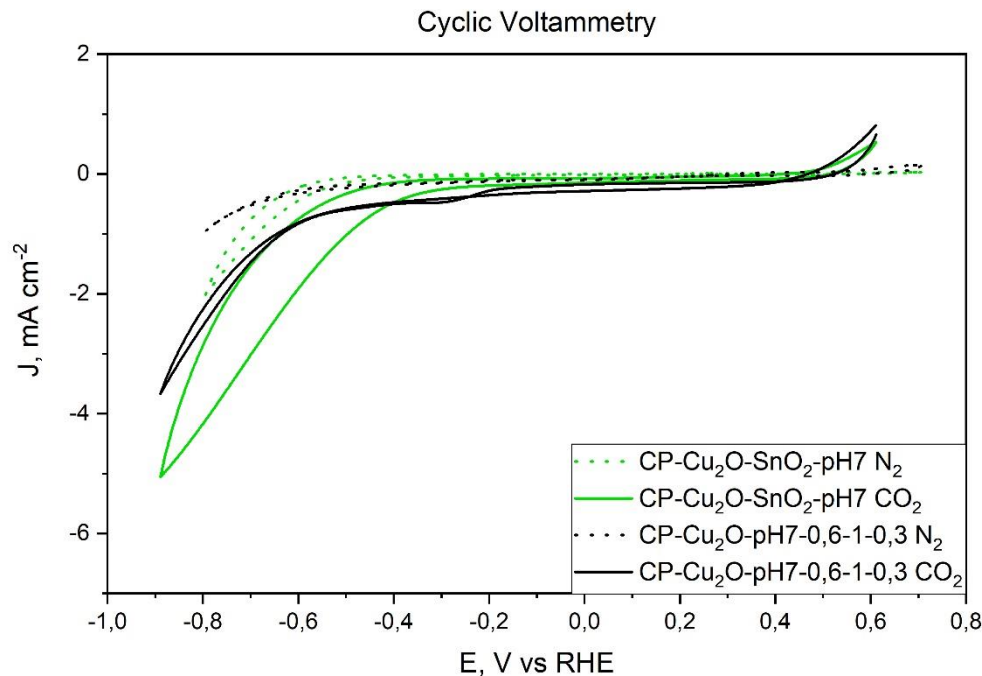


Figure 4.1.2.1 Cyclic voltammetries in N₂ and CO₂ of samples CP-Cu₂O-SnO₂-pH7 and CP-Cu₂O-pH7-0,6-1-0,3.

As in the previous comparison between the samples P1-Cu₂O-0.02-6-1.8-600 and P1+I-Cu₂O-SnO₂-4, the sample containing SnO₂ has a larger area inside the CVs than the tin-free sample, further confirming the property of SnO₂ to improve the capacitive effect of the sample [43]. Moreover, the CP-Cu₂O-pH7-0.6-1-0.3 sample shows a CO₂ reduction peak at about -0.3 V vs. RHE, not present in the CP-Cu₂O-SnO₂-pH7 sample, further confirming the protective function of SnO₂.

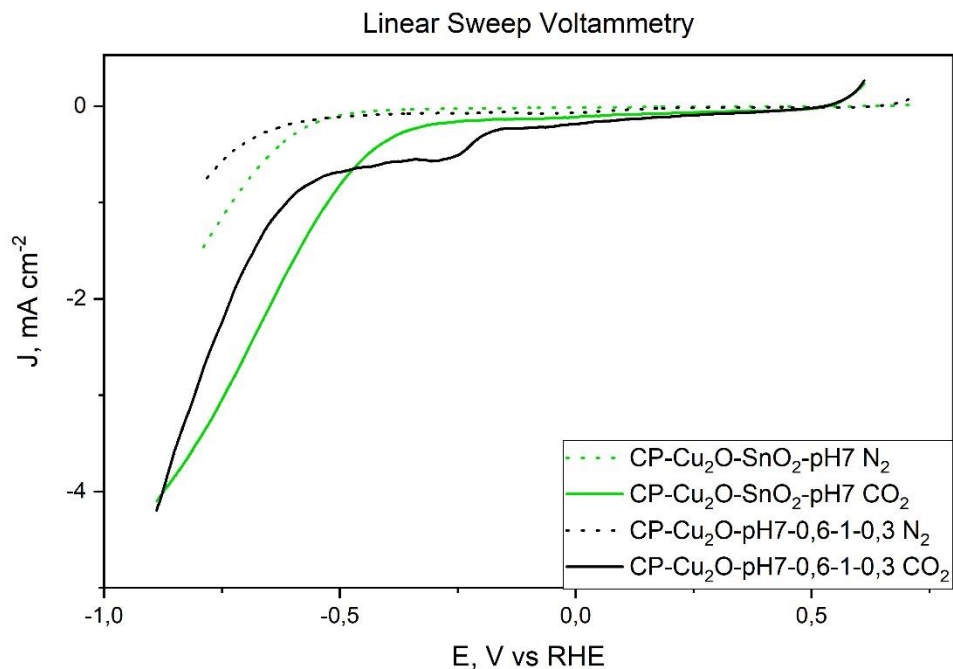


Figure 4.1.2.2: Linear sweep voltammetries in N₂ and CO₂ of samples CP-Cu₂O-SnO₂-pH7 and CP-Cu₂O-pH7-0,6-1-0,3.

As in the previous CVs graph, the only reduction peak is that of the CP-Cu₂O-pH7-0,6-1-0,3 at -0.3 V vs. RHE. Table 4.1.1.1 shows the on-set potential values of both samples in N₂ and CO₂.

Table 4.1.2.1: on-set potential values of CP-Cu₂O-pH7-0,6-1-0,3 and CP-Cu₂O-SnO₂-pH7 in N₂ and CO₂.

Sample	On-set potential (V)	
	N ₂	CO ₂
CP-Cu ₂ O-pH7-0,6-1-0,3	-0.656	-0.620
CP-Cu ₂ O-SnO ₂ -pH7	-0.578	-0.444

Also in this case, on-set potentials values are smaller in modulus in CO₂, specifically those of the CP-Cu₂O-SnO₂-pH7 sample are lower in modulus than the tin-free sample, giving a possible confirmation to the fact that SnO₂ can improve activity towards CO₂. Furthermore, these curves did not have an oscillating trend due to the faradic gain of the light. This is to say that this gain in photo-current is zero or very small with respect to the electrochemical contribution.

Figures 4.1.2.3 and 4.1.2.4 show the chronoamperometries in CO₂ at -100 mV and -250 mV respectively. Table 4.1.2.2 shows light faradic gain for both samples in CA at -100 mV and at -250 mV.

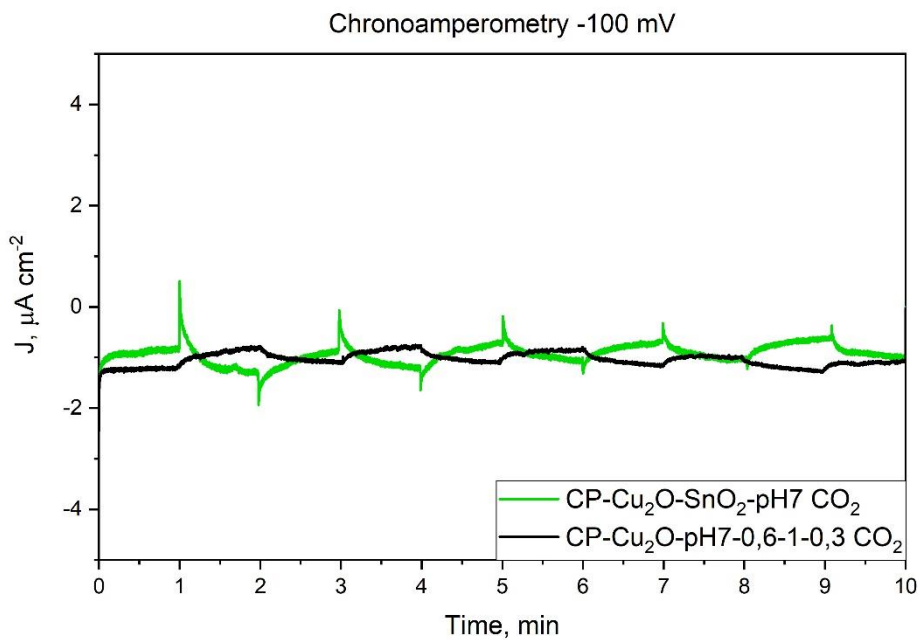


Figure 4.1.2.3: Chronoamperomtries in CO₂ of samples CP-Cu₂O-SnO₂-pH7 and CP-Cu₂O-pH7-0,6-1-0,3 at -100 mV.

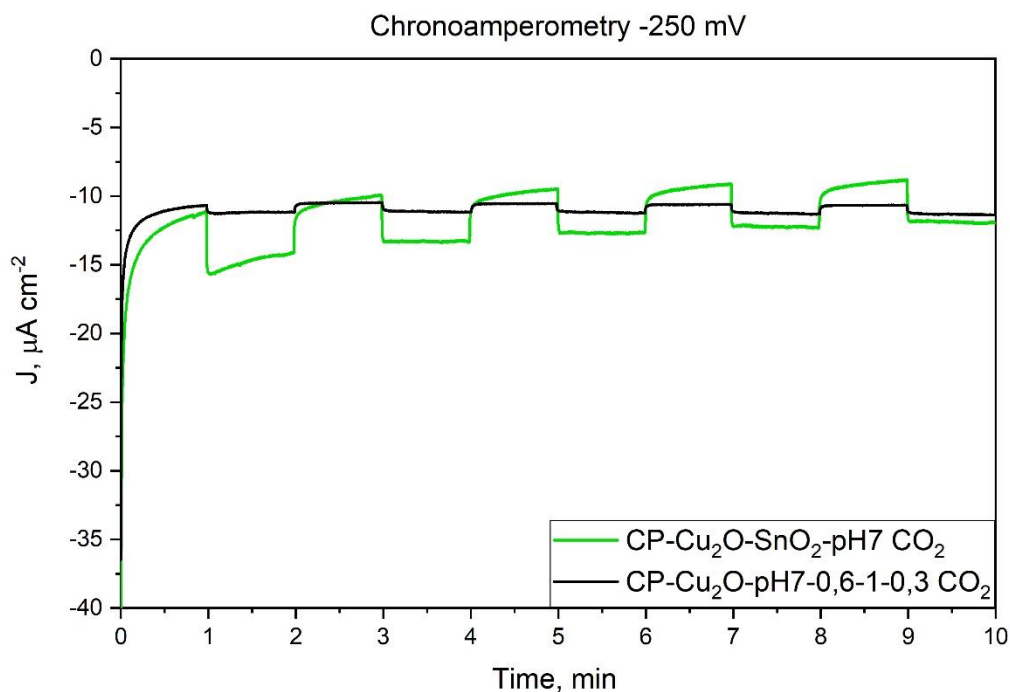


Figure 4.1.2.4: Chronoamperomtries in CO₂ of samples CP-Cu₂O-SnO₂-pH7 and CP-Cu₂O-pH7-0,6-1-0,3 at -250 mV.

Table 4.1.2.2: Light faradic gain on average for samples CP-Cu₂O-SnO₂-pH7 and CP-Cu₂O-pH7-0,6-1-0,3 in CA at -100mV and at -250 mV.

Sample	Light Faradic Gain ($\mu\text{A cm}^{-2}$)	
	CA -100 mV	CA -250 mV
CP-Cu ₂ O-SnO ₂ -pH7	-0.2662	-0.65
CP-Cu ₂ O-pH7-0,6-1-0,3	-0.2587	-2.80

Finally, Figure 4.1.2.5 shows a linear sweep voltammetry post CA in CO₂ at -250 mV, while figure 4.1.2.6 shows a chronopotentiometry in CO₂ at -1 mA.

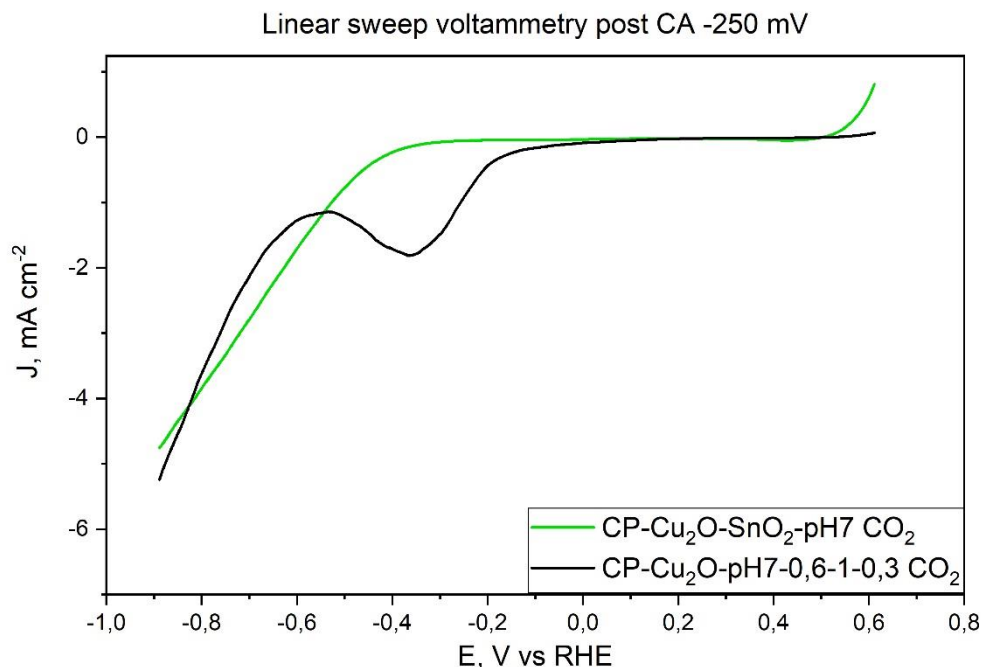


Figure 4.1.2.5: Linear sweep voltammetries in CO₂ post CA at -250 mV of samples CP-Cu₂O-SnO₂-pH7 and CP-Cu₂O-pH7-0,6-1-0,3.

Observing post CA -250 mV LSVs, the CP-Cu₂O-pH7-0.6-1-0.3 sample shows a reduction peak at -0.37 V, while the CP-Cu₂O-SnO₂-pH7 sample shows no peaks. This is the confirmation that, also through the synthesis method by co-precipitation, SnO₂ plays an essential role in keeping the sample stable and unaltered.

Finally, Figure 4.1.2.5 shows a linear sweep voltammetry post CA in CO₂ at -250 mV, while figure 4.1.2.6 shows a chronopotentiometry in CO₂ at -1 mA.

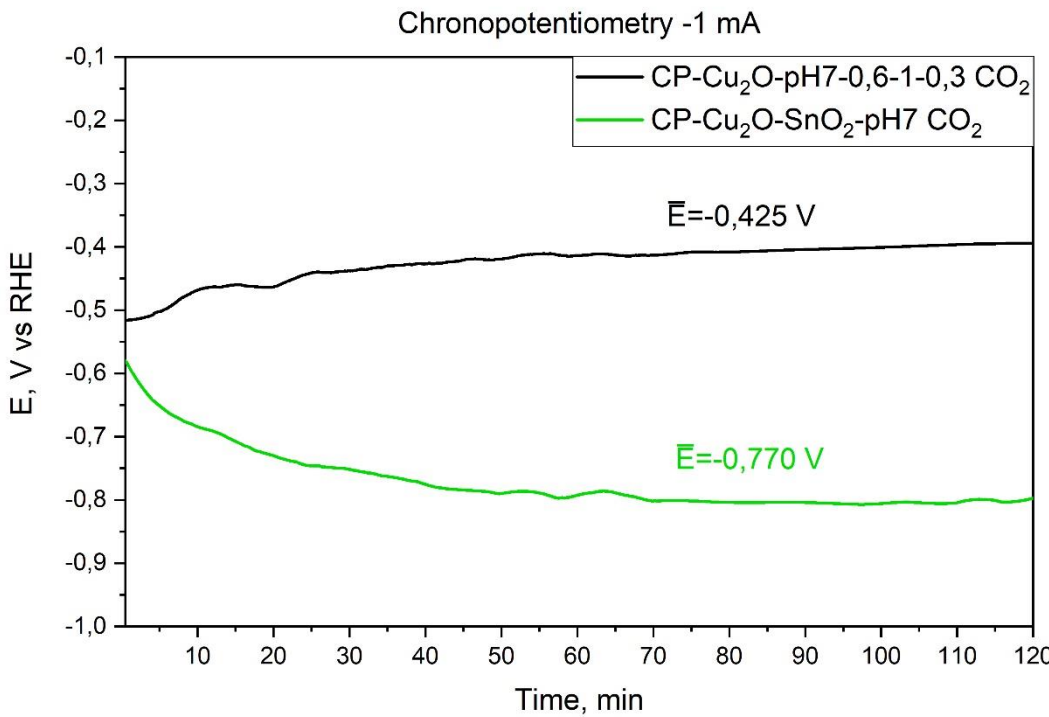


Figure 4.1.2.6: Chronopotentiometries in CO₂ at -1 mA of samples CP-Cu₂O-SnO₂-pH7 and CP-Cu₂O-pH7-0,6-1-0,3.

Interesting aspect, which catches the attention, is the decreasing trend of the CP of the sample containing SnO₂ and increasing trend of the one without tin. Therefore, SnO₂ is probably the cause of this behavior. Furthermore, the value gap between the two curves is very pronounced and could be due to the greater quantity of tin oxide (IV) in the sample synthesized by coprecipitation, given that it is observable in the XRD spectra, while Sn percentage obtained from EDX analysis of sample P1+I-Cu₂O-SnO₂-4 is 0.33%. This higher potential could be due to SnO₂, since it absorbs in the UV range and that the conductivity of SnO₂ is lower than Cu₂O [44,45].

4.2 Comparison of test results by chemical species

In this paragraph, the test results will be shown, comparing the samples according to the chemical species. In particular, the results of the sample P1-Cu₂O-0.02-6-1.8-600 will be compared with those of CP-Cu₂O-pH7-0.6-1-0.3, the results of the sample P1+I-Cu₂O-SnO₂-4 with those of the CP-Cu₂O-SnO₂-pH7 and the results of the sample P1-Cu₂O-0.02-6-1.8-300-Et0 with those of the P1-Cu₂O-0.02-6-1.8-300-Et3.

4.2.1 Comparison between CP-Cu₂O-pH7-0.6-1-0.3 and P1-Cu₂O-0.02-6-1.8-600

Figure 4.2.1.1 shows cyclic voltammetries in N₂ and CO₂, while Figure 4.2.1.2 presents liner sweep voltammetries in N₂ and CO₂.

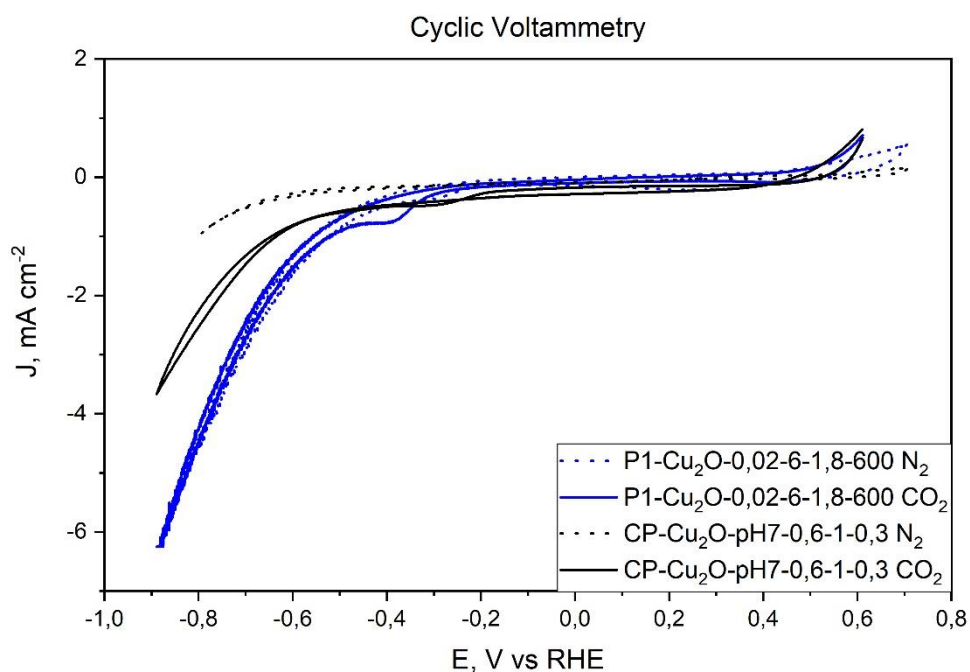


Figure 4.2.1.1 Cyclic voltammetries in N₂ and CO₂ of samples CP-Cu₂O-pH7-0.6-1-0.3 and P1-Cu₂O-0.02-6-1.8-600.

Observing the CVs, it can be seen that the curves for both samples did not have an extended internal area, since the samples under consideration are without SnO₂. Furthermore, there are CO₂ reduction peaks at -0.39 V vs. RHE for P1-Cu₂O-0.02-6-1.8-600 and -0.3 V vs. RHE for CP-Cu₂O-pH7-0.6-1-0.3, due to the absence of tin (IV) oxide.

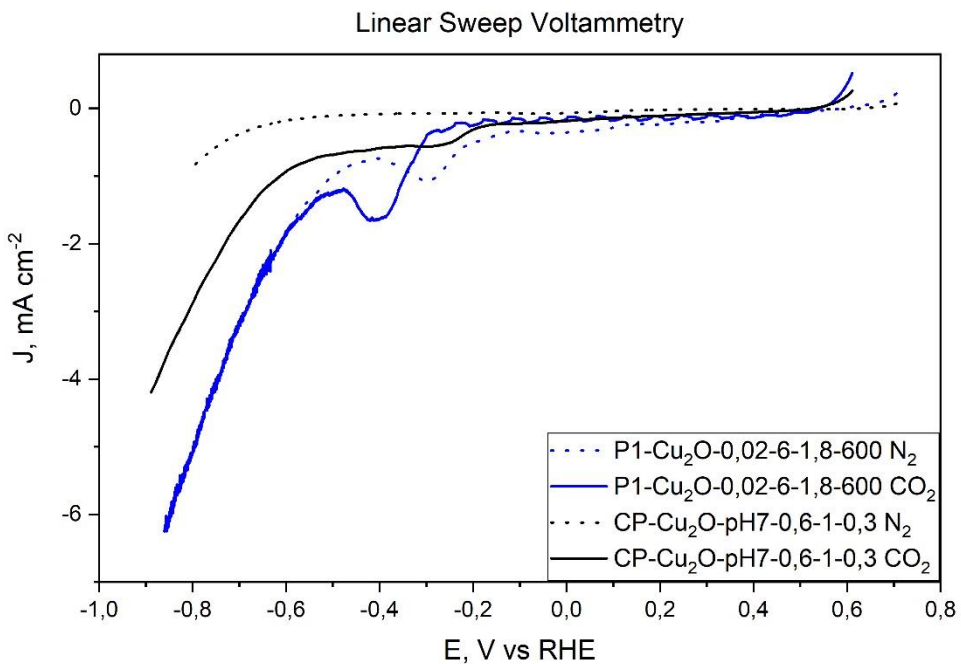


Figure 4.2.1.2: Linear sweep voltammetries in N₂ and CO₂ of samples CP-Cu₂O-pH7-0.6-1-0.3 and P1-Cu₂O-0.02-6-1.8-600.

The first difference, which catches the attention, is the fact that only the sample P1-Cu₂O-0.02-6-1.8-600 presents photo-activity with significant and observable contribute from the LSVs. Furthermore, the current densities (J) assume higher decisively values in modulus for the sample synthesized by precipitation. Table 4.2.1.1 shows the on-set potential values of both samples in N₂ and CO₂.

Table 4.2.1.1: on-set potential values of CP-Cu₂O-pH7-0.6-1-0.3 and P1-Cu₂O-0.02-6-1.8-600 in N₂ and CO₂.

Sample	On-set potential (V)	
	N ₂	CO ₂
CP-Cu ₂ O-pH7-0.6-1-0.3	-0.656	-0.620
P1-Cu ₂ O-0.02-6-1.8-600	-0.533	-0.530

Comparing the values of on-set potentials, the values of P1-Cu₂O-0.02-6-1.8-600 are decidedly lower in modulus than CP-Cu₂O-pH7-0.6-1-0.3, highlighting another positive aspect of the sample synthesized by precipitation.

Instead Figures 4.2.1.3 and 4.2.1.4 show the chronoamperometries in CO₂ at -100mV and -250 mV, respectively. Table 4.2.1.2 shows light faradic gain for both samples in CA at -100 mV and at -250 mV. Finally, Figure 4.2.1.5 shows a linear sweep voltammetry post CA in CO₂ at -250 mV, while figure 4.2.1.6 shows a chronopotentiometry in CO₂ at -1 mA.

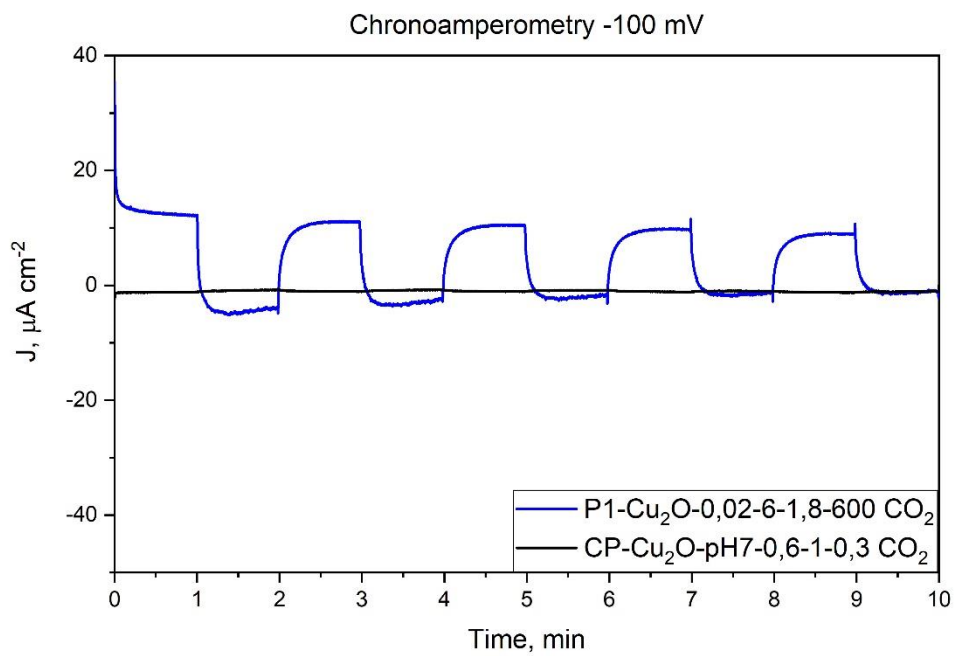


Figure 4.2.1.3: Chronoamperomtries in CO₂ of samples CP-Cu₂O-pH7-0.6-1-0.3 and P1-Cu₂O-0.02-6-1.8-600 at -100 mV.

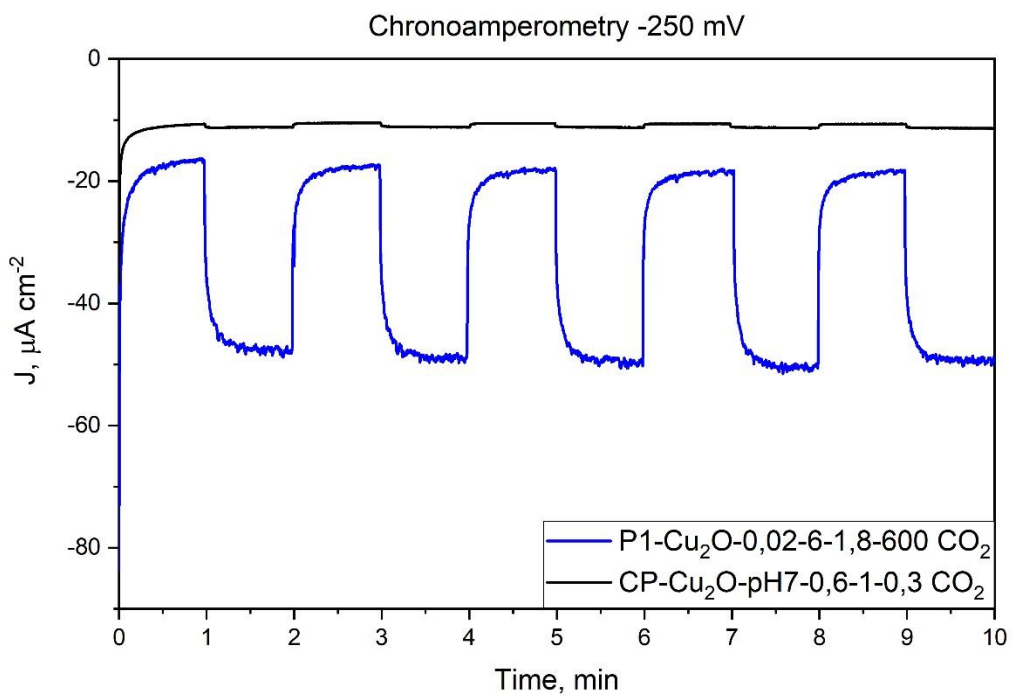


Figure 4.2.1.4: Chronoamperomtries in CO₂ of samples CP-Cu₂O-pH7-0.6-1-0.3 and P1-Cu₂O-0.02-6-1.8-600 at -250 mV.

Table 4.2.1.2: Light faradic gain on average for samples CP-Cu₂O-pH7-0.6-1-0.3 and P1-Cu₂O-0.02-6-1.8-600 in CA at -100mV and at -250 mV.

Sample	Light Faradic Gain ($\mu\text{A cm}^{-2}$)	
	CA -100 mV	CA -250 mV
CP-Cu ₂ O-pH7-0.6-1-0.3	-0.2662	-0.65
P1-Cu ₂ O-0.02-6-1.8-600	-13.1	-30.7

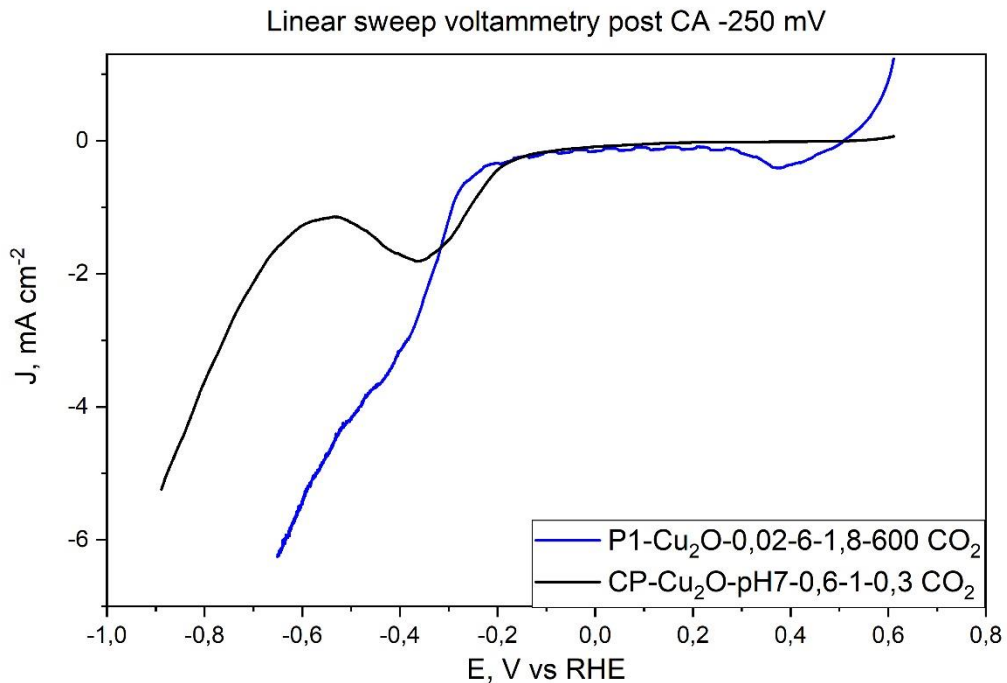


Figure 4.2.1.5: Linear sweep voltammetries in CO₂ post CA at -250 mV of samples CP-Cu₂O-pH7-0.6-1-0.3 and P1-Cu₂O-0.02-6-1.8-600 .

As can be seen from the post CA -250 mV LSV curves, sample P1-Cu₂O-0.02-6-1.8-600 still has photo-activity, while the CP-Cu₂O-pH7-0.6-1-0.3 does not show this property. P1-Cu₂O-0.02-6-1.8-600 has a 0.37 V reduction peak, a value very close to the reduction potential of Cu²⁺ at Cu (0.340 V). This could be due to the fact that Cu₂O could be self-oxidized during water reduction, given that H₂ FE is about 88%, as reported by Kakuta and Abe [18]. Moreover, works in the literature show how Cu₂O can oxidize to CuO under illumination [17]. Therefore, also the illumination could be the cause of this hypothetical oxidation.

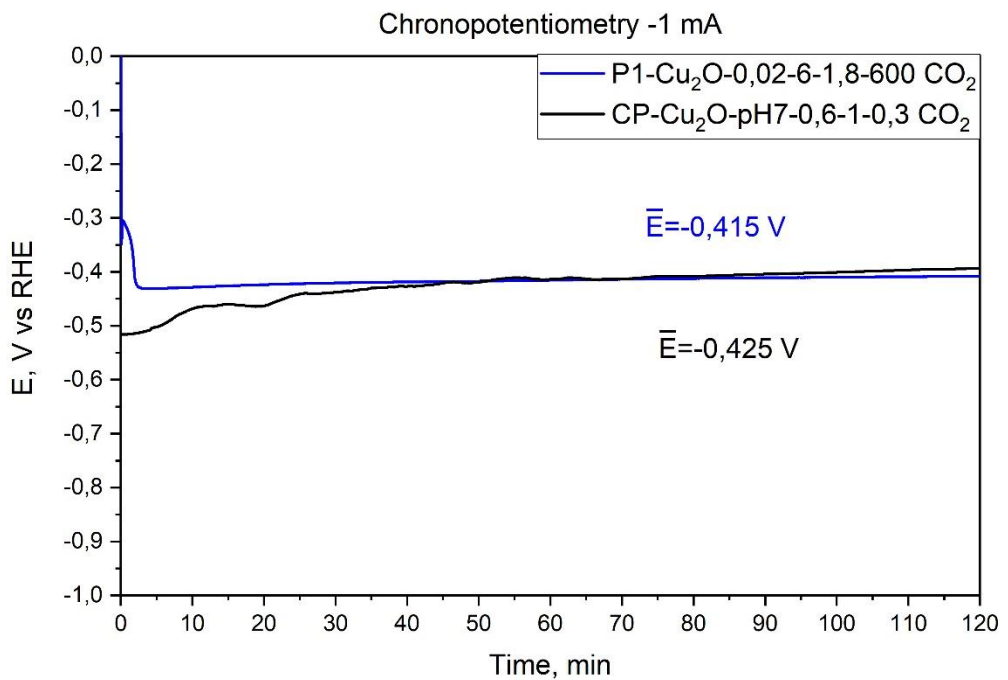


Figure 4.2.1.6: Chronopotentiometries in CO₂ at -1 mA of samples CP-Cu₂O-pH7-0.6-1-0.3 and P1-Cu₂O-0.02-6-1.8-600.

4.2.2 Comparison between CP-Cu₂O-SnO₂-pH7 and P1+I-Cu₂O-SnO₂-4

Figure 4.2.2.1 shows cyclic voltammetries in N₂ and CO₂, while Figure 4.2.2.2 presents linear sweep voltammetries in N₂ and CO₂. Instead Figures 4.2.2.3 and 4.2.2.4 show the chronoamperometries in CO₂ at -100 mV and -250 mV respectively. Table 4.2.2.1 shows light faradic gain for both samples in CA at -100 mV and at -250 mV. Finally, Figure 4.2.2.5 shows a linear sweep voltammetry post CA in CO₂ at -250 mV, while figure 4.2.2.6 shows a chronopotentiometry in CO₂ at -1 mA.

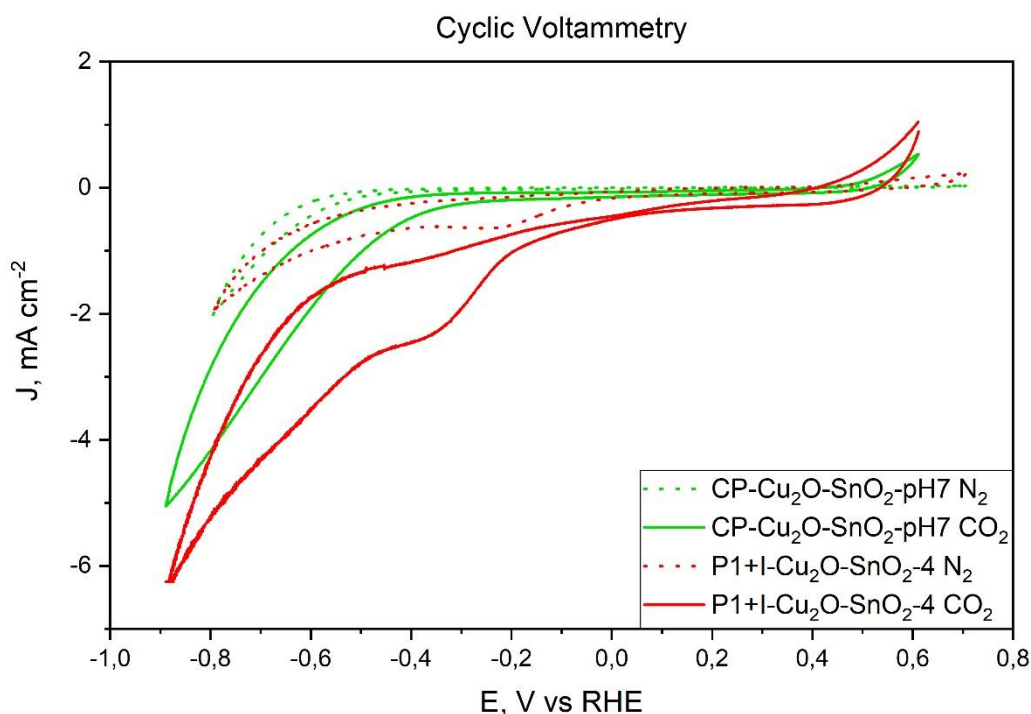


Figure 4.2.2.1 Cyclic voltammetries in N₂ and CO₂ of samples qui-SnO₂-4.

Both samples have an extended area inside the CVs, due to the presence of SnO₂, greater for the sample P1+I-Cu₂O-SnO₂-4. moreover, the current densities of this last sample are decidedly higher in modulus.

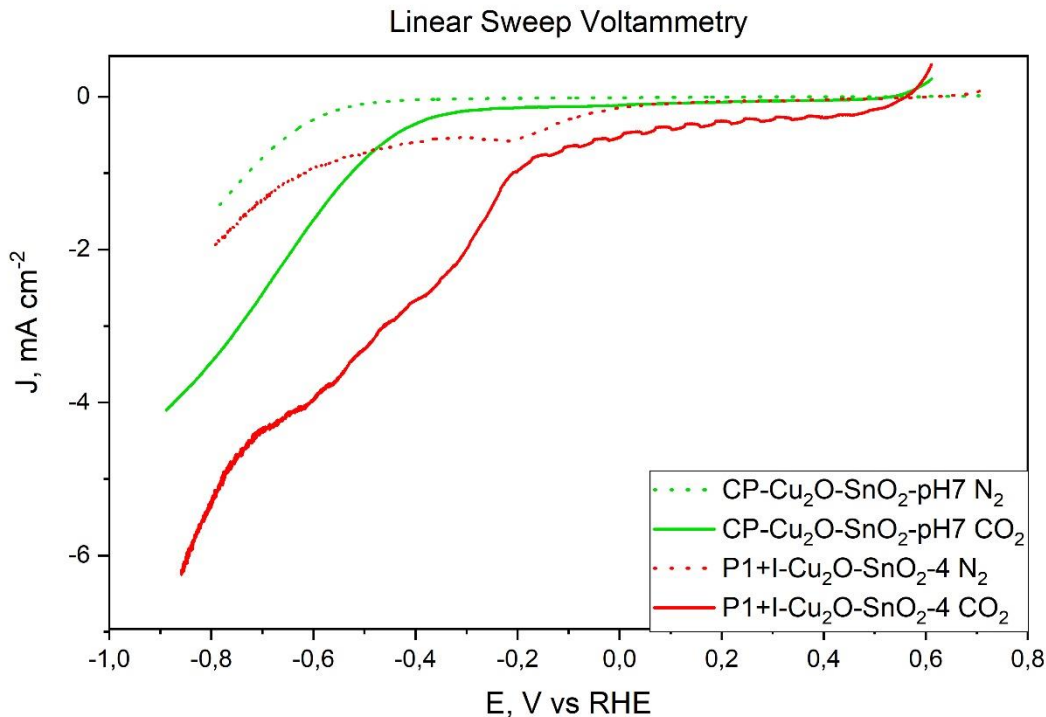


Figure 4.2.2.2: Linear sweep voltammetries in N₂ and CO₂ of samples CP-Cu₂O-SnO₂-pH7 and P1+I-Cu₂O-SnO₂-4.

Sample P1+I-Cu₂O-SnO₂-4 has higher photo-activity and higher density of currents in modulus than the sample CP-Cu₂O-SnO₂-pH7. However, the sample synthesized via precipitation and impregnation exhibits a reduction peak in N₂ at -0.25 V, not present in the other sample. Table 4.2.2.1 shows the on-set potential values of both samples in N₂ and CO₂.

Table 4.2.2.1: On-set potential values of CP-Cu₂O-pH7-0.6-1-0.3 and CP-Cu₂O-SnO₂-pH7 in N₂ and CO₂.

Sample	On-set potential (V)	
	N ₂	CO ₂
CP-Cu ₂ O-SnO ₂ -pH7	-0.578	-0.444
P1+I-Cu ₂ O-SnO ₂ -4	-0.532	-0.458

Instead, Figures 4.2.2.3 and 4.2.2.4 show the chronoamperometries in CO₂ at -100 mV and -250 mV, respectively. Table 4.2.2.1 shows light faradic gain for both samples in CA at -100 mV and at -250 mV. Finally, Figure 4.2.2.5 shows a linear sweep voltammetry post CA in CO₂ at -250 mV, while figure 4.2.2.6 shows a chronopotentiometry in CO₂ at -1 mA.

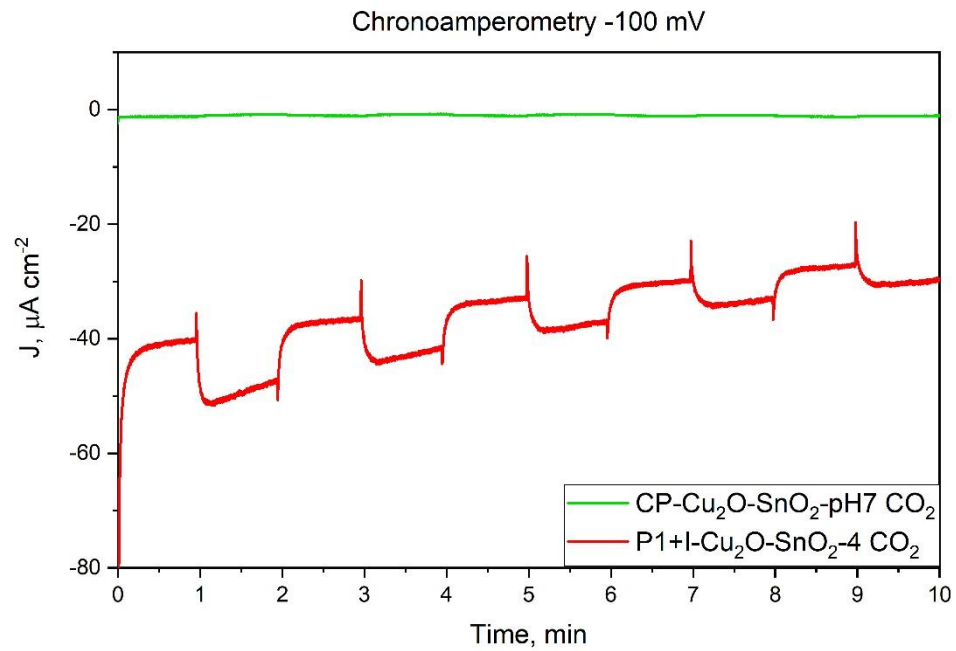


Figure 4.2.2.3: Chronoamperomtries in CO₂ of samples CP-Cu₂O-SnO₂-pH7 and P1+I-Cu₂O-SnO₂-4 at -100 mV.

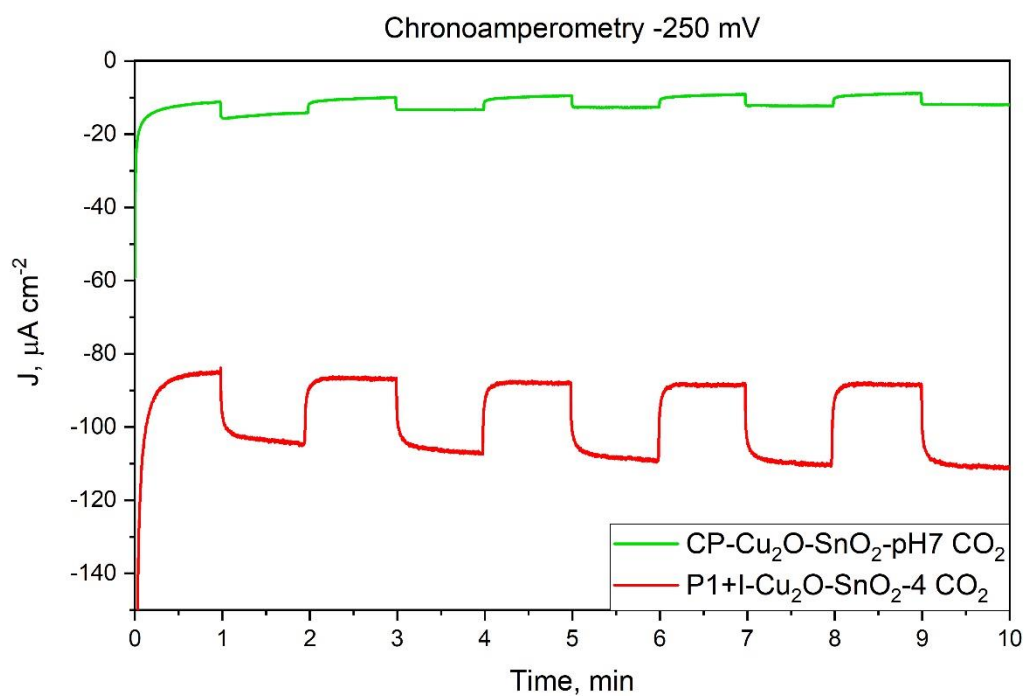


Figure 4.2.2.4: Chronoamperomtries in CO₂ of samples CP-Cu₂O-SnO₂-pH7 and P1+I-Cu₂O-SnO₂-4 at -250 mV

Table 4.2.2.2: Light faradic gain on average for samples CP-Cu₂O-pH7-0.6-1-0.3 and P1-Cu₂O-0.02-6-1.8-600 in CA at -100mV and at -250 mV.

Sample	Light Faradic Gain ($\mu\text{A cm}^{-2}$)	
	CA -100 mV	CA -250 mV
CP-Cu ₂ O-SnO ₂ -pH7	-0.2587	-2.80
P1+I-Cu ₂ O-SnO ₂ -4	-5.2	-20.3

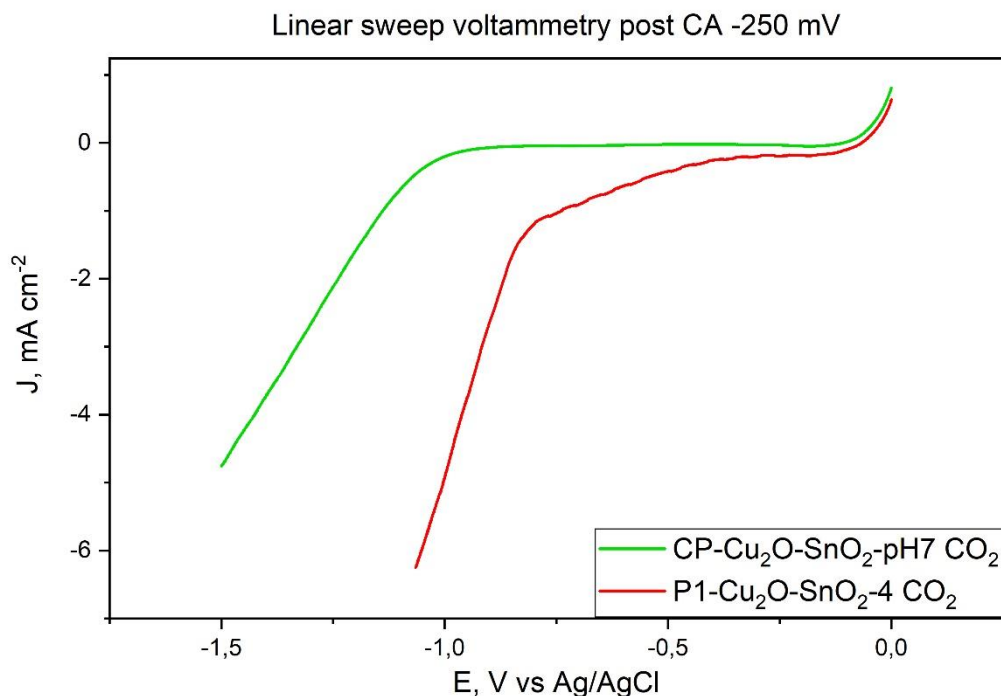


Figure 4.2.2.5: Linear sweep voltammetries in CO₂ post CA at -250 mV of samples CP-Cu₂O-SnO₂-pH7 and P1+I-Cu₂O-SnO₂-4.

As can be seen from the post CA -250 mV LSV curves, sample P1+I-Cu₂O-SnO₂-4 still had photo-activity, while the CP-Cu₂O-SnO₂-pH7 did not show this property. In the both samples, in which tin is also present in the atomic composition, reduction peaks did not occur, probably due to greater stability conferred by the presence of SnO₂. This hypothesis can be justified by the fact that in CP-Cu₂O-SnO₂-pH7 samples, in which tin (IV) oxide is observable from XRD analyzes, there are no reduction peaks in both CVs and LSVs.

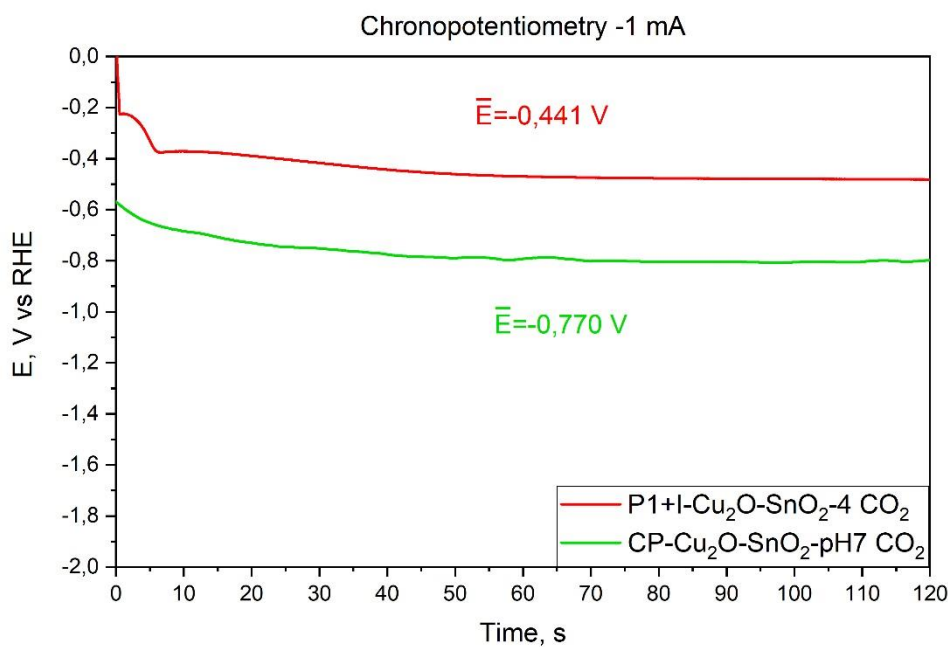


Figure 4.2.2.6: Chronopotentiometries in CO₂ at -1 mA of samples CP-Cu₂O-SnO₂-pH7 and P1+I-Cu₂O-SnO₂-4.

Both samples have a decreasing trend, probably due to the presence of SnO₂. Furthermore, the gap between the values is large and may be due to the greater amount of SnO₂ in the CP-Cu₂O-SnO₂-pH7.

4.2.3 Comparison between P1-Cu₂O-0.02-6-1.8-300-Et0 and P1-Cu₂O-0.02-6-1.8-300-Et3

Figure 4.2.3.1 shows cyclic voltammetries in N₂ and CO₂ while Figure 4.2.3.2 and Figure 4.2.3.3 show a linear sweep voltammetry in CO₂ and chronoamperometry at -1600 mV in CO₂ respectively.

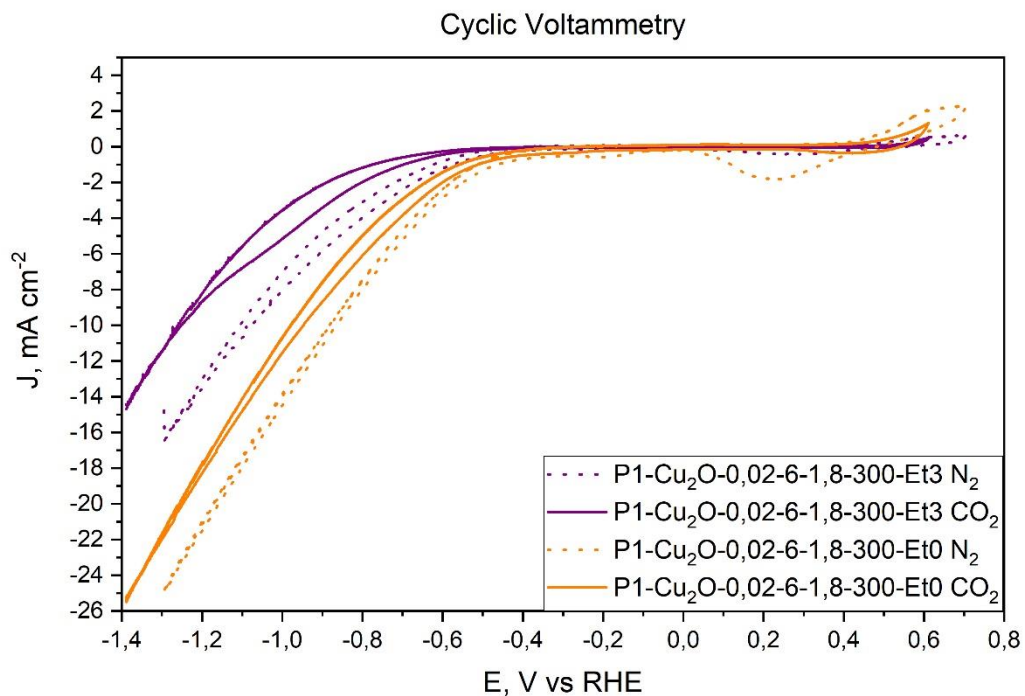


Figure 4.2.3.1 Cyclic voltammetries in N₂ and CO₂ of samples P1-Cu₂O-0.02-6-1.8-300-Et0 and P1-Cu₂O-0.02-6-1.8-300-Et3.

CVs in N₂ show reduction peaks at about 0.23 V vs. RHE for both samples but more markedly for P1-Cu₂O-0.02-6-1.8-300-Et0 sample, while CVs in CO₂ did not show reduction peaks, since the reduction has already occurred in N₂. Table 4.2.3.1 shows the on-set potential values of both samples in N₂ and CO₂.

Table 4.2.3.1: On-set potential values of P1-Cu₂O-0.02-6-1.8-300-Et0 and P1-Cu₂O-0.02-6-1.8-300-Et3 in N₂ and CO₂.

Sample	On-set potential (V)	
	N ₂	CO ₂
P1-Cu ₂ O-0.02-6-1.8-300-Et0	-0.703	-0.638
P1-Cu ₂ O-0.02-6-1.8-300-Et3	-0.945	-0.812

Compared to PEC samples, the lowest on-set potential values in modulus are those in N₂. Comparing the two samples, sample P1-Cu₂O-0.02-6-1.8-300-Et0 shows an on-set potential value in CO₂ equal to -0.703 V vs RHE, while the P1-Cu₂O-0.02-6-1.8-600-Et3 a value of -0.945 V vs RHE. This could be due to the lower quantity of metallic Cu in the sample P1-Cu₂O-0.02-6-1.8-30-Et0.

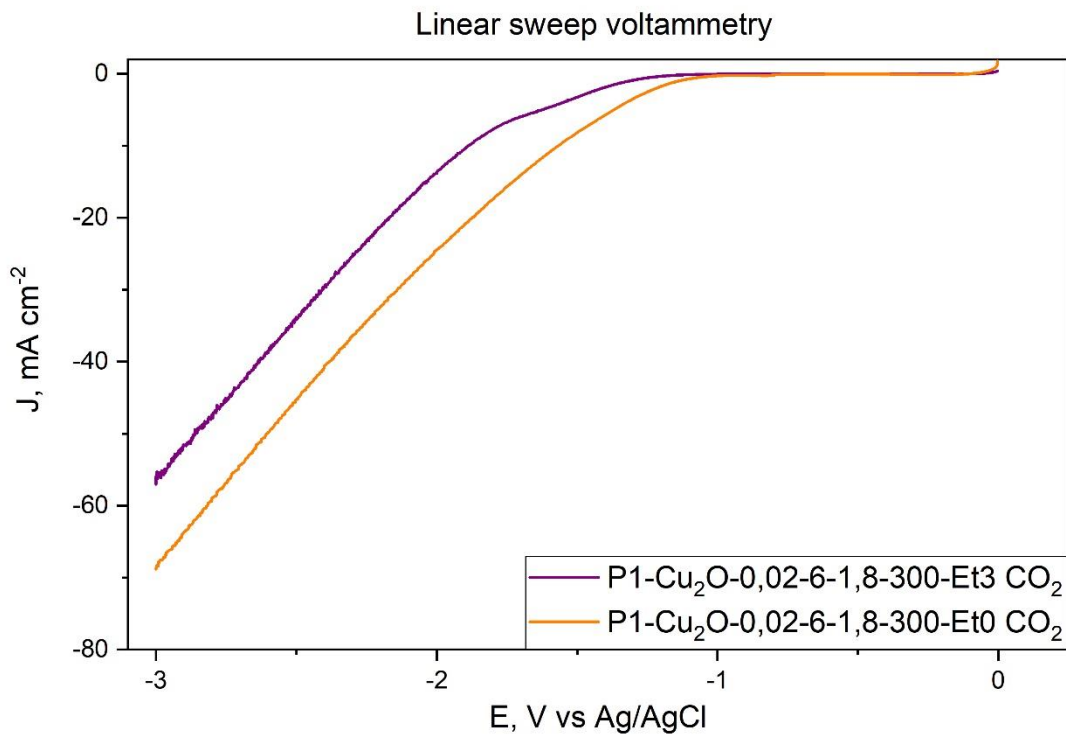


Figure 4.2.3.2 Linear sweep voltammetries in CO₂ of samples P1-Cu₂O-0.02-6-1.8-300-Et0 and P1-Cu₂O-0.02-6-1.8-300-Et3.

LSVs show no reduction peaks and the onset potentials values are -1.06 V for P1-Cu₂O-0.02-6-1.8-300-Et3 and -0.90 V for P1-Cu₂O-0.02-6-1.8-300-Et0 in CO₂. The value is higher for the P1-Cu₂O-0.02-6-1.8-300-Et3 sample as the quantity of metallic Cu is probably greater than for the other sample. This can be evaluated through the ratio of the XRD peaks of maximum intensity of Cu and Cu₂O, defined as the maximum intensity of Cu divided by that of Cu₂O. these values are 0.046 for P1-Cu₂O-0.02-6-1.8-300-Et0 and 0.618 for P1-Cu₂O-0.02-6-1.8-300-Et3. Furthermore, the current densities of these samples are the highest of all the synthesized samples, probably due to the presence of metallic Cu.

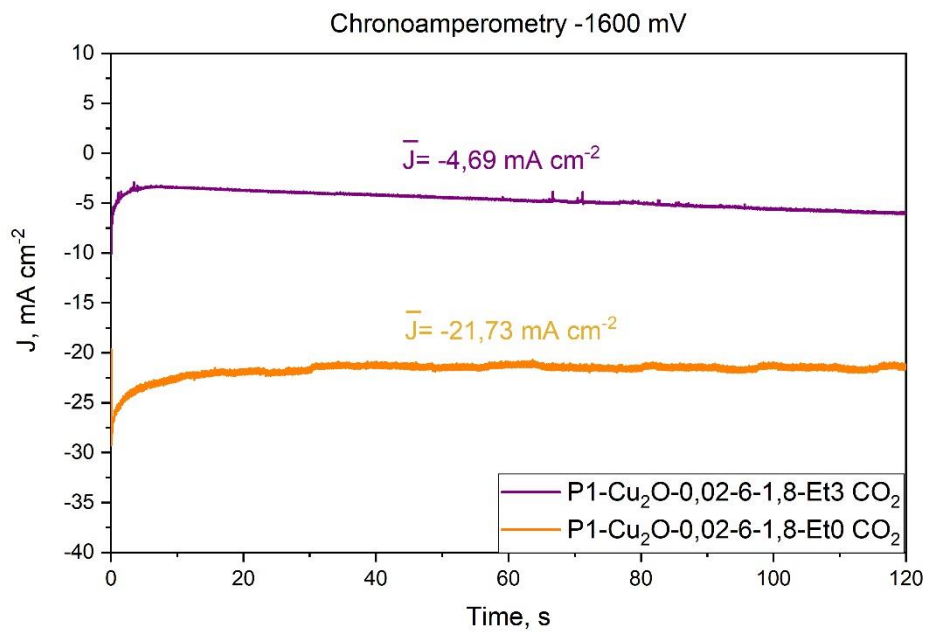


Figure 4.2.3.3 Chronoamperometry at -1600mV in CO₂ of samples P1-Cu₂O-0.02-6-1.8-300-Et0 and P1-Cu₂O-0.02-6-1.8-300-Et3.

4.3 Comparison of Light Faradic Gain of PEC samples

In the PEC test samples, it is possible to calculate the light faradic gain and observe how it varies over time. Table 4.3.1 shows on average light faradic gain of PEC test samples. Figure 4.3.1 and Figure 4.3.2 present light faradic gain trends over time in the CA at -100 mV and at -250 mV respectively.

Table 4.3.1: Light faradic gains on average of PEC test samples

Sample	Light Faradic Gain ($\mu\text{A cm}^{-2}$)	
	CA -100 mV	CA -250 mV
CP-Cu ₂ O-SnO ₂ -pH7	-0.2587	-2.80
CP-Cu ₂ O-pH7-0.6-1-0.3	-0.2662	-0.65
P1+I-Cu ₂ O-SnO ₂ -4	-5.2	-20.3
P1-Cu ₂ O-0.02-6-1.8-600	-13.1	-30.7

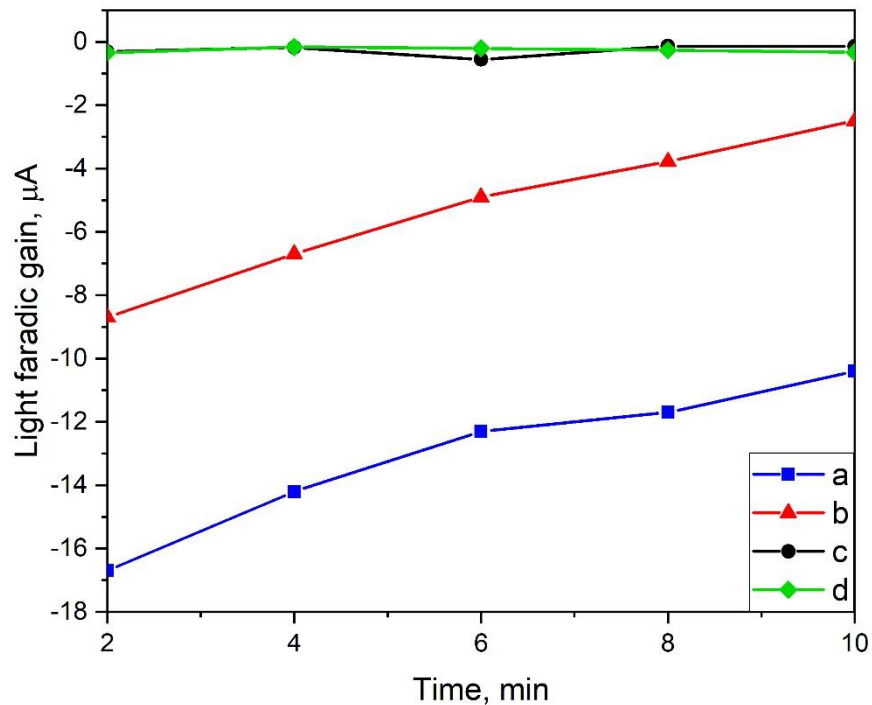


Figure 4.3.1: Light faradic gain trends over time pf samples a) P1-Cu₂O-0.02-6-1.8-600, b) P1+I-Cu₂O-SnO₂-4, c) CP-Cu₂O-pH7-0.6-1-0.3 and d) CP-Cu₂O-SnO₂-pH7 in the CA at -100 mV.

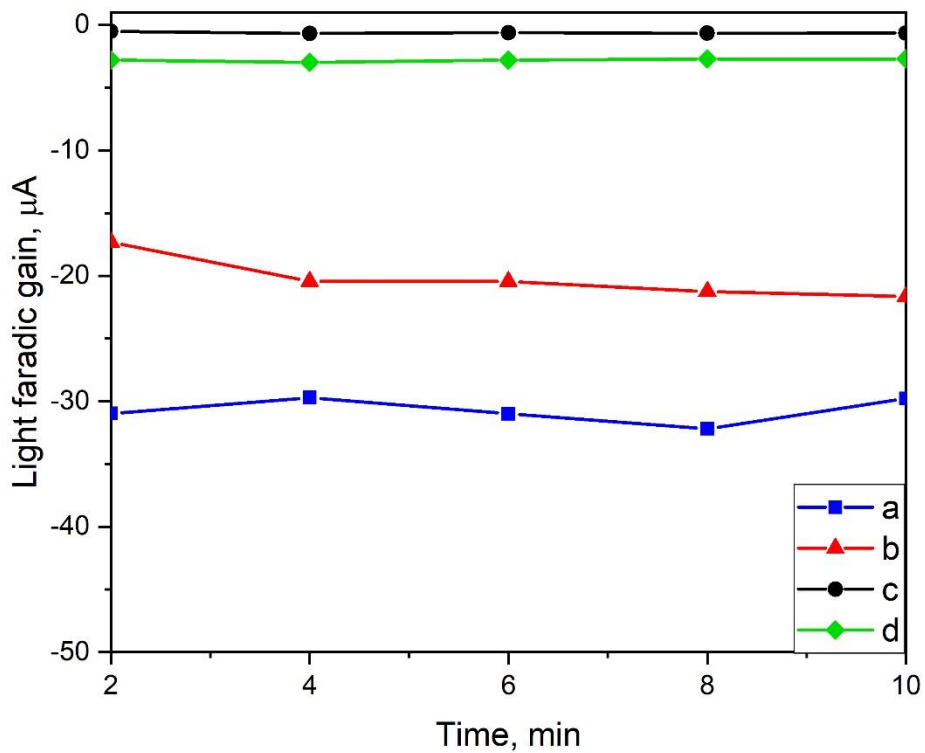


Figure 4.3.2: Light faradic gain trends over time pf samples a) P1-Cu₂O-0.02-6-1.8-600, b) P1+I-Cu₂O-SnO₂-4, c) CP-Cu₂O-pH7-0.6-1-0.3 and d) CP-Cu₂O-SnO₂-pH7 in the CA at -250 mV.

From Figures 4.3.1 and 4.3.2, it can be seen that the sample P1-Cu₂O-0.02-6-1.8-600 presents the highest light faradic gains with values equal to -13.1 μA and -30.7 μA, followed by the sample P1+I-Cu₂O-SnO₂-4 with light faradic gains at -5.2 μA and -20.3 μA. Much lower values are those of the samples synthesized by the coprecipitation method. In particular the CP-Cu₂O-pH7-0.6-1-0.3 sample shows values equal to -0.2662 μA and -0.65 μA, while the CP-Cu₂O-SnO₂-pH7 sample shows light faradic gain values equal to at -0.2587 μA and -2.80 μA. These values can be justified by reasoning about the chemical species present in the tested samples. Sample P1-Cu₂O-0.02-6-1.8-600 consists exclusively of Cu₂O, while the P1+I-Cu₂O-SnO₂-4 has a 0.33% of Sn which could have negatively influenced the light faradic gain, reducing its value. Same reasoning can be applied to CP-Cu₂O-SnO₂-pH7 in which SnO₂ is present in greater quantities than P1+I-Cu₂O-SnO₂-4, being observable from XRD analysis. On the other hand, for sample CP-Cu₂O-pH7-0.6-1-0.3 the presence of metallic Cu could be the cause of low values of light faradic gain, since the metallic Cu is not photo-active. Observing the light faradic gain trends, it can be observed that the curves at -250 mV vary less than those at -100 mV, in particular for P1-Cu₂O-0.02-6-1.8-600 and P1+I-Cu₂O-SnO₂-4 samples. Probably this is due to the fact that, by applying a greater potential, the material is more active and, consequently, more stable in exploiting the light contribution.

4.4 Comparison of Faradic Efficiencies

Table 4.4.1 and Table 4.4.2 show faradic efficiencies (FE) of PEC test samples and RDE test samples respectively.

Table 4.4.1: Faradic Efficiencies of PEC test samples.

Products	Faradic Efficiency (%)			
	P1-Cu ₂ O-0.02-6-1.8-600	P1+I-Cu ₂ O-SnO ₂ -4	CP-Cu ₂ O-pH7-0.6-1-0.3	CP-Cu ₂ O-SnO ₂ -pH7
H ₂	88.67	45.93	43.49	75.89
CO	0.70	3.89	0.06	0.008
Formate	4.62	10.27	4.28	5.73
MeOH	0	0.8	0.20	0.19
EtOH	2.38	0	8.91	0
2-propanol	0.61	0.47	0.073	0.20

Table 4.3.2: Faradic Efficiencies of RDE test samples.

Products	Faradic Efficiency (%)	
	P1-Cu ₂ O-0.02-6-1.8-300-Et0	P1-Cu ₂ O-0.02-6-1.8-300-Et3
H ₂	30.14	71.48
CO	13.81	10.69
Formate	25.50	19.16
MeOH	0.04	0.66
EtOH	0.073	0
2-propanol	0	0

Figure 4.4.3 and Figure 4.4.4 show faradic efficiencies of PEC test samples and RDE test samples respectively.

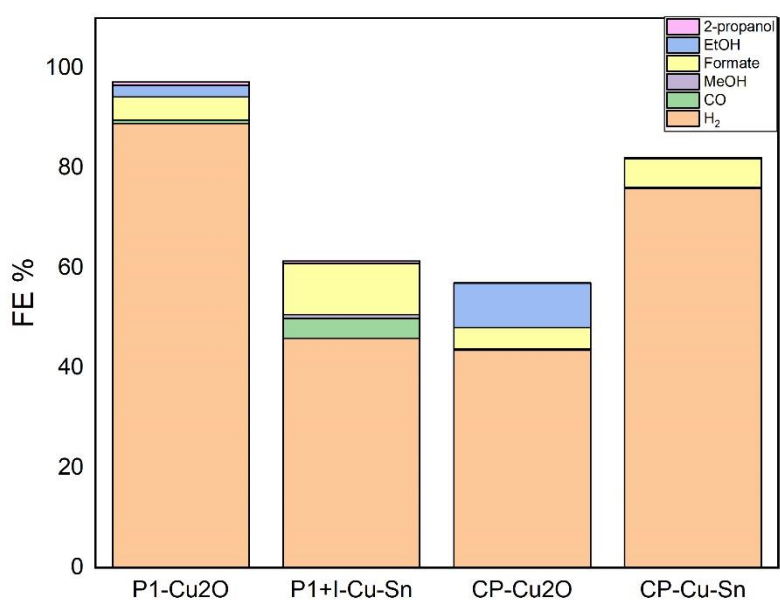


Figure 4.4.3: Faradic efficiencies of PEC test samples.

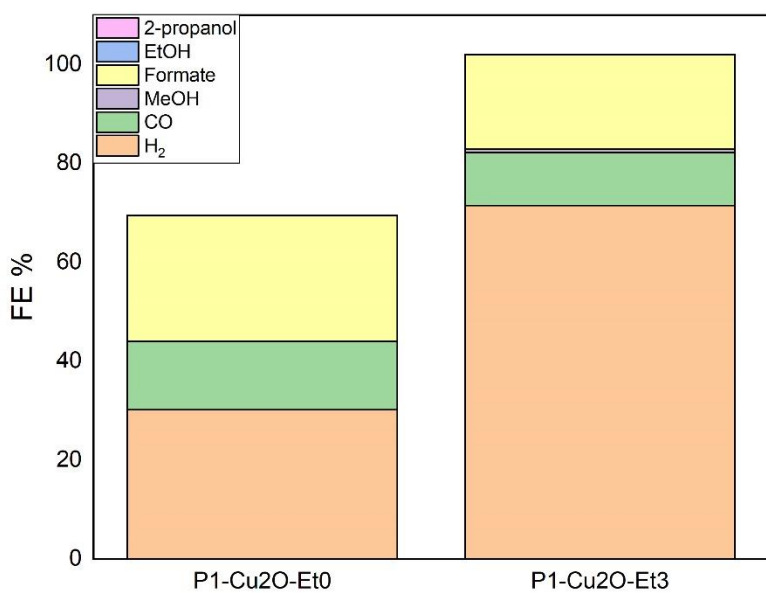


Figure 4.4.4: Faradic efficiencies of RDE test samples.

As regards the faradic efficiencies of the PEC test samples, the samples with Sn have higher HCOOH FE than the corresponding tin-free samples. In particular, P1+I-Cu₂O-SnO₂-4 has a faradic formate efficiency of 10.27%, while P1-Cu₂O-0.02-6-1.8-600 shows a value of 4.62%, approximately 2 times lower. On the other hand, for the sample CP-Cu₂O-SnO₂-pH7 the HCOOH FE is 5.73%, slightly higher than that of CP-Cu₂O-pH7-0.6-1-0.3 by about 4.28%. This increase in FE of formate is due to the presence of tin (IV) oxide, which is a good catalyst for the electrochemical reduction of CO₂ to formate [41,42]. Observing the FE of CO, only the P1+I-Cu₂O-SnO₂-4 shows a value higher than the unit and equal to 3.89%. Moreover, it is interesting to observe how the CP-Cu₂O-pH7-0.6-1-0.3 sample shows a fair FE towards ethanol of about 8.91 %.

From the RDE tests, the samples show good CO and HCOOH FE with values equal to 13.81% and 25.50% for the P1-Cu₂O-0.02-6-1.8-300-Et0 and 10.69% and 19.16% for the P1-Cu₂O-0.02-6-1.8-300-Et3, respectively. Observing the FE of hydrogen, it can be seen that sample P1-Cu₂O-0.02-6-1.8-300-Et0 has a faradic efficiency of 30.14%, while P1-Cu₂O-0.02-6-1.8-300-Et3 71.48%. This could be justified by looking at the XRD spectra of the two samples. P1-Cu₂O-0.02-6-1.8-300-Et0 shows an intensity ratio between the maximum peaks of Cu₂O and that of metallic Cu equal to 0.046, while this ratio is 0.618 for P1-Cu₂O-0.02-6-1.8-300-Et3. This suggests that in the sample P1-Cu₂O-0.02-6-1.8-300-Et3 there is a higher percentage of metallic Cu than in P1-Cu₂O-0.02-6-1.8-300-Et0. Since the metallic Cu is much more conductive than Cu₂O it could have favored the water splitting reaction, thus determining a higher H₂ FE in the sample P1-Cu₂O-0.02-6-1.8-300-Et3. Extremely low or zero are the FEs of methanol, ethanol and 2-propanol for both samples.

5 Conclusions

This work aimed to study possible methods of Cu₂O synthesis and use them to develop Cu-Sn based catalysts for photo-electrochemical conversion of CO₂. The samples were synthesized, characterized and their catalytic activity was evaluated in the RDE and PEC systems.

For the coprecipitation method, the optimal pH, at which the reagent solution must be maintained, was found to be at value 7. The XRD spectra of the samples synthesized at this pH show only the peaks of Cu₂O and SnO₂, while BET analysis have a greater porosity and area surface equal to 134 ± 7.15 m²/g, higher than the other samples synthesized at different pH. Moreover, also the energy bandgap value confirms the pH7 as the best value. Its value is around 2.51 ± 0.02 eV, a much lower value than the other syntheses with acidic or basic pH, where the value ranges between 4.25 eV and 4.4 eV. Table 3.1.3.1 shows the percentage variation coefficients of the repetitions made at pH 7 and it can be said that the synthesis at pH 7 has good replicability. PEC tests were conducted on the samples at pH7. Observing the curves of the cyclic voltammetries and linear sweep voltammetries, reduction peaks are not present, thus highlighting the high stability of the sample during the test. The faradic efficiencies obtained show 75.89% for H₂, 5.73% for formic acid, while the other FEs are lower than the unit value. A hypothesis of these low FE values may be the fact that tests have a rather long protocol, useful for characterization, but which alters the catalyst, in particular the oxidation state of Cu₂O, making it gradually less active in reducing CO₂.

For the precipitation-impregnation two-steps strategy, the Cu₂O yield went from 86% for P1-Cu₂O-0.01-2-0.6-300 to about 99% for P1-Cu₂O-0.02-6-1.8-600, going to increase the molarity of the CuCl₂ solution by 100%, the molarity of the NaOH and C₆H₈O₆ solutions by 200% and using a double volume. On the other hand, from the synthesis of Cu₂O with the addition of an etching acid step, obtained samples presented metallic Cu together with Cu₂O. This was not the desired result, but such materials can be interesting starting points for obtaining mixed Cu / Cu₂O catalysts for the electrochemical conversion of CO₂ to alcohols. Furthermore, the XRD spectra of all synthesized copper (I) oxide samples showed characteristics typical of the octahedral crystalline form, such as the maximum intensity peak at 36.5 and the intensity ratio between the peaks {220} and {200} in the range of 0.6 to 0.7, which means that by modifying the concentrations and volumes of the reagents it was possible to have a probable variation of the crystalline structure. P1-Cu₂O-0.02-6-1.8-600 and P1+I-Cu₂O-SnO₂-4 samples were tested in PEC tests, while P1-Cu₂O-0.02-6-1.8-300-Et0 and P1-Cu₂O-0.02-6-1.8-300-Et3 samples were tested in RDE tests. Comparing the faradic efficiencies of the PEC test samples just mentioned, P1+I-Cu₂O-SnO₂-4 shows FE of CO and HCOOH equal to 3.89% and 10.27% respectively, higher than those of P1-Cu₂O-0.02-6-1.8-600 equal to 0.70% and 4.62%. Interesting is the faradic efficiency of H₂ of these two samples, which is around 45.93% for P1+I-Cu₂O-SnO₂-4 and 88.67% for P1-Cu₂O-0.02-6-1.8-600. Probably, P1+I-Cu₂O-SnO₂-4 tends more to favor the CO₂ photo-electrochemical conversion reactions to those of water splitting compared to P1-Cu₂O-0.02-6-1.8-600, given that the total faradic efficiency of the products containing carbon is about 15.43% for P1+I-Cu₂O-SnO₂-4 and 8.31 for P1-Cu₂O-0.02-6-1.8-600, almost 2 times lower. For the samples tested at RDE, the faradic efficiencies related to CO and HCOOH are the highest than all tested samples with values equal to 13.81% and 25.50 for P1-Cu₂O-0.02-6-1.8-300-Et0 and 10.69% and 19.16% for P1-Cu₂O-0.02-6-1.8-300-Et3. Instead, H₂ FE are around 30.14% for P1-Cu₂O-0.02-6-1.8-300-Et0 and 71.48% for P1-Cu₂O-0.02-6-1.8-300-Et3.

As regards the gain in photo-current, the sample with the highest light faradic gain is the sample P1-Cu₂O-0.02-6-1.8-600 with values of -13.1 μA and -30.7 μA, followed by P1+I-Cu₂O-SnO₂-4 with -5.2 μA and -20.3 μA in CA at -100 mV and at -250 mV respectively. On the other hand, the worst sample is CP-Cu₂O-pH7-0.6-1-0.3 with light faradic gain values lower than unity in CA at -100 mV than in CA at -250 mV.

This work paves the way for many ideas on the optimization of these catalysts. it would be very interesting to realize the catalyst P1+I-Cu₂O-SnO₂ with rhombic dodecahedral Cu₂O, in order to obtain useful information on the optimal crystalline structure. Another possible synthesis is that which aims to obtain a dodecahetric rhombic crystal structure using C₆H₈O₆ and HCl, added simultaneously with two separate solutions, in order to replace the NH₂OH * HCl.

References

1. Joel Y. Y. Loh , Nazir P. Kherani and Geoffrey A. Ozin, *Persistent CO₂ photocatalysis for solar fuels in the dark*, Nature Sustainability, 2021, 4, 466–473.
2. Corinne Le Quéré, Glen P. Peters, Pierre Friedlingstein, Robbie M. Andrew, Josep G. Canadell, Steven J. Davis, Robert B. Jackson and Matthew W. Jones, *Fossil CO₂ emissions in the post-COVID-19 era*, Nature Climate Change, 2021, 11, 197–199.
3. Nico Wunderling, Matteo Willeit, Jonathan F. Dongesand Ricarda Winkelmann, *Global warming due to loss of large ice masses and Arctic summer sea ice*, Nature Communication, 2021, 11, 5177-5185
4. David E. H. J. Gernaat, Harmen Sytze de Boer, Vassilis Daioglou, Seleshi G. Yalew, Christoph Müller and Detlef P. van Vuuren, *Climate change impacts on renewable energy supply*, Nature Climate Change, 2021, 11, 119–125
5. Xin Li, Jiaguo Yu, Mietek Jaroniec and Xiaobo Chen, *Cocatalysts for Selective Photoreduction of CO₂ into Solar Fuels*, Chem. Rev. 2019, 119, 3962–4179.
6. Sheng-Nian Zhang, Meng Li , Bin Hua, Nanqi Duan, Shaochen Ding, Steven Bergens, Karthik Shankar and Jing-Li Luo, *A Rational Design of Cu₂O SnO₂ Core-Shell Catalyst for Highly Selective CO₂-to-CO Conversion*, ChemCatChem 2019, 11, 4147–4153.
7. Qing Li, Jiaju Fu, Wenlei Zhu, Zhengzheng Chen, Bo Shen, Liheng Wu, Zheng Xi, Tanyuan Wang, Gang Lu, Jun-jie Zhu and Shouheng Sun, *Tuning Sn-Catalysis for Electrochemical Reduction of CO₂ to CO via the Core/Shell Cu/SnO₂ Structure*, J. Am. Chem. Soc. 2017, 139, 4290–4293.
8. S. Benammara , A. Boudjemaab , G. Nezzala , S. Gómez-Ruizc , D. Meziane , K. Bacharib , A. Lounisd , Neil J. Covillee, *Nanoparticles based on copper deposited on carbon spheres. Preparation, characterization and application for CO₂ photo-electrochemical reduction*, Journal of Electroanalytical Chemistry, 2018, 809, 80–87
9. Liang Li, Rui Zhang, John Vinson, Eric L. Shirley, Jeffrey P. Greeley, Jeffrey R. Guest and Maria K. Y. Chan, *Imaging Catalytic Activation of CO₂ on Cu₂O (110): A First-Principles Study*, Chem. Mater. 2018, 30, 1912–1923.
10. Hoang Long Ngo, Dinesh Kumar Mishra, Vivek Mishra, Cong Chien Truong, *Recent advances in the synthesis of heterocycles and pharmaceuticals from the photo/electrochemical fixation of carbon dioxide*, Chemical Engineering Science, 2021, 229, 116-142.
11. Yimin A. Wu, Ian McNulty , Cong Liu, Kah Chun Lau, Qi Liu, Arvydas P. Paulikas4, Cheng-Jun Sun, Zhonghou Cai, Jeffrey R. Guest, Yang Ren, Vojislav Stamenkovic, Larry A. Curtiss, Yuzi Liu and Tijana Rajh, *Facet-dependent active sites of a single Cu₂O particle photocatalyst for CO₂ reduction to methanol*, Nature Energy, 2019, 4, 957–968.
12. Wan-Chen Huang, Lian-Ming Lyu, Yu-Chen Yang and Michael H. Huang, *Synthesis of Cu₂O Nanocrystals from Cubic to Rhombic Dodecahedral Structures and Their Comparative Photocatalytic Activity*, J. Am. Chem. Soc. 2012, 134, 1261–1267.
13. Shou-Heng Liua, Jun-Sheng Lua , Ying-Chih Pub , Hsiao-Chuan Fan, *Enhanced photoreduction of CO₂ into methanol by facet-dependent Cu₂O/ reduce graphene oxide*, Journal of CO₂ Utilization, 2019, 33, 171–178.

14. Yao, K. X., Yin, X. M., Wang, T. H. and Zeng, H. C., *Synthesis, Self-Assembly, Disassembly, and Reassembly of Two Types of Cu₂O Nanocrystals Unifaceted with {001} or {110} Planes*, J. Am. Chem. Soc. 2010, 132, 6131–6144.
15. Lan, X., Zhang, J Gao, H.; Wang, T., *Morphology-controlled hydrothermal synthesis and growth mechanism of microcrystal Cu₂O*, CrystEngComm 2011, 13, 633–636.
16. Liang, X., Gao, L., Yang, S. and Sun J, *Facile synthesis and shape evolution of single crystal corpus oxide*, J. Adv. Mater. 2009, 21, 2068–2071.
17. Cui Ying Toe, Zhaoke Zheng, Hao Wu, Jason Scott, Rose Amal, and Yun Hau Ng, *Photocorrosion of Cuprous Oxide in Hydrogen Production: Rationalising Self-Oxidation or Self-Reduction*, Angew. Chem. Int. Ed. 2018, 57, 13613 –13617
18. S. Kakuta, T. Abe, *Structural Characterization of Cu₂O After the Evolution of H₂ under Visible Light Irradiation*, Electrochemical and Solid-State Letters. 2009, 12 (3), 1-3.
19. L. Huang, F. Peng, H. Yu, H. Wang, *Preparation of cuprous oxides with different sizes and their behaviors of adsorption, visible-light driven photocatalysis and photocorrosion*, Solid State Sciences. 2009, 11, 129 – 138
20. C.-M. Wang, C.-Y. Wang, J., *Photocorrosion of plasmonic enhanced Cu_xO photocatalysts*, Journal of Nanophotonics, 2014, 8, 084095
21. Z. Xi, C. Li, L. Zhang, M. Xing, J. Zhang, Int. J. Hydrogen Energy 2014, 39, 6345 – 6353
22. Manon Spalla, Emilie Planes, Lara Perrin, Muriel Matheron, Solenn Berson and Lionel Flandin, *Alternative Electron Transport Layer Based on Al-Doped ZnO and SnO₂ for Perovskite Solar Cells: Impact on Microstructure and Stability*, Appl. Energy Mater. 2019, 2, 7183–7195
23. Mousa Abuhelaiqa, Naoyuki Shibayama, Xiao-Xin Gao, Hiroyuki Kanda and Mohammad Khaja Nazeeruddin, *SnO₂/TiO₂ Electron Transporting Bilayers: A Route to Light Stable Perovskite Solar Cells*, Appl. Energy Mater. 2021, 4, 3424–3430.
24. Hilmar Guzmán, Federica Zammillo, Daniela Roldán, Camilla Galletti, Nunzio Russo and Simelys Hernández, *Investigation of Gas Diffusion Electrode Systems for the Electrochemical CO₂ Conversion*, Catalysts, 2021, 11, 482.
25. Chun-Hong Kuo and Michael H. Huang, *Fabrication of Truncated Rhombic Dodecahedral Cu₂O Nanocages and Nanoframes by Particle Aggregation and Acidic Etching*, J. Am. Chem. Soc., 2008, 130, 12815–12820.
26. Soon A., Todorova M., Delley B., Stampfl C., *Thermodynamic Stability and Structure of Copper Oxide Surfaces: A First-Principles Investigation*. Phys. Rev. B: Condens. Matter Mater. Phys. 2007, 75 (12), 1–9.
27. B.D. Cullity and S.R. Stock, *Elements of X-Ray Diffraction: Pearson New International Edition, 3rd Edition*, Pearson, London, UK.
28. Brundle, C.R., Evans, C.A., Wilson, S., *Encyclopedia of materials characterization: Surfaces, Interfaces, Thin Films*, Gulf Professional Publishing, USA, 1992.
29. Montanari, R, *Tecniche sperimentali per la caratterizzazione dei materiali dal laboratorio alla produzione*, Associazione Italiana di Metallurgia, Italy, 2005.
30. Yang Su, Hongfei Li, Hanbin Ma, John Robertson and Arokia Nathan, *Controlling Surface Termination and Facet Orientation in Cu₂O Nanoparticles for High Photocatalytic Activity: A Combined Experimental and Density Functional Theory Study*, ACS Appl. Mater. Interfaces, 2017, 9, 8100–8106.

31. Zhiyu Wang, Deyan Luan, Freddy Yin Chiang Boey and Xiong Wen (David) Lou, *Fast Formation of SnO₂ Nanoboxes with Enhanced Lithium Storage Capability*, J. Am. Chem. Soc., 2011, 133, 4738–4741.
32. Jaya Pal, Mainak Ganguly, Chanchal Mondal, Anindita Roy, Yuichi Negishi and Tarasankar Pal, *Crystal-Plane-Dependent Etching of Cuprous Oxide Nanoparticles of Varied Shapes and Their Application in Visible Light Photocatalysis*, J. Phys. Chem. C 2013, 117, 24640–24653.
33. Jing-Yi Huang, Mahesh Madasu and Michael H. Huang, *Modified Semiconductor Band Diagrams Constructed from Optical Characterization of Size-Tunable Cu₂O Cubes, Octahedra, and Rhombic Dodecahedra*, J. Phys. Chem. C 2018, 122, 13027–13033.
34. A. Farhadi, M.R. Mohammadi and M. Ghorbani, *On the assessment of photocatalytic activity and charge carrier mechanism of TiO₂@SnO₂ core-shell nanoparticles for water decontamination*, Journal of Photochemistry and Photobiology A: Chemistry, 2017, 338, 171–177.
35. Jae-Hun Kima, Ali Mirzaeib, Hyoun Woo Kimc and Sang Sub Kima, *Variation of shell thickness in ZnO-SnO₂ core-shell nanowires for optimizing sensing behaviors to CO, C₆H₆, and C₇H₈ gases*, Sensors & Actuators: B. Chemical, 2020, 302 127150–127159.
36. Anupam Nandi, Pratanu Nag, Dipankar Panda, Sukanta Dhar, Syed Minhaz Hossain, Hiranmay Saha and Sanhita Majumdar, *Outstanding Room-Temperature Hydrogen Gas Detection by Plasma-Assisted and Graphene-Functionalized Core–Shell Assembly of SnO₂ Nanoburflower*, ACS Omega 2019, 4, 11053–11065.
37. Bang-De Hong, Chien-Liang Lee, *Specific activities of rhombic dodecahedral, octahedral, and cubic Cu₂O nanocrystals as glucose oxidation catalysts*, Chemical Engineering Journal, 2020, 382, 122994–123001.
38. Jin-Yi Ho and Michael H. Huang, *Synthesis of Submicrometer-Sized Cu₂O Crystals with Morphological Evolution from Cubic to Hexapod Structures and Their Comparative Photocatalytic Activity*, J. Phys. Chem. C 2009, 113, 14159–14164.
39. Allen J. Bard and Larry R. Faulkner, *Electrochemical methods, fondamentals and applications*, John Wiley & Sons, Inc, New York, USA, 2001.
40. Roberto Spinicci, *Elementi di chimica*, Firenze University Press, Florence, 2009.
41. Qing Li, Jiaju Fu, Wenlei Zhu, Zhengzheng Chen, Bo Shen, Liheng Wu, Zheng Xi, Tanyuan Wang, Gang Lu, Jun-jie Zhu and Shouheng Sun, *Tuning Sn-Catalysis for Electrochemical Reduction of CO₂ to CO via the Core/Shell Cu/SnO₂ Structure*, J. Am. Chem. Soc. 2017, 139, 4290–4293.
42. Jing Li, Jiqing Jiao, Haochen Zhang, Peng Zhu, Hefeng Ma, Chen Chen, Hai Xiao and Qi Lu, *Two-Dimensional SnO₂ Nanosheets for Efficient Carbon Dioxide Electrocatalysis to Formate*, ACS Sustainable Chem. Eng. 2020, 8, 4975–4982.
43. Prakas Samantaa, Souvik Ghosha, Pranab Samantaa, Naresh Chandra Murmua, Tapas Kuilaa, *Alteration in capacitive performance of Sn-decorated MnO₂ with different crystal structure: An investigation towards the development of highperformance supercapacitor electrode materials*, Journal of Energy Storage 28 2020, 101281-101293.
44. Z. M. Jarzebski and J. P. Marten, *Physical Properties of SnO₂ Materials II. Electrical Properties*, J. Electrochem. Soc., 1976, 123, 299-309.

45. E. Fortin and F. L. Weichman, *Hall effect and electrical conductivity of Cu₂O monocrystals*, Canadian Journal of Physics, 1966, 4.

Copyright

Synthesis of Cu₂O Nanocrystals from Cubic to Rhombic Dodecahedral Structures and Their Comparative Photocatalytic Activity



Author: Wan-Chen Huang, Lian-Ming Lyu, Yu-Chen Yang, et al

Publication: Journal of the American Chemical Society

Publisher: American Chemical Society

Date: Jan 1, 2012

Copyright © 2012, American Chemical Society

PERMISSION/LICENSE IS GRANTED FOR YOUR ORDER AT NO CHARGE

This type of permission/license, instead of the standard Terms and Conditions, is sent to you because no fee is being charged for your order. Please note the following:

- Permission is granted for your request in both print and electronic formats, and translations.
- If figures and/or tables were requested, they may be adapted or used in part.
- Please print this page for your records and send a copy of it to your publisher/graduate school.
- Appropriate credit for the requested material should be given as follows: "Reprinted (adapted) with permission from {COMPLETE REFERENCE CITATION}. Copyright {YEAR} American Chemical Society." Insert appropriate information in place of the capitalized words.
- One-time permission is granted only for the use specified in your RightsLink request. No additional uses are granted (such as derivative works or other editions). For any uses, please submit a new request.

If credit is given to another source for the material you requested from RightsLink, permission must be obtained from that source.

[BACK](#)

[CLOSE WINDOW](#)

© 2021 Copyright - All Rights Reserved | Copyright Clearance Center, Inc. | Privacy statement | Terms and Conditions
Comments? We would like to hear from you. E-mail us at customercare@copyright.com

Acknowledgments

Thanks to Professor Simelys Pris Hernandez Ribullen and Maddalena Zoli for following me and helping me throughout the course of the thesis.

To my mother, Roberta Pavani, and to my father, Loreto Bucci, to always be examples of smart, generous, hearted people who do not shy away from challenges. They are my models and points of reference in everything, essential elements.

To my brothers, Bruno Bucci and Lorenzo Bucci, who are my right arms and who I can't do without even if they always make me angry.

To my grandparents, Rita Di Giambattista and Attilio Pavani, who are always present and always support me. two important pieces of heart. my thoughts always go to the grandparents who are no longer there.

To uncle Carlo Altrocchi, my great supporter in everything, like a grandfather, to whom I dedicate this thesis.

To Roberta Altrocchi, a zerofolle whom I love very much.

To my uncle Claudio Pavani, my aunt Laura Colli and my cousin Valerio to always be present.

To Uncle Giovanni, Elisabetta and Massimo Varisco for being an important part of the family.

To aunt Bionda, Tommasina Bucci, and uncle Giovanni Dafano for being amazing uncle.

To my super cousins Elio Dafano, Giulio Dafano and Ilaria Mancini, whom I love immensely.

To little Giovannino who is the love of home.

To my cousin Memi, Noemi Marinelli, thanks to her my Turin adventure began and Marco Mazzetti always tender with me.

To my auntie Eleonora whom I am very fond of.

To my school friends, Cristina Caladrella, Giorgia Baiocchi, Agnese Baiocchi, Alessia Rosati and Riccardo Sanna, my best friends, on which i can always count.

To Desire Capoccia, Teresa Comisso and Giovanna Giardina (Tormina), my funny friends and important like sister.

To my Blonde, Elena Marras, a friend of laughter and tears, essential for my survival during my master's degree.

To Alessandro Gilardini, a friend of trips and dives.

To Gioia, Caterina Brosio, and Giorgia Cosentino whom I love very much.

To Nadia Grifasi, Valeria Bruno and Serena Linsalata, with whom the laughter and jokes never end.

To Nancy, Nunzia Lauriello, and Rosy, Rosalba Virgiglio and Giorgia Morone, friends I care about.

To Melodj Dosa who is very tender with me always.

To my prof Carmine Mastroianni, who is the first to believe in me and support me, when I was about to undertake a university career at the Politecnico.

In conclusion, I sincerely thank everyone for having been there.